REDUCED-DATA MAGNETIC RESONANCE IMAGING RECONSTRUCTION METHODS: CONSTRAINTS AND SOLUTIONS

A Thesis
Presented to
The Academic Faculty

by

Lei H. Hamilton

In Partial Fulfillment
of the Requirements for the Degree
Doctor of Philosophy in the
School of Electrical and Computer Engineering

Georgia Institute of Technology
December 2011

REDUCED-DATA MAGNETIC RESONANCE IMAGING RECONSTRUCTION METHODS: CONSTRAINTS AND SOLUTIONS

Approved by:

Professor John Oshinski,
Committee Chair
Department of Biomedical Engineering
Georgia Institute of Technology

Professor Marijn Brummer, Advisor
Department of Electrical and
Computer Engineering
Georgia Institute of Technology

Professor Xiaoping Hu
Department of Biomedical Engineering
Georgia Institute of Technology

Professor Justin Romberg
Department of Electrical and
Computer Engineering
Georgia Institute of Technology

Professor Shella Keilholz
Department of Biomedical Engineering
Georgia Institute of Technology

Professor Xiaoli Ma
Department of Electrical and
Computer Engineering
Georgia Institute of Technology

Date Approved: 14 July 2011

To my family

Benjamin Hamilton

Xinnian Liu, Yuming Hou

Donna Hamilton, David Hamilton

ACKNOWLEDGEMENTS

I would like to thank my advisor, Marijn Brummer, for his support, guidance and encouragement during my graduate studies. I also would like to thank Professor Justin Romberg for providing both his inspiration in my work and financial support for my last summer semester in Gatech. I would also thank Professor Xiaoping Hu, Shella Keilholz, John Oshinski and Xiaoli Ma for serving on my committee and giving me valuable suggestions for my research.

I extend my thanks to Dr. Thomas Denney, Auburn University, for bringing me into the field of MRI and supporting my transfer to Georgia Tech to be with my husband.

I am also thankful for my colleague Senthil Ramamurthy for helping me acquiring the MRI data that I used for my research and thesis. Thanks for David Moratal for all his valuable suggestions and comment on the papers.

Thanks my husband, Russ, for his helpful discussion and support of my PhD work. I am also deeply indebted to my parents, who encouraged my scientific interest from early on and my parents-in-law, who continuously supported me during my studies.

TABLE OF CONTENTS

LIST OF TABLES

LIST OF FIGURES

LIST OF SYMBOLS OR ABBREVIATIONS

ACS	Auto Calibrating Signal.
BLAST	Broad-use Linear Acquisition Speed-up Technique.
CG	Conjugate Gradient.
CMRI	Cardiac Magnetic Resonance Imaging.
CS	Compressive Sensing.
CT	Computed Tomography.
DFT	Discrete Fourier Transform.
FOV	Field of View.
GEYSER	GRAPPA Enhanced Sensitivity Estimates for SENSE Reconstructions.
GP	Gerchberg-Papoulis.
GRAPPA	Generalized Autocalibrating Partially Parallel Acquisitions.
GRIS	Gerchberg Reduced Iterative System.
iNoquist	iterative Noquist.
MR	Magnetic Resonance.
MRI	Magnetic Resonance Imaging.
Noquist	No nyquist.
PF	Partial Fourier.
PILS	Partially parallel Imaging with Localized Sensitivities.
PINOT	Parallel Imaging and NOquist in Tandem.
PNS	Peripheral Nerve Stimulation.
POCS	Projection Onto Convex Sets.
rFOV	reduced Field of View.
SENSE	SENnSitivity Encoding.
SMASH	SiMultaneous Acquisition of Spatial Harmonics.

SNR	Signal to Noise Ratio.
SPACE-RIP	Sensitivity Profiles from an Array of Coils for Encoding and Reconstruction In Parallel.
SPIRiT	Iterative Self-consistent Parallel Imaging Reconstruction.
SR	Super Resolution.
SVD	Singular Value Decomposition.
UNFOLD	UNaliasing by Fourier-encoding the Overlaps using the temporaL Dimension.
VD-AUTO-SMASH	Variable Density AUTO SMASH.

SUMMARY

Magnetic resonance (MR) imaging is a non-invasive medical imaging technique to visualize detailed internal structure. Magnetic resonance imaging (MRI) provides great soft tissue contrast compared with other imaging modalities, which makes it especially useful in imaging the brain, the heart, and the musculoskeletal system. Magnetic resonance imaging speed is important especially in dynamic cardiac applications, which involve respiratory motion and heart motion. Patient safety considerations limit further use of faster gradients or higher RF power to speed up the pulse sequence beyond current technology.

With the introduction of reduced-data MR imaging methods, increasing acquisition speed has become possible without requiring a higher gradient system. Reduced-data MR imaging techniques have significantly reduced acquisition time, decreased motion artifacts, and increased spatial or temporal resolution. Various reduced-data imaging methods utilize data redundancy to increase imaging speed, but carry a price for higher imaging speed. This may be a signal-to-noise ratio (SNR) penalty, reduced resolution, or a combination of both. Many methods sacrifice edge information in favor of SNR gain, which is not preferable for applications which require accurate detection of myocardial boundaries.

This thesis presents a novel reduced-data imaging method, PINOT (Parallel Imaging and NOquist in Tandem), to accelerate MR imaging. PINOT does not apply any filter or interpolation, therefore preserves the edge details, with flexibility of improving SNR by regularization. A sampling scheme is designed for this method and the noise behavior is analyzed using the pseudo-replica method. The Conjugate-gradient (CG) method is used to alleviate the computational cost. Additional time savings is

achieved by providing a favorable initial estimate. Regularized PINOT uses Tikhonov regularization on highly accelerated MRI to relieve the noise penalty.

Another contribution is to exploit the data redundancy from parallel imaging, rFOV and partial Fourier methods. A Gerchberg Reduced Iterative System (GRIS), implemented with the Gerchberg-Papoulis (GP) iterative algorithm is introduced. Under the GRIS, which utilizes a temporal band-limitation constraint in the image reconstruction, a variant of Noquist called iterative implementation iNoquist (iterative Noquist) is proposed. Utilizing a different source of prior information, first combining iNoquist and Partial Fourier technique (phase-constrained iNoquist) and further integrating with parallel imaging methods (PINOT-GRIS) are presented to achieve additional acceleration gains.

CHAPTER I

INTRODUCTION

1.1 Motivation

Heart disease is the leading cause of death in the United States and throughout the whole world [48]. Heart disease includes conditions affecting the heart, such as coronary heart disease, heart attack, congestive heart failure, and congenital heart disease. Cardiovascular magnetic resonance (CMR) imaging, sometimes known as cardiac MRI (CMRI) is a highly accurate, non-ionizing and routinely used imaging modality for the diagnosis of heart disease. The detection of cardiovascular disease is based on anatomical changes and CMR is especially suited for the assessment of cardiac function and morphology. CMR is used to evaluate the anatomy and function of the heart, valves, major vessels, and surrounding structures (such as the surrounding pericardial sac); detect and evaluate the effects of coronary artery disease. Cardiac MRI can separate ischemic from non-ischemic cardiomyopathy, and is the most important imaging modality for the diagnosis and follow-up of patients with myocarditis. Cardiac MRI is increasingly important in the diagnosis and follow-up of patients with congenital heart disease, usually as a complement to echocardiography.

Although cardiac MRI is a versatile and highly accurate imaging modality, there are several practical limitations to the use of the technique. Compared with computed tomography (CT) scans, cardiac MRI examinations are time-consuming. Cardiac MRI usually takes 60 to 90 minutes, depending on which images are needed, While it only takes CT approximately 15 minutes. Furthermore, most routine cardiac MRI techniques are dependent upon image acquisition during breathhold to

eliminate movement artifacts. Both image quality and the duration of the examination are highly dependent upon the patient's ability to hold their breath repeatedly during imaging. For patients or children who are unable to perform breatholds well, a poor image quality can be anticipated and hinders the diagnosis. Solutions are to use respiratory gating or signal averaging. Respiratory gating typically makes the scan time longer. Signal averaging increases SNR, removes ghost artifacts but blurring still exists. Another solution, accelerated imaging, leads to reduced scan time, decreased motion artifacts, and increased spatial or temporal resolution and is beneficial for diagnosis.

Accelerated imaging is especially important in dynamic CMR applications and improving image speed has been a research topic in the MRI field for the last two decades. However, current MRI scanners already operate at the limits of potential imaging speed. To increase gradient strength for accelerated imaging, more powerful amplifiers and gradient coils capable of taking the increased current and voltage are needed, both of which add significantly to the cost of the scanner. Furthermore, when the human nervous system is exposed to a time dependent magnetic field, spontaneous nerve firing may occur; this is known as peripheral nerve stimulation (PNS). Physiological limits associated with the rate of switching of such gradients restrict the imaging speed as well.

With the introduction of reduced-data MR imaging methods, a decrease in acquisition time can be achieved without the need of further increasing gradient performance. Normally when only a fraction of phase-encoding steps are acquired, the Nyquist criterion is violated. After Fourier Transform, under-sampled k-space data will exhibit aliased images. Exploiting data redundancy, reduced-data methods imaging result in an accelerated image acquisition while reconstructing artifact-free images. Alternatively increased temporal resolution at a given spatial resolution may be achieved, or the time savings due to reduced-data imaging methods can also be used to improve

the spatial resolution in a given imaging time.

For the past twenty years, various reduced-data imaging methods have been proposed and are used to accelerate imaging speed to achieve better quality images. They all utilize data redundancy by either filling in undersampled phase-encoding lines or unfolding the aliased images to increase imaging speed, but carry prices for the higher imaging speed. One major tradeoff with imaging speed gain may be a signal-to-noise ratio (SNR) penalty, reduced spatial or temporal resolution, or a combination of both. From a linear system perspective, they all try to solve an ill-conditioned linear system problem. Recent works achieve combined gains in imaging speed or better performance by jointly using independent sources of data redundancy to improve the performance of single component method. Interestingly, none of the combined methods are capable of reconstructing the image at the same spatiotemporal resolution as the fully sampled grid due to the use of filters, interpolation or regularization, even though the inversion problem is still overdetermined. Furthermore, this process is not reversible. In applications where image resolution is the most critical criterion, such as accurate detection of myocardial boundary locations, reduced-data imaging methods which allow full or nearly full preservation of "full-grid resolution" may present the preferred approach.

1.2 Outline of Thesis

The main contribution of this thesis is to improve reduced-data imaging reconstruction image performance from two different angles. First, we present reduced-data imaging methods to accelerate CMR that preserve the image resolution, while with flexibility of improving SNR by regularization. Another contribution is to exploit maximally the data redundancy from three different reduced-data methods and exceed the performance of each individual method to further reduce imaging time and/or an increase in signal-to-noise ratio.

To appreciate the necessity of reduced-data imaging methods' development, chapter 2 introduces MRI physics, the background on how MRI works. Following that, chapter 2 also gives a brief technical overview over the present reduced-data imaging reconstruction methods and strategies. The basic principle of reduced-data imaging is introduced and methods are divided into several categories. Examples of several typical/representative reconstruction methods have been reviewed in detail and their advantages and drawbacks are discussed. Chapter 3 presents a novel method named PINOT (Parallel Imaging and NOquist in Tandem), which combines SPACE-RIP parallel imaging and the Noquist rFOV method. PINOT does not apply any filter or interpolation, therefore preserves edge details, with flexibility of improving SNR by regularization. Conjugate-gradient method is used to alleviate the computational cost. Chapter 4 focuses on the improvements for the PINOT method. Additional time savings for PINOT reconstruction is achieved by providing a favorable initial estimate. The accuracy of sensitivity maps is very important for any reduced-data imaging methods involving parallel imaging which require the sensitivity maps explicitly, an auto-calibrated PINOT variant is presented using GRAPPA to calculate sensitivity maps. Chapter 5 introduces a Gerchberg Reduced Iterative System (GRIS), implemented with the Gerchberg-Papoulis (GP) iterative algorithm. Under GRIS, which utilizes a temporal band-limitation constraint in the image reconstruction, a variant of Noquist called iterative Noquist (iNoquist), is proposed. Utilizing different source of prior information, a first combinations of iNoquist and Partial Fourier technique (phase-constrained iNoquist) and further combining with parallel imaging method (PINOT-GRIS) are presented to achieve additional acceleration gains. The theory of GRIS and all three novel methods will be introduced, followed by experiments with phantom and in vivo data. Reconstruction results will be demonstrated. Conclusion and future work are in chapter 6.

1.3 Specific Contributions

In summary, this thesis explores several new techniques of reduced-data imaging in MRI.

- Develop a novel reduced-data MR imaging method PINOT.
- Develop sampling schemes for PINOT method and justify by comparing with other sampling schemes.
- Compare PINOT's performance with other two reduced-data imaging methods, TSENSE and *k*-*t* SENSE.
- Analyze the noise behavior of PINOT based on pseudo-replica method and compare with TSENSE and *k*-*t* SENSE.
- Propose a variant auto-calibrated PINOT which used interleaved average *k*-space sample to fit GRAPPA (Generalized Autocalibrating Partially Parallel Acquisitions), and calculate sensitivity maps from GRAPPA results.
- Improve PINOT reconstruction speed with a fast initial estimate. Additional time savings is achieved by providing a favorable initial estimate.
- Present regularized PINOT using Tikhonov regularization on higher reduction factor to relieve the noise penalty.
- Develop a novel phase constrained iterative Noquist method, for the first time combining Partial Fourier with reduced FOV method, iNoquist.
- Develop method PINOT-GRIS, combining three different data redundancy sources from PINOT and Partial Fourier method.

The main contributions of this thesis is to offer an accelerated imaging method, PINOT, which preserves the spatial-temporal resolution, which is beneficial for the

heart disease diagnosis. Another contribution is to present PINOT-GRIS, which exploits three differet sources of data redundancy and to improve the performance of the single method it combined to further reduce imaging time and/or an increase in signal-to-noise ratio.

CHAPTER II

MAGNETIC RESONANCE IMAGING (MRI) INTRODUCTION

2.1 Introduction

MRI provides clinical anatomical and functional information with minimal risk. The principle of the MRI system is rather complex, this chapter begins with a brief introduction of MRI fundamentals to provide the basic background. A more detailed explanation of MRI principles can be found in many MRI textbooks [39, 66, 16]. MRI is very sensitive to motion, and will show blurring and ghosting artifacts if patients move during the scan. MR imaging speed is important especially in dynamic cardiac applications, which involve both respiratory motion and heart motion. With the introduction of reduced-data MR imaging methods, a decrease in acquisition time can be achieved. The second part of the chapter givens a technical overview of current reduced-data imaging methods.

2.2 MRI Fundamentals

2.2.1 Spin Physics

Some atomic nuclei with an odd atomic weight and/or an odd atomic number, such as ^{1}H, ^{13}C, ^{15}N, ^{31}P, possess a fundamental quantum property called spin. For MRI, the most important nucleus is the hydrogen atom, ^{1}H, consists of a single proton with spin 1/2. The MRI signal comes from protons in the living tissue, primarily water molecules. Spin system can be described as a microscopic bar magnet and therefore can be represented by a vector called magnetic moment $\vec{\mu}$. In the absence of an external magnetic field, their directions are completely random due to thermal

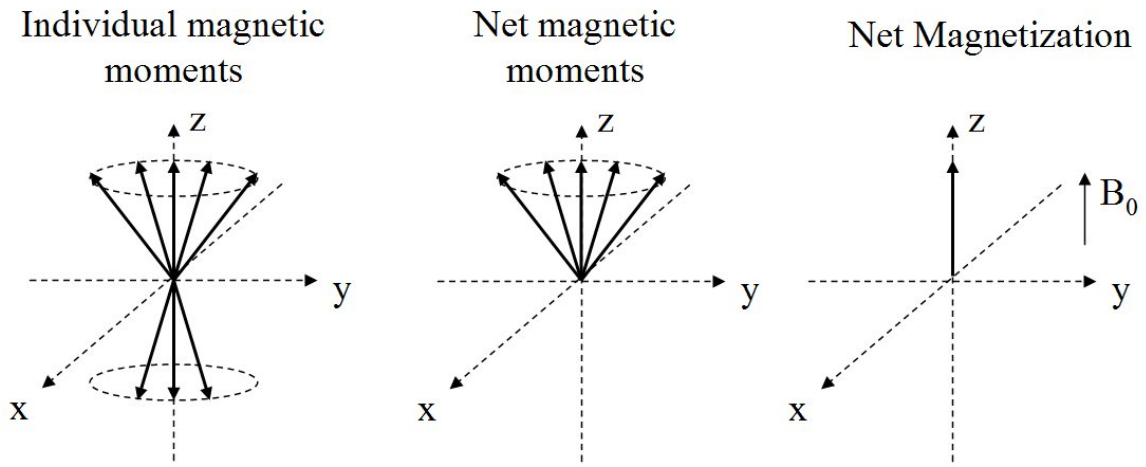

Figure 1: Left figure is the magnetic moments from each proton precess around the z axis. Middle one shows the net magnetic moments corresponding to the slightly greater number of aligned parallel to the magnetic field than antiparallel. Right one shows the net magnetization, the sum of all the magnetic moment.

random motion and therefore show no net magnetic field. In a magnetic field, protons align themselves along the magnetic field direction. When placed in a magnetic filed B_0 (along z axis), magnetic moments undergo Zeeman interaction or spin-splitting to two states (Fig. 1). Two states of equilibrium are either with the field (low energy state) or against the field (high energy state). The precession of $\vec{\mu}$ is called nuclear precession. The corresponding frequency is proportional to the strength of the magnetic field B_0. This frequency is termed the Larmor frequency:

$$\omega = \gamma B_0, \tag{2.1}$$

where γ is called gyromagnetic ratio and equals to 42.58MHz/Tesla for ^{1}H atom. For a typical 1.5 Tesla (T) clinical magnetic field, the value of the resonant frequency in hertz (f) is approximately 63.9 MHz. Larger number of protons in lower energy state generates a net magnetization vector $\vec{M} = \sum_{n=1}^{N_s} \vec{\mu}_n$. The net magnetization is the vector sum of all the individual proton magnetic moments, given by:

$$M = \left|\vec{M}\right| = \sum_{n=1}^{N_s} \vec{\mu}_{z,n} = \frac{\gamma^2 h^2 B_0 N_s}{16\pi^2 kT}. \tag{2.2}$$

Here, N_s is the total number of spins and h is Plank constant (6.6×10^{-34}J-s). k is the Boltzmann constant, with a value of 1.38×10^{-23}J/K, and T is the temperature in Kelvins. At equilibrium, the net magnetization aligns with the main magnetic field B_0, and only has a z component because the vector sum of the components in the x and y axes are zero:

$$M_z = M_0, M_y = 0, M_x = 0. \tag{2.3}$$

2.2.2 Excitation and Relaxation

So far, the macroscopic effect of an external magnetic field is the generation of a bulk magnetization vector pointing along the direction of B_0. The second magnetic field B_1 along x axis, generated by a radiofrequency (RF) pulse at Larmor frequency $\omega_{rf} = \omega_0$, tips protons from alignment with z axis toward the transverse plane and creates a transverse magnetization $M_x y$. The angle of the tip is called flip angle α, which is proportional to the strength of the applied RF field and the RF pulse duration time τ_{B1}:

$$\alpha = \gamma B_1 \tau_{B1}. \tag{2.4}$$

Switching off the RF pulse will lead to the equilibrium of the magnetization. This process is called free precession. A recovery of the longitudinal magnetization M_z, called longitudinal relaxation and the value of M_z at time t is:

$$M_z(t) = M_0 \cos\alpha + (M_0 - M_0 \cos\alpha)(1 - e^{-t/T_1}). \tag{2.5}$$

If $\alpha = 90°$, $M_z(t) = M_0(1 - e^{-t/T_1})$. The return of M_z to its equilibrium is due to protons losing their energy to the surrounding lattice (the spin-lattice relaxation).

The relaxation of the transverse magnetization return to its equilibrium is called transverse relaxation or spin-spin (T_2) relaxation. T_2 results from interactions protons with their surroundings. The net magnetization M_y in the transverse plane as a function of time t shows in the following:

$$M_y(t) = M_0 \sin\alpha e^{-t/T_2} \tag{2.6}$$

The overall relaxation time for the decay of the transverse magnetization is T_2^* which is from T_2 plus defects in main magnetic field.

$$\frac{1}{T_2^*} = \frac{1}{T_2^+} + \frac{1}{T_2} \tag{2.7}$$

Other than proton density ρ, different tissues have different T_1 and T_2 and they are prime determinates of image contrast.

2.2.3 Detection and Localization (slice selection, spatial encoding)

MR signal detection is based on the Faraday law of electromagnetic induction and the principle of reciprocity. In MRI, the bulk magnetization is processing at a radio frequency as a changing magnetic flux through a conducting loop (receiver coil), which induces a voltage in a receiver coil. The induced voltage is a high frequency signal and often is converted to low frequency through signal demodulation. The complex signal, with two outputs, is obtained by demodulating the voltage. This signal is still the sum of signals from protons at all different locations. In order to distinguish the signals at different spatial locations, a magnetic field gradient is applied, which results in spatial dependent proton resonant frequencies at different positions. In this way, spatial information will be encoded into MR signals. In spin wrap imaging, the most commonly used spatial encoding technique, the magnetic field gradient is applied differently in all three different directions: slice selection, phase-encoding, and frequency-encoding.

$$\frac{\partial B_z}{\partial z} = G_z, \frac{\partial B_z}{\partial x} = G_x, \frac{\partial B_z}{\partial y} = G_y. \tag{2.8}$$

The effective magnetic field is the sum of the static component B_0 with additional linear magnetic field gradient $\boldsymbol{G} = (G_x, G_y, G_z)$ and can be expressed as $\Delta \boldsymbol{k}$, the corresponding precessional frequencies therefore is a function of their location $\boldsymbol{\omega} = \gamma \boldsymbol{B_{(r)}}$. The slice selection magnetic field gradient, G_{slice}, is accomplished by a RF pulse. Spins within a certain bandwidth of Larmor frequencies which matches the

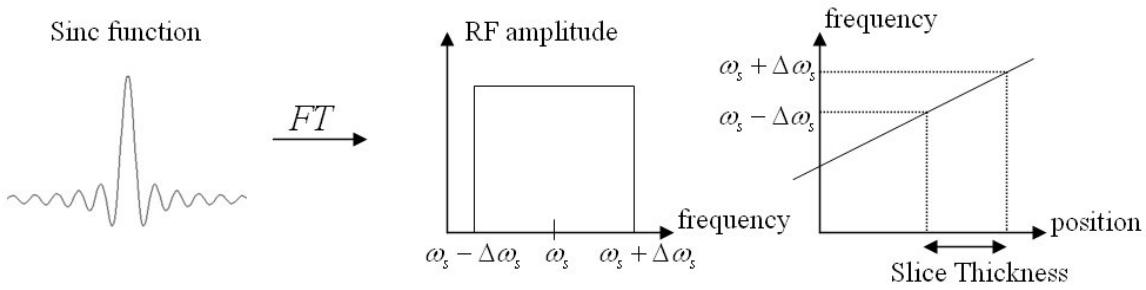

Figure 2: The RF pulse used for slice selection and the corresponding frequency bandwidth in b. c is the relationship between frequency bandwidth and slice thickness.

bandwidth of the RF pulse will be excited. A sinc-shaped RF pulse is often used to produce a square-shaped slice (Fig. 2). The slice selection orientation can be in the x, y or z direction, which are called sagittal, coronal, or axial respectively.

After selecting a slice, the other two dimension information can be encoded by phase encoding and frequency encoding to produce a two-dimensional image. A frequency encoding gradient G_x, in the x direction, is turned on during the data acquisition. Frequency is proportional to the x location. While the phase is encoded by a gradient G_y, in the y direction, turned on and off (duration time τ_{pe}) before the data acquisition begins. Phase is proportional to the y position. The combination of phase-encoding and frequency-encoding gradients gives the signal

$$S(G_x, \tau_{pe}, G_x, t) \propto \int_{slice}\int_{slice} \rho(x,y) e^{-j\gamma G_x x t} e^{-j\gamma G_y y \tau_{pe}} dxdy. \tag{2.9}$$

2.2.4 MR Image Reconstruction

MR image information is not encoded directly in image space, but in Fourier domain which we refer to "k-space". If we define two variables k_x and k_y as

$$k_x = \frac{\gamma}{2\pi} G_x t, k_y = \frac{\gamma}{2\pi} G_y \tau_{pe}, \tag{2.10}$$

where x and y are frequency- and phase-encoding direction. Eq.2.9 can be expressed as

$$S(k_x, k_y) \propto \int_{slice}\int_{slice} \rho(x,y) e^{-jk_x x} e^{-jk_y y} dxdy. \tag{2.11}$$

Therefore, the MR signals can be viewed as a two-dimensional data set in k-space. Taking inverse Fourier transform of the k-space data gives the MR image, showing the estimate of proton density $\rho(x, y)$. Based on Nyquist theory, the distance between k-space points $\Delta \boldsymbol{k}$ decide the field of view (FOV) of the image.

$$\begin{aligned} FOV_x &= \frac{1}{\Delta k_x} = \frac{2\pi}{\gamma G_x t_{dw}} \\ FOV_y &= \frac{1}{\Delta k_x} = \frac{2\pi}{\gamma G_y \tau_{pe}} \end{aligned} \tag{2.12}$$

In MRI, we generally do not collect data immediately after the RF pulse since we need time to perform spatial encoding (for 2-D image case). A pulse sequence diagram representing multiple steps of the MR signal reception and an example of k-space are shown in Figure 3. First, the RF pulse and slice selection gradient are applied to tip the protons in the chosen frequency range to the transverse direction. The phase encoding gradient is switched on for a period to time τ_{pe}. After that, the gradient is switched off and frequency encoding gradient is turned on during the data acquisition. This accounts for one phase encoding line, which represents a single row in k-space. For a 2D image, a number of different phase encoding gradient values must be used. A typical example of an image with 256 phase encoding lines and 256 frequency encoding lines, if TR is defined as the repeat time between one phase encoding excitation and then the whole imaging time is $256 \times TR$. Since each phase encoding step takes a significant acquisition time, it is beneficial to minimize the number of phase encoding lines to save some time. Patient safety considerations limit further use of faster gradients or higher RF power to speed up the pulse sequence beyond current technology. Skipping phase encoding lines causes aliasing in the reconstructed images obtained after taking inverse Fourier transform of under-sampled k-space data due to the violation of the Nyquist criteria. However, with some prior information about images, the missing phase encoding lines can be estimated, and hence alias free images can be reconstructed. This is the basic principle of reduced-data imaging methods.

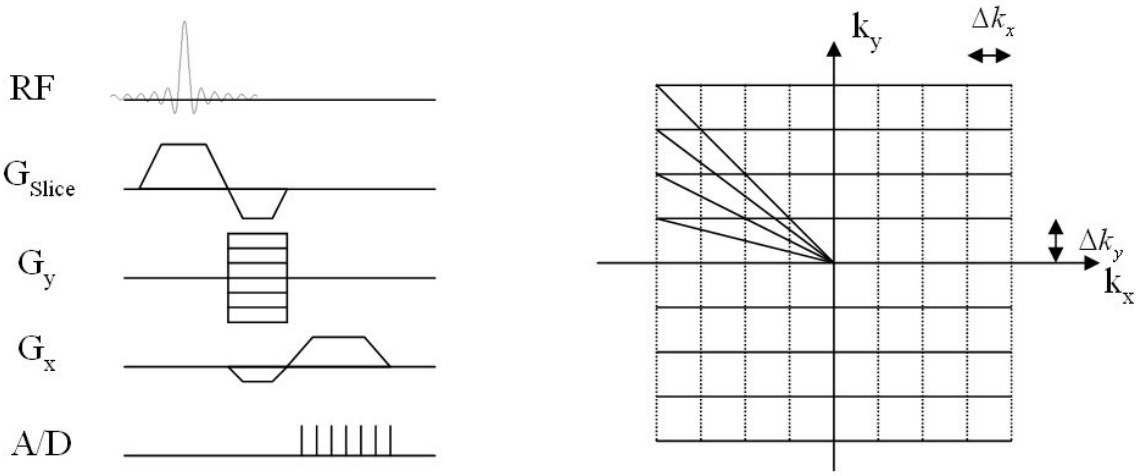

Figure 3: The RF pulse used for slice selection and the corresponding frequency bandwidth in b. c is the relationship between frequency bandwidth and slice thickness.

2.3 Reduced-data Imaging Techniques

In the past 20 years, various reduced-data imaging methods have been proposed to accelerate the imaging speed through incorporation of prior information. The idea behind this is to incorporate some prior information about the image to define data redundancy which may be used to reduce data required in the reconstruction. Based on different sources of prior information, they can be pursued in several ways: partial Fourier (PF) techniques, parallel MR imaging (pMRI) methods, reduced field of view (rFOV) methods, recent application of compressive sensing (CS) techniques, and the combined implementation of above methods, which has higher acceleration factor by jointly using independent sources of data redundancy.

2.3.1 Parallel imaging methods

Phased-array coils consist of a number of ideally decoupled surface coils that simultaneously receive MR signals. They were originally introduced to improve signal to noise ratio (SNR) [57], shown in Fig. 4. Later, prior knowledge of receiver coil sensitivity profiles has been applied to accelerate the MRI scan. This class of techniques is called parallel imaging. Parallel imaging methods utilize the information provided

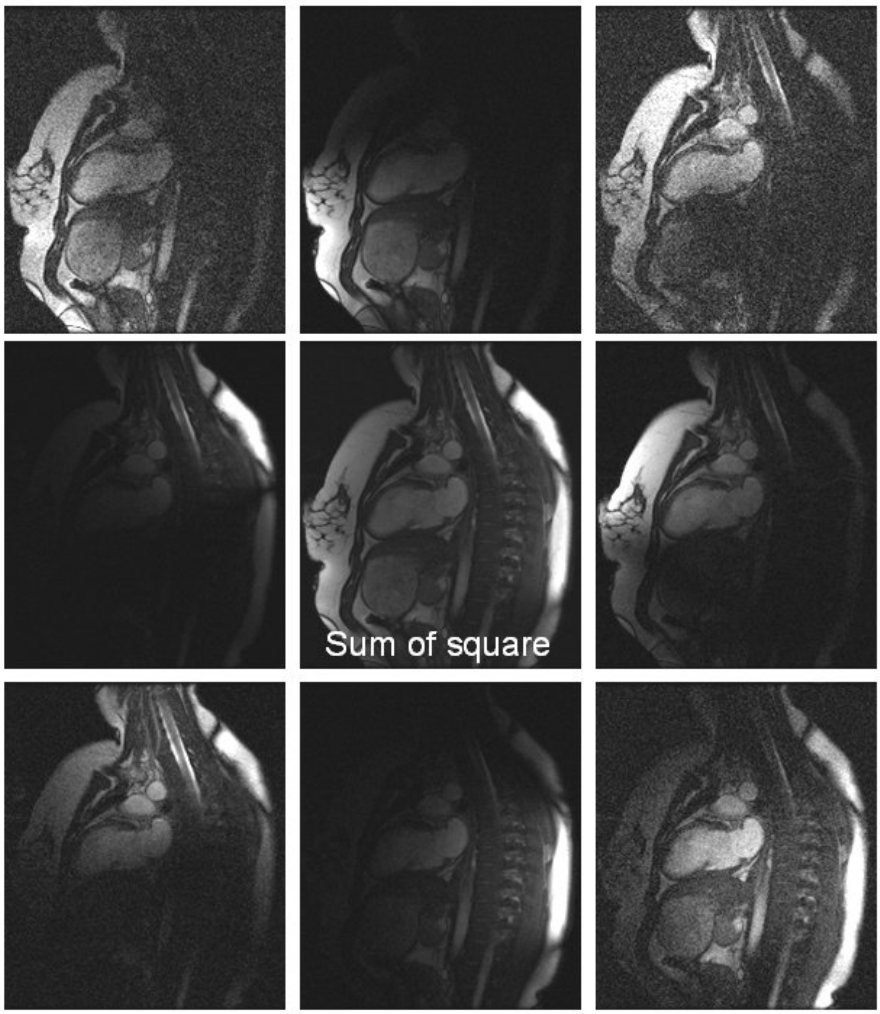

Figure 4: Phase array coil images and their sum of square image example.

by multiple receiver coils to reduce the image data size by skipping data acquisition in portions of k-space that would normally scanned, and images are reconstructed from these reduced sample sets of data. Parallel imaging methods, such as SMASH [59], AUTO-SMASH [32], VD-AUTO-SMASH [25], GRAPPA [14] and SPIRiT [44] synthesize missing k-space samples from acquired samples at other locations to construct a complete grid. PILS [13], SENSE [54], and SPACE-RIP [37] use estimates of the coil sensitivity maps to reconstruct the image from reduced k-space samples. The maximum sampling rate reduction factor is limited by the number of independent channels [52, 67]. pMRI methods take place either in image space (e.g. PILS, SENSE) or in k-space (SMASH, GRAPPA). Most pMRI methods require availability of coil sensitivity maps. These sensitivity maps can be derived either from a prescan or during reduced-data imaging scan by acquiring a few additional k-space lines (auto-calibration).

2.3.2 Reduced field of view (rFOV) methods

The main idea behind rFOV methods is that spatiotemporal redundancy in dynamic imaging may be exploited if parts of the field of view (FOV) are relatively static over time. Compared to parallel acquisition methods for reduced-data imaging, it does not require phased-array coils. UNFOLD [46] employs time interleaving of k-space lines to remove data redundancy from time-varying objects using a temporal filter. Noquist [3] exploits the data redundancy associated with the presence of a static FOV region by only reconstructing it once for a dynamic sequence. It has a direct inversion model without temporal filtering or interpolation. The reduction factor for these two methods is limited by the ratio of the size of the static region to the total FOV. k-t BLAST [62] obtains a low-resolution estimate of the signal distribution in x-f space using training data, and uses it to separate the true signal from the aliased copies.

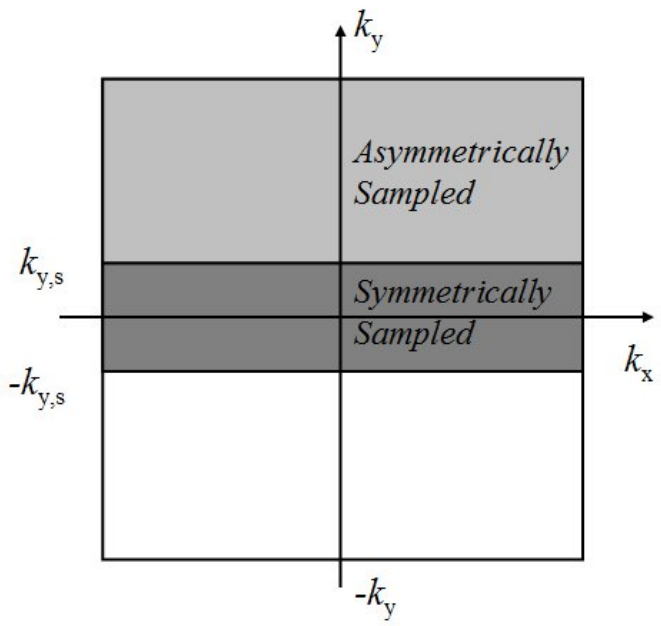

Figure 5: Partial k-space acquisition reduces the number of phase encodes required for reducing scan time.

2.3.3 Partial Fourier Imaging

One early technique for accelerating MR speed is called partial Fourier (PF) [8, 7, 50], which applies phase constraints to image reconstruction. PF techniques (Fig. 5) are based on the fact that a real-valued object in image space corresponds to Hermitian symmetry in k-space. Typically, PF methods fully sample half of k-space, and restores the true image phase using a low-frequency phase map estimated from the fully-sampled k-space center. There are many ways to implement the PF technique, such as Margosian approach [47], Cuppen method [7], Homodyne detection [50], and a projection onto convex sets (POCS) based iterative method [15]. Phase information is typically estimated in image space from the low-resolution image. Recent improvement [30] has focused on implicitly estimating phase information in k-space through data fitting to improve the accuracy of the phase information.

2.3.4 Compressive Sensing Methods

Another recent development in dynamic MRI is the introduction of "compressed sensing" (CS) theory from the signal processing community [5, 10]. According to compressed sensing theory, MR images which are sparse or have a sparse representation in some transfrom (such as wavelet transform) domain can be reconstructed from significantly fewer random samples than the traditional Nyquist sampling limit with very little information loss. MR images can be successfully reconstructed by minimizing the $l1$ norm of a transformed image, subject to data fidelity constraints. SparseMRI [43] was the paper introduced the theory of compressive sensing into reduced-data MR imaging and demonstrated significant scan time reduction.

2.3.5 Combined Methods

These previous introduced methods (section 2.3.1-2.3.4) all utilize independent prior information sources to accelerate imaging speed, therefore may be combined for even higher gains in imaging speed or better image quality. TSENSE, UNFOLD-SENSE and k-t SENSE integrate parallel imaging methods with rFOV methods. TSENSE, as initially proposed in [34], uses UNFOLD to eliminate residual aliasing artifacts that are not removed by SENSE. Subsequent improvements [35] combine UNFOLD and SENSE for compounded gains from each individual method. UNFOLD-SENSE [45] combines variable-density SENSE and UNFOLD-based artifact suppression scheme, with autocalibrated signals for sensitivity map estimation. TGRAPPA [2] and k-t GRAPPA [63] use time-interleaved sampling with improved acquisition efficiency. k-t SENSE [62] allows high reduction factors by combining k-t BLAST with SENSE parallel imaging. Other works have combined both parallel imaging and partial Fourier techniques. Bydder et al [4] and Willig-Onwuachi et al [68] combined PF with parallel imaging by constraining parallel imaging to reconstruct a real image. In addition, POCSENSE [58], under POCS formalism, uses parallel imaging technique SENSE

followed by PF to reconstruct images. Parallel imaging methods are introduced to combine with compressive sensing method for further reduction. CS-SENSE [38] has been proposed to combine SENSE from parallel MRI, and compressed sensing for rapid MR imaging. L1SPIRiT [42] is another robust, iterative algorithm for MR images reconstruction acquired with parallel imaging and compressed sensing acceleration.

2.4 Reduced-data imaging methods as linear Inverse Problem

During acquisition of a MR image sequence, k-space sampling points $F(k,t)$ are acquired at multiple time points t in the cardiac cycle. In conventional serial imaging with Cartesian k-space sampling, trains of the same read-out sampling points are acquired at each phase encoding value to cover a k-space grid in identical fashion at each time point. Fourier inversion reconstructs the images $f(x,t)$. Reduced sampling in the read-out/frequency encoding dimension does not offer much imaging time savings, but imaging time is linearly proportional to the number of phase encodings. Therefore reduced-data imaging methods often focus on reducing the number of phase encodings. Read-out reconstruction is performed conventionally by DFT, while appropriate algorithms must be developed for modified phase encoding reconstruction from reduced samples. Thus, the 2-D spatial image reconstruction problem can be reduced to a 1-D spatial problem, only considering the phase encoding and time dimensions. Considering temporal and coil information together for a dynamic image sequence $f(x,t)$, the MR signal F_c received for cardiac delay time t in each coil c, with S_c sensitivity map is:

$$F_c(k,t) = \sum_{x=0}^{N-1} S_c(x) f(x,t) \varphi(x,k) \tag{2.13}$$

N is the number of phase encoding views, k and $\varphi(x,k) = e^{-j2\pi kx}$ are the Fourier coefficients. Expressed in matrix form:

$$F = Mf, \tag{2.14}$$

where vector F contains the k-space data of all N_c coils and phase encodings for time frame t, and M is the forward system matrix. Conventional image reconstruction does not invert the coil modulation S_c, and reconstructs the modulated function $f_S = S_c f$ by Fourier inversion:

$$f_s = \Omega^{-1} F, \tag{2.15}$$

where Ω^{-1} contains the inverse Fourier coefficients. A final image f (Fig. 2.4).is reconstructed conventionally by calculating magnitude images with the sum of squares of all the coil images f_s,

$$f = \sqrt{\sum_s |f_s|^2}, \tag{2.16}$$

In essence, for MR reconstruction, we have some observations of k-space data M, from which we want to reconstruction the original MR images f. In a general form, the observation process can be approximated as a linear operation M (Fourier Transform).

$$F = Mf. \tag{2.17}$$

Reduced-data imagings are the cases where the number of observations k-sapce data is much fewer than the MR images. Reduced-data imaging methods can be formulated as solving a linear inverse problem to unfold the aliased images to the full FOV images (Fig. 6). In practise, it is defined as a forward linear problem:

$$F = Mf + n. \tag{2.18}$$

Here f is the unknown image, F is the under-sampled k-space data, M is the forward matrix and n is the noise. Given enough prior information, Eq. 2.18 can be formed as

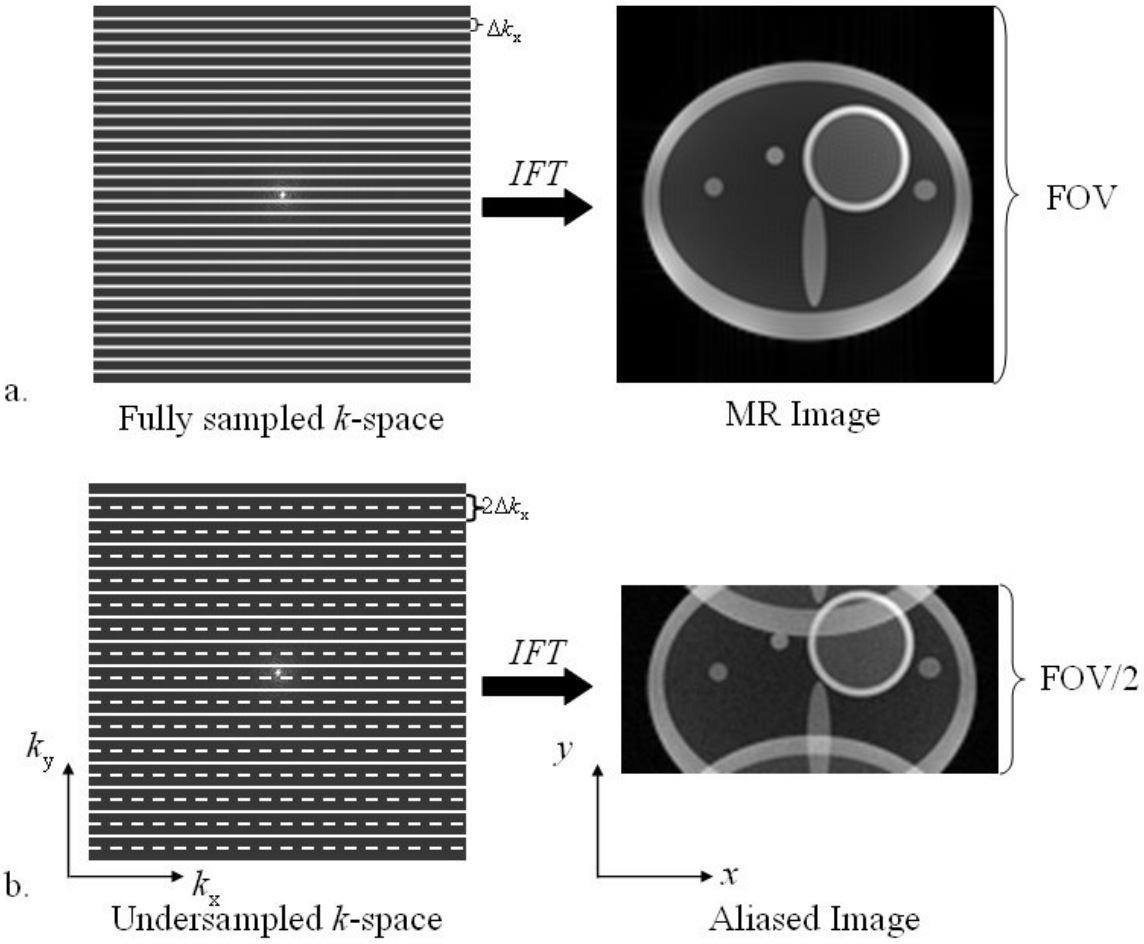

Figure 6: a. Conventional acquisition of fully sampled k-space, resulting in a full FOV image after inverse Fourier transformation. b. Undersampled acquisition ($R = 2$), resulting in a reduced FOV (FOV/2) with aliasing artifacts. Solid lines indicate sampled k-space lines, dashed lines indicate not sampled k-space lines.

an over-determined linear system. The least-square solution therefore can be defined as:

$$\bar{f} = \arg\min_{f} \|Mf - F\|_2^2 . \tag{2.19}$$

In the cases where matrix M is ill-conditioned, the noise level can be high in the reconstructed images. Regularization techniques [41, 69] can be introduced to solve the ill-conditioned linear equation to reduce noise level. Choosing the simplest regularization term, the identity matrix, the solution is formulated as:

$$\bar{f}_r = \arg\min_{f} \|Mf - F\|_2^2 + \alpha \|f\|_2^2 , \tag{2.20}$$

where the regularization parameter α offers a trade-off mechanism between the error from prior knowledge (large α) or the error from unconditioned matrix inversion (small α). Consider the extreme case where α is zero, Eq. 2.20 is equivalent to 2.19. For all reduced-data MR imaging techniques, coverage of the k-space for image reconstruction may become undersampled along one or more phase-encoding dimensions, which corresponds to a reduction of overall scan time. To quantify the time savings we define a reduction factor/acceleration factor R as the size of the sampled phase encoding data $N_{sampled}$ as an inverse ratio of full-grid Fourier phase encoding data N:

$$R = N/N_{sampled}. \tag{2.21}$$

Figure 6 shows an example of acceleration/reduction factor $R = 2$.

2.5 Algorithms

Many methods have been introduced for accelerating MRI. Here we review some of the most influential works in this field and illustrate the theoretical details with examples.

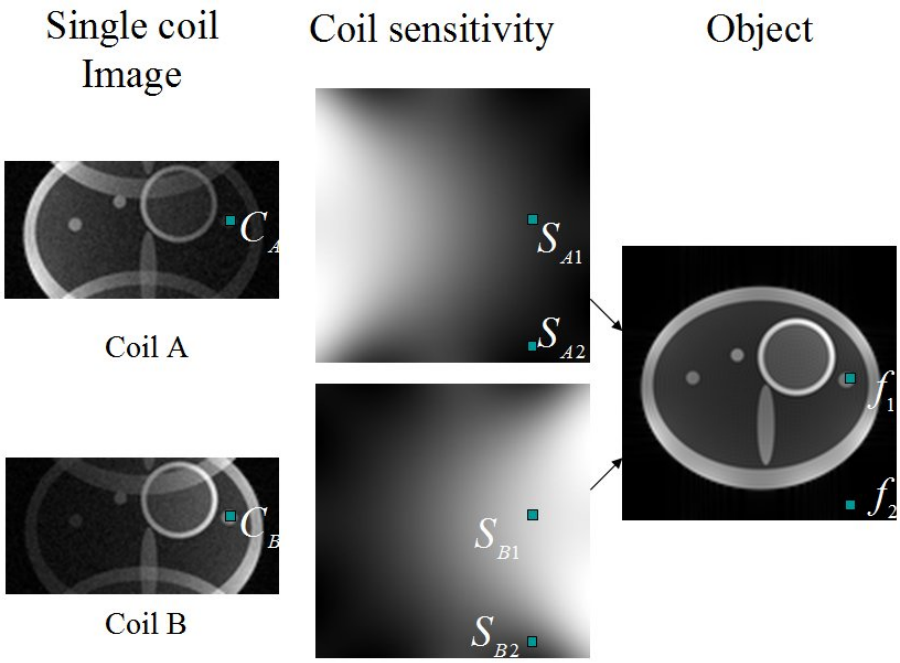

Figure 7: Illustration of the SENSE with acceleration factor $R = 2$ with two receiver coils.

2.5.1 Parallel Imaging (SENSE/SPACE-RIP, GRAPPA)

SENSE [54] is a parallel imaging method that operates in the image domain. Like other parallel imaging methods, it utilizes the information provided by multiple receiver coils to skip portions of k-space that normally is phase-encoded by a gradient field. Undersampled k-space along phase encoding direction causes reduction of the FOV and aliased images. To explain how SENSE can undo this aliasing, here is an example with acceleration/reduction factor $R = 2$ with a set of two coils, as shown in Figure 7. For a single aliased pixel at location (x, y) in the aliased image, the signals from each of two surface coil are:

$$\begin{aligned} C_A &= S_{A1} f_1 + S_{A2} f_2 \\ C_B &= S_{B1} f_1 + S_{B2} f_2 \end{aligned} \tag{2.22}$$

Here S denotes the coil sensitivity maps, f_1 and f_2 are super-imposed image pixels and C_A, C_B are aliased coil image pixels from coil A and coil B. Assuming coil sensitivities S are known, we can solve this equation and find the value of aliased

pixels, hence unfold aliased images. The equation above can be shown in a matrix form:

$$\vec{C} = \hat{S} \cdot \vec{f}. \tag{2.23}$$

For a single aliased pixel, if we denote n_c as the number of receiver coils and n_p as the number of superimposed pixels, the size of matrix S is $n_p \times n_c$. Theoretically, as long as $n_p > n_c$, matrix S is overdetermined, taking inverse of matrix S or more general form pseudo-inverse of matrix S, image f can be reconstructed by

$$\hat{S}^{-1} \cdot \vec{C} = \vec{f} \;\; or \;\; \hat{S}^{\dagger} \cdot \vec{C} = \vec{f}. \tag{2.24}$$

SPACE-RIP [37] is essentially a k-space implementation of SENSE parallel imaging technique. The image reconstruction by the SPACE-RIP method is simply a direct inversion of weighted Fourier transform matrix, combined for all coils:

$$\begin{bmatrix} F_1(k) \\ F_2(k) \\ \vdots \\ F_C(k) \end{bmatrix} = \begin{bmatrix} S_1(1)e^{j2\pi k1} & ... & S_1(N)e^{j2\pi kN} \\ S_2(1)e^{j2\pi k1} & ... & S_2(N)e^{j2\pi kN} \\ \vdots & \vdots & \vdots \\ S_C(1)e^{j2\pi k1} & ... & S_C(N)e^{j2\pi kN} \end{bmatrix} \begin{bmatrix} f(1) \\ f(2) \\ \vdots \\ f(N). \end{bmatrix} \tag{2.25}$$

Matrix M_p contains both the coil sensitivity information S and the Fourier coefficients:

$$M_p = S\Omega. \tag{2.26}$$

For parallel imaging $R_p = N/N_{sample\_p}$, where N_{sample_p} is the number of sampled phase encodings. M_p is of size $N_c N_{sample\_p} \times N$, N_c is the number of coils used in the reconstruction. Hence for M_p to remain invertible the reduction factor R_p must be

$$R_p \leq N_c. \tag{2.27}$$

The SPACE-RIP method (10) finds the solution by pseudo-inversion of Eq. 2.25

$$f = (M_p^H M_p)^{-1} M_p^H F. \tag{2.28}$$

GRAPPA [14] is a parallel imaging technique that utilizes information about the spatial sensitivities of the receiver coils to directly calculate missing lines of k-space, then reconstructs images. The technique is an extension of the earlier method SMASH and later ones, such as AUTO-SMASH and VD-AUTOS-MASH, but with additional improvements. One difference between GRAPPA and SMASH is that GRAPPA reconstructs images coil by coil, and then combines them by a sum of squares, while SMASH reconstructs composite images. The benefit is that SNR can be improved by a factor of $\sqrt{N_c}$ compared with SMASH and AUTO-SMASH. The principle that underlies both SMASH and GRAPPA is that linear combinations of the complex coil sensitivities can provide the spatial encoding information that would normally be provided by a phase encoding gradient magnetic field. GRAPPA starts with estimating weights n using full-sampled low frequency k-space data F_l^{ACS}, called auto-calibrated signals (ACS) lines , for each receiver coil l.

$$\sum_{c=1}^{N_c} n_{k,l}^m F_k(k_x, k_y) = F_l^{ACS}(k_x, k_y + m\Delta k_y). \tag{2.29}$$

Notice that in Eq. 2.29, m is the number of shifted lines in k-space.

$$F_j(k_x, k_y + m\delta k_y) = \sum_l \sum_b n(j, b, l, m) F_l(k_x, k_y + bR_{GRAPPA}\Delta k_y). \tag{2.30}$$

The weights are then applied to fill in the missing k-space lines for each receiver coil j. R_{GRAPPA} is the acceleration factor and b is the index that count the number of phase-encoding lines that used in the reconstruction. This procedure repeated for every receiver coil j, after inverse Fourier transform, coil images are combined by sum of squares. GRAPPA was later improved, and the size of the kernel used for determining the weights was expanded to 2D including frequency encoding k_x [65] and even 3D include both frequency encodings and temporal direction [28]. In Figure 8 an example of a 2D 5×4 kernel is shown. The GRAPPA reconstruction can be

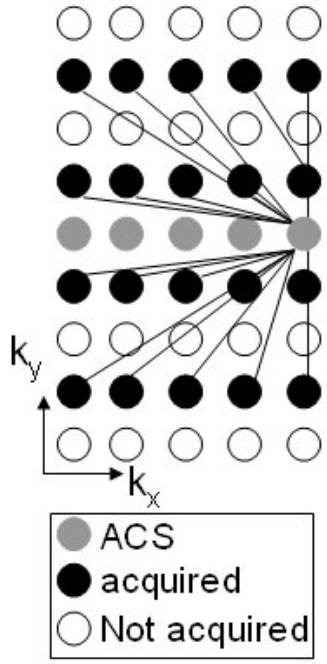

Figure 8: Sampling pattern with illustration of kernel with size of 5×4.

written as:

$$F_j(k_x, k_y + m\delta k_y) = \sum_{l}^{N_c} \sum_{a=-2}^{2} \sum_{b=-2}^{1} n(j, b, l, m) F_l(k_x + a\Delta k_x, k_y + br\Delta k_y). \quad (2.31)$$

One strength of GRAPPA is that it does not require explicit calculation of coil sensitivities, excluding the risk of involving misregistration errors with the pre-scan used to compute the coil maps. However, GRAPPA does not provide an analytical solution but instead an approximate solution from a least-square fitting.

2.5.2 rFOV methods (UNFOLD, Noquist, *k-t* BLAST)

UNFOLD [46] exploits the property that the outer portion of the FOV is relatively static. Taking $R = 2$ for example, k-space is undersampled by a factor of 2 at each time frame (Fig. 9). This leads to a one-half reduction of the FOV and a subsequent twofold aliasing of the image contents. Since k-space data are collected at the odd or even lines at alternate temporal frames, the aliased portion of the image contents alternates between positive and negative signs at successive time frames. As a result,

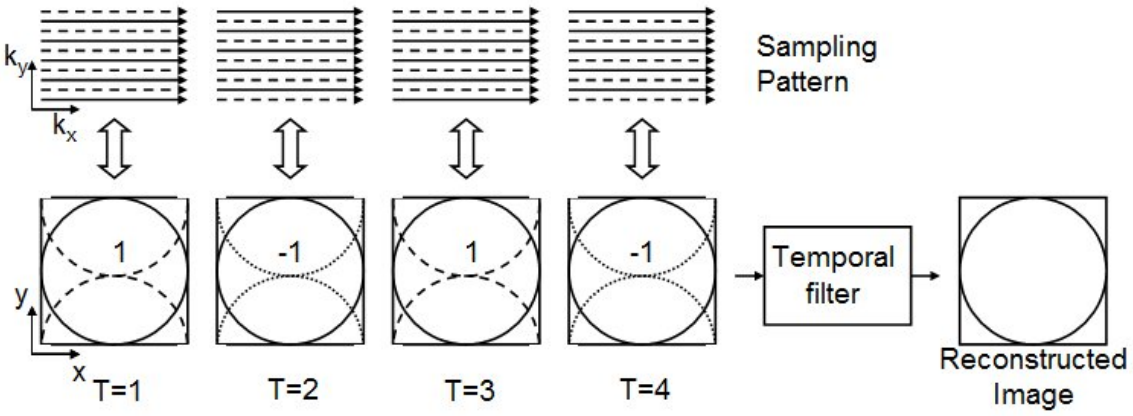

Figure 9: UNFOLD sampling pattern and temporal filtering for removal of reduced FOV alias artifacts.

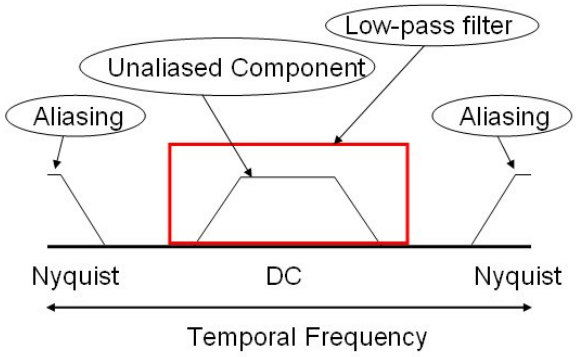

Figure 10: The aliased components can be removed by a low-pass filter.

the aliased signal is shifted to the high temporal frequency and can be separated from the unaliased portion by low-pass filter (Fig. 10) along the temporal axis. The main assumption in UNFOLD is that the aliased parts of the image in *y-f* space do not overlap with the original one, since aliased components are static regions which do not show big motion in temporal domain. In practical situations, this assumption is difficult to meet, therefore the size of the temporal-frequency filter must be carefully chosen to balance the trade-off between noise and signal loss (which may appear as artifacts).

Noquist: If part of the FOV does not change over time, we can define the sizes of the static and dynamic portions of the FOV as N_S and N_D: $N = N_S + N_D$. If these sizes are known at acquisition (e.g., estimated from manual or automated observations in scout images), this allows us to reconstruct the static region only once for the entire sequence (Fig. 11). The image vector f at a single time frame t can be partitioned as $f = \begin{bmatrix} f_S & f_{t,D} \end{bmatrix}^T$. Superscript T denotes transposition. The corresponding Fourier matrix can be similarly partitioned as $M = \begin{bmatrix} M_S & M_D \end{bmatrix}$. Data F_t for all T time frames indexed by t ($t \in 0, 1, \cdots, T-1$) may be concatenated into a single vector F:

$$\begin{bmatrix} F_0 \\ F_1 \\ ... \\ F_{T-1} \end{bmatrix} = \begin{bmatrix} M_S & M_D & 0 & ... & 0 \\ M_S & 0 & M_D & ... & 0 \\ ... & ... & ... & ... & ... \\ M_S & 0 & 0 & ... & M_D \end{bmatrix} \begin{bmatrix} f_S \\ f_{0,D} \\ f_{1,D} \\ ... \\ f_{T-1,D} \end{bmatrix} = M_{Noquist} f \tag{2.32}$$

The image sequence f is expressed as a vector, which concatenates the static portion of image followed by the dynamic portion for each time frame. is defined as the reduced number of phase encoding samples, which should be equal for each time frame to ensure equidistant temporal sampling, so $N_{data} = N_{sample\_nq} T$. Since the static part f_s is only reconstructed once in Noquist, the total dynamic image size is

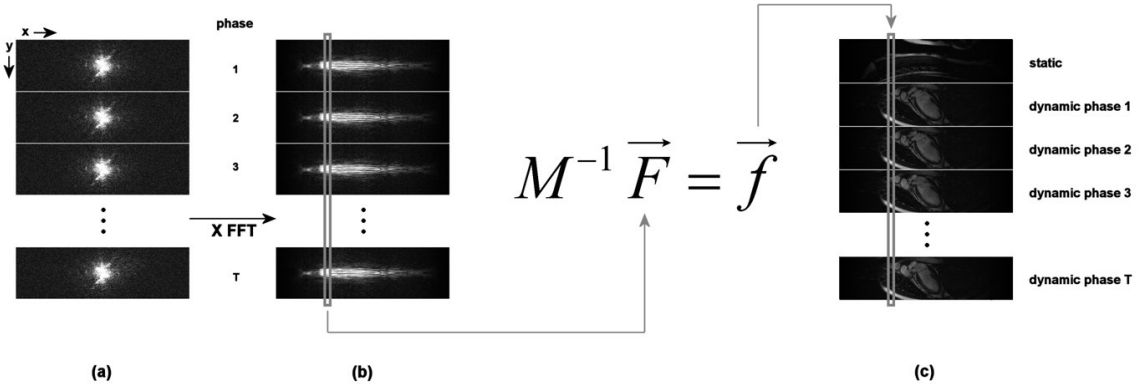

Figure 11: Schematic overview of the Noquist reconstruction.

$N_{pixels} = N_S + N_D T$. If the system matrix $M_{Noquist}$ with total size $N_{data} \times N_{pixels}$ is square, the image is reconstructed by multiplying the data F with its inverse:

$$f = M_{Noquist}^{-1} F. \tag{2.33}$$

More generally, for over- or under-determined systems, the matrix inversion M^{-1} may be replaced by a Moore-Penrose pseudo-inverse $M^{\dagger}$ [1]. Exact solutions may exist for fully- or over-determined systems ($N_{data} \geq N_{pixels}$). It follows that

$$N_{sample\_nq} \geq N_S/T + N_D. \tag{2.34}$$

Thus, the corresponding acceleration rate $R_{nq} = N/N_{sample\_nq}$ is maximized at

$$R_{nq} = N/(N_S/T + N_D). \tag{2.35}$$

***k-t* BLAST** [62] takes advantages of the observation that signals from a MR image series can be represented in a compact fashion in *x-f* space (where x and f denote space and temporal frequency) due to slow varying motion along temporal direction. Most of the signal is concentrated in a small portion of *x-f* space, while large areas contain little to no signal. *k-t* BLAST (Fig 12) subsamples k-space lines in *k-t* space (spatial frequency and time). Skipping k-space lines result in overlapping of the signal replicas in *x-f* space, shown only little overlapping of the signal replicas.

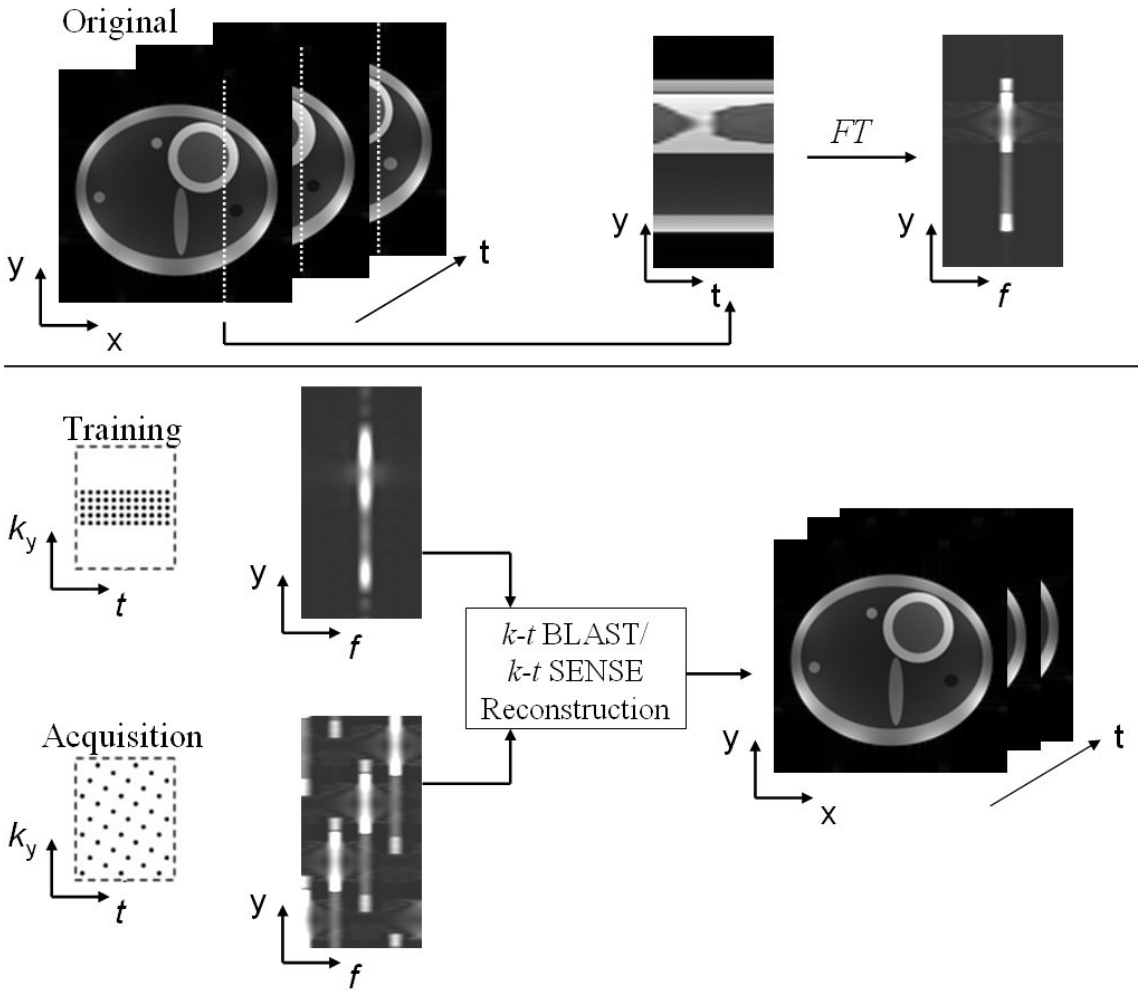

Figure 12: k-t BLAST/k-t SENSE reconstruction steps for the training stage and image reconstruction stage.

By also acquiring a separate low-resolution training data set, an estimate of the distribution of the signal and aliased signal in x-f space is obtained. This estimate can be used to separate the true signal from the aliased copies. The true signal is retrieved from aliased components.

2.5.3 Partial Fourier Methods(POCS implementation)

One implementation [15] of Partial Fourier technique is to use the Projection onto Convex Sets (POCS) algorithm. The POCS algorithm provides a simple and computationally efficient way to utilize various linear and nonlinear constraints in image reconstruction. The algorithm operates by iteratively transforming between the image domain and the spatial frequency domain to estimate the missing k-space data by applying the phase constraint (Fig. 13).

For a dynamic image sequence, we define the k-space MR signal $F(k,t)$, sampled k-space data $F_{sampled}(k,t)$ and image space signal for ith iteration $f_i(x,t)$. We construct the following two convex sets, here convex set Ω_p contains all images satisfying the phase constraints $\varphi(x,t)$, Ω_k contains sampled k-space data from all images for ith iteration equal to the original sampled k-space data from MRI scan:

$$\begin{aligned} \Omega_p &= \{f_i(x,t) | \arg\{f_i(x,t)\} = \varphi(x,t)\} \\ \Omega_k &= \{f_i(x,t) | FT\{f_i(x,t)\} = F_{sampled}(k,t)\} \end{aligned} . \tag{2.36}$$

The reconstruction procedure is like follows:

1. Symmetric low frequency k-space views are used to calculate phase constraints $\varphi(x,t)$.

2. Zero-fill missing k-space data and apply inverse Fourier transform to get initial estimated images $f_0(x,t)$.

3. In each iteration, constrain the phase of resulting image to $\varphi(x,t)$ by multiplying the absolute value of the current estimate with $\varphi(x,t)$.

4. Apply a FT to get estimated full-sampled k-space for each image and replace each acquired view by the original sampled data.

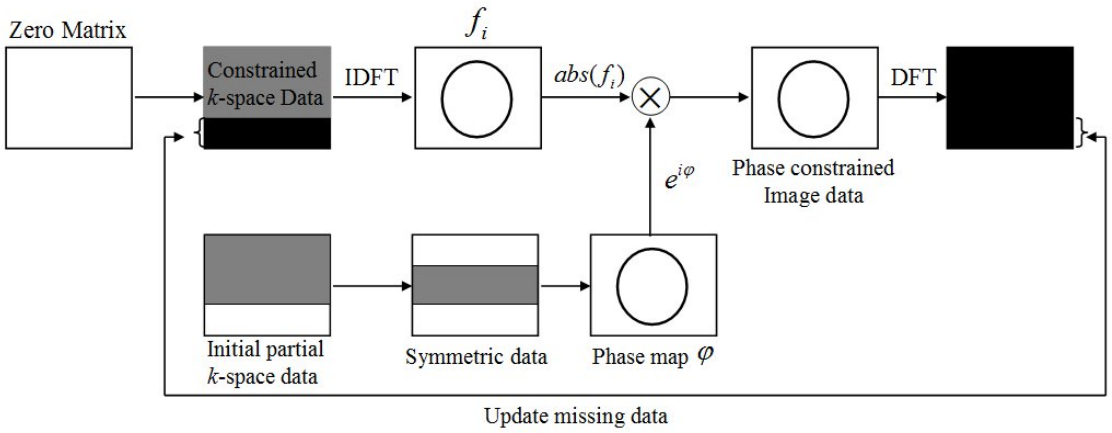

Figure 13: POCS implementation of Partial Fourier technique.

5. Apply inverse Fourier transform and go back to step 3 until convergence or maximum number of iteration reaches.

2.5.4 Combined methods (TSENSE, *k-t* SENSE)

TSENSE [34, 35]: combines UNFOLD ($R = 2$) with SENSE ($R = 2$) to achieve a total acceleration factor of 4, relative to conventional full-grid acquisition. First, interleaved k-space sampling shifts two aliased components to the temporal band edge; the aliases are subsequently removed using a low pass Fermi filter. Then the two remaining aliasing components in DC frequency can be separated by SENSE with two or more coils. TSENSE's undersampled acquisition scheme, adopted from [35], repeats every other frame. It is illustrated in Fig 2.13 (phase encoding 2,6,10, for odd frames and 4,8,12 for even frames).

***k-t* SENSE** [62]: is similar to k-t BLAST, but it additionally takes into account the spatial encoding effect of coil sensitivity, if multiple receiver coils are used for signal reception. In k-t BLAST, the reconstruction does not incorporate information from coil sensitivity encodings, and reconstructed images from multiple receiver coils are combined after reconstruction by root of mean square. In contrast, coil sensitivity

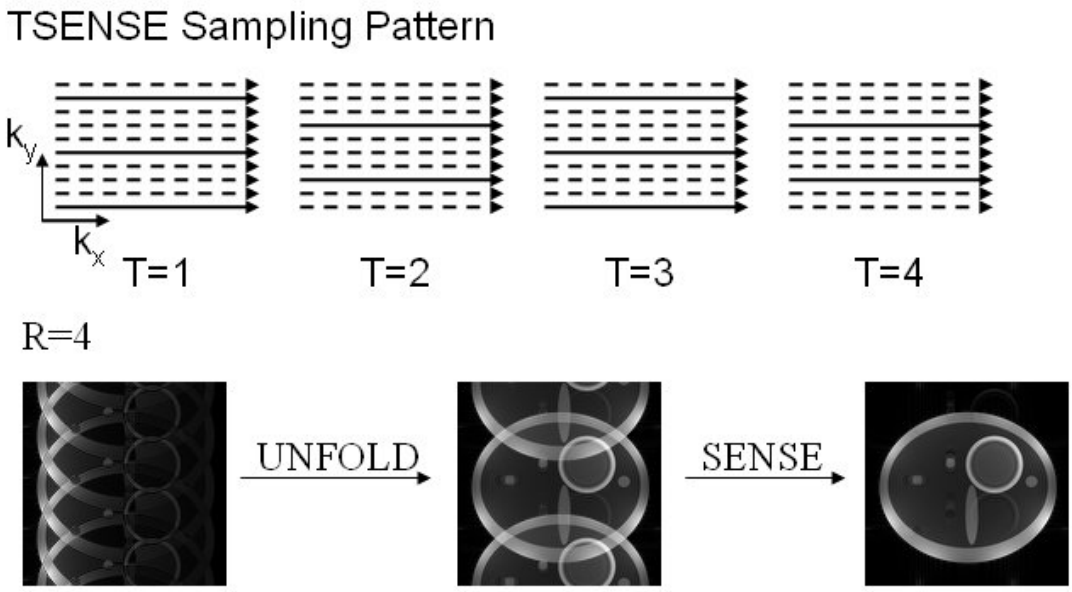

Figure 14: TSENSE sampling pattern with $R = 4$ and TSENSE reconstructed figures shown aliased images, reconstructed image using UNFOLD, reconstructed image using SENSE after UNFOLD reconstruction.

information is incorporated directly in the k-t SENSE reconstruction to aid the unaliasing process. k-t SENSE (Fig. 12) is essentially a combination of k-t BLAST and SENSE, therefore achieves higher speed gain. The principle of k-t BLAST was introduced earlier in section 2.5.2. Time-invariant coil sensitivities are estimated from the temporally averaged undersampled data, i.e., no additional calibration scan is required to obtain the coil sensitivity maps.

Partial Fourier Partially Parallel Imaging [4]: combined techniques of partial Fourier and parallel imaging method using a constrainted reconstruction. The low frequency reference lines for can be used to estimate both coil sensitivities and phase maps.

The parallel imaging methods can be written as:

$$F = Mf, \tag{2.37}$$

where M is the forwarding matrix, F is the acquired k-space sampleds from multiple

coils and f is the vector of image pixles to be reconstructed. Partial Fourier exploit a known Hermitian data symmetry. In the image domain, Hermitian symmetry implies that the object is pure real, which means $Im\rho = 0$. This property can be incorporated into Eq. 2.37 by separating into real and imaginary parts and forming a constrained least squares equation,

$$\begin{bmatrix} Re\{\mathbf{F}\} \\ Im\{\mathbf{F}\} \\ 0 \end{bmatrix} = \begin{bmatrix} Re\{\mathbf{M}\} & Im\{\text{-}\mathbf{M}\} \\ Im\{\text{-}\mathbf{M}\} & Re\{\mathbf{M}\} \\ 0 & \lambda I \end{bmatrix} \begin{bmatrix} Re\{\boldsymbol{f}\} \\ Im\{\boldsymbol{f}\} \end{bmatrix} \tag{2.38}$$

where I is the identity matrix and λ is a scalar used for regularization that allows a trade-off between noise amplification from PPI with phase artifacts from PF. The phase correction is implicit in M.

2.6 Discussion

Reduced-data imaging methods have been widely used in clinical applications. However, important challenges remain. For example, theoretically the maximum sampling rate reduction factor for parallel imaging methods is limited by the number of independent channels [52, 67]. However, this maximum is usually not achieved due to noise amplification or imperfections in the sensitivity maps. Therefore, image quality reconstructed by SENSE-like parallel imaging methods which requires explicit calculations of sensitivity maps, relies on accurate estimate of coil sensitivities. The sensitivity maps are commonly estimated by a pre-scan prior to image acquisition, which prolongs the preparatory scan time and can introduce reconstruction artifacts due to spatial inconsistency between the pre-scan and the acquisition data. For k-t BLAST and k-t SENSE, an increased amount of training data also increases sensitivity to misregistration of the training data. GRAPPA-like parallel imaging methods use coil information in a slightly different way, in that it is not extracted explicitly, but the solutions are approximation resulting from a least-squares optimized fit to

spatial harmonics. Another influential factor is signal to noise (SNR) loss. The SNR loss is due to two factors. One is that SNR loss is proportional to the square root of the acceleration factor, which means the higher acceleration factor, the more SNR loss will occur. Another factor is called geometry factor (g-factor), which depends on number and configuration of coils. In practice, more coils than the acceleration factor are used to guarantee an overdetermined system and improve the condition of the matrix inversion for image reconstruction. The investigation of the intrinsic limits of SNR for parallel imaging by Ohliger et al [52] concluded that the signal and the noise are necessarily coupled. For higher acceleration factors above a certain limit, the g-factor increases exponentially, leading to very high SNR levels. In response to these observed limits, some alternative strategies using prior information or numerical tools have been developed to control the level of noise and artifact amplification in the reconstructed image. One strategy is use regularization, such as truncated singular value decomposition (SVD) [27] or Tikhonov regularization [41]. Another strategy is use a filter to filter the high frequency noise. For example, UNFOLD uses a Fermi filter and k-t BLAST and k-t SENSE essentially employ a filter designed from the training set to get rid of the aliased component as well as noise. However, these methods lead to a reduced noise level at a cost of increased aliasing artifacts. In sum, all reduced-data imaging methods discussed above carry a price for the higher imaging speed, in comparison with conventional fully-sampled imaging. This may be a signal-to-noise ratio (SNR) penalty, reduced spatial-temporal resolution, or a combination of these two. Depending on the "native" SNR and resolution of the comparable fully-sampled conventional scan, a method with the desired characteristics may be selected. Methods with SNR penalties may sometimes be improved by regularization techniques to shift their characteristics towards better problem conditioning, in turn often trading off true resolution. The converse does not hold in

all cases: methods which intrinsically rely on filtering or regularization may not always be "unregularized" to regain better resolution. If image resolution is the most critical criterion, reduced-data methods which allow full or nearly full preservation of "full-grid resolution" may present the preferred approach. SENSE, SPACE-RIP, and Noquist all possess such characteristics. Interestingly, none of the proposed techniques to combine rFOV and parallel imaging are capable of reconstructing the image at the same spatiotemporal resolution as the fully sampled grid, due to the use of low-pass filters, interpolation, or embedded regularization, even in cases where the reduced data set still represents an overdetermined inversion problem.

2.7 Summary

In summary, MRI signals arise from protons, primarily water molecules, in the body. The protons precess around the direction of the static magnetic field. A radiofrequency field tips the proton's alignment and produces signals which can be detected by receiver coils. 3-D spatial information can be obtained with magnetic field gradients in each direction. An inverse Fourier transform is applied to produce the MR images. A brief overview of reduced-data MR imaging methods was given in this chapter and differences and similarities as well as advantages and disadvantages have been addressed. The theory underlying reduced-data image acquisition has established a central tradeoff between scan time and image quality. It demonstrates that reduced-data imaging reconstruction techniques can be viewed as solving a constrained linear inverse system. An important remaining challenge is development of a technique to combine rFOV and parallel imaging, capable of preserving the full spatiotemporal resolution of the "unaccelerated scan". A solution to this challenge is the central theme of this research.

CHAPTER III

PINOT:A TIME-RESOLVED PARALLEL MRI METHOD WITH A REDUCED DYNAMIC FIELD OF VIEW

3.1 Introduction

As discussed in chapter 2, all fast imaging methods carry a price for the higher imaging speed, in comparison with conventional fully-sampled imaging. This may be a signal-to-noise ratio (SNR) penalty, reduced spatial-temporal resolution, or a combination of these two. An important remaining challenge is development of a technique to combine rFOV and parallel imaging, capable of preserving the full spatiotemporal resolution of the "unaccelerated scan". This chapter introduces a novel method named PINOT (Parallel Imaging and NOquist in Tandem) [19, 18], which combines SPACE-RIP parallel imaging and the Noquist rFOV method. PINOT does not apply any filter or interpolation, therefore preserves the edge details, with flexibility of improving SNR by regularization. In the next section, we introduce theoretical aspects of PINOT, followed by improvements and extensions. Experimental results on computer simulated data and retrospectively sub-sampled full-grid magnetic resonance imaging (MRI) data are put in further perspective by a comparison of PINOT with the individual SPACE-RIP and Noquist methods, and by a comparison with TSENSE and k-t SENSE.

3.2 PINOT algorithm

We introduced the background of two fast imaging methods SPACE-RIP and Noquist in chapter 2. SPACE-RIP is a direct inversion of the weighted Fourier transform matrix, combined for all coils. Noquist also uses a direct inversion model combing

all temporal frames. To implement accelerated imaging using both sources of prior knowledge, these two model formulations can be combined naturally into the PINOT method.

$$F = M_{PINOT} f. \tag{3.1}$$

To alleviate the high computational cost of using direct matrix inversion, iterative reconstruction algorithms, such as conjugate gradient (CG) method [55] may be employed instead. The reconstructed image (column) vector f, with again the static region f_s only represented once, expands as

$$f = \begin{bmatrix} f_S & f_{0,D} & f_{1,D} & ... & f_{T-1,D} \end{bmatrix}^T. \tag{3.2}$$

The data vector F contains acquired phase encoded data k for all time frames and coils:

$$F = \begin{bmatrix} F_{0,0} & F_{0,1} & ... & F_{0,C-1} & ... & ... & F_{T-1,0} & F_{T-1,1} & ... & F_{T-1,C-1} \end{bmatrix}^T. \tag{3.3}$$

k-space data F are now indexed by the time frame t as well as the coil c. The matrix is the forward system matrix M_{PINOT} for a given readout axis location. Its structure is similar to $M_{Noquist}$, but is expanded for all coils and weighted by sensitivity maps:

$$M_{PINOT} = \begin{bmatrix} M_S S_0 & M_D S_0 & 0 & ... & 0 \\ M_S S_1 & M_D S_1 & 0 & ... & 0 \\ \vdots & \vdots & \vdots & \vdots & \vdots \\ M_S S_{C-1} & M_D S_{C-1} & 0 & ... & 0 \\ M_S S_0 & 0 & M_S S_0 & ... & 0 \\ \vdots & \vdots & \vdots & \vdots & \vdots \\ M_S S_{C-1} & 0 & M_D S_{C-1} & ... & 0 \\ \vdots & \vdots & \vdots & \vdots & \vdots \\ M_S S_0 & 0 & 0 & ... & M_D S_0 \\ \vdots & \vdots & \vdots & \vdots & \vdots \\ M_S S_{C-1} & 0 & 0 & ... & M_D S_{C-1} \end{bmatrix} \tag{3.4}$$

The size of M_{PINOT} is $(TN_cN_{sample\_PI}) \times (TN_D + N_S)$. where N_{sample_PI} denotes the number of phase encodings sampled for each time point. For a solvable system the number of rows must again exceed the number of columns, thus

$$(TN_cN_{sample\_PI}) \geq (TN_D + N_S) \tag{3.5}$$

With R_p and R_{nq} defined as in Eqs. 2.27 and 2.35,this implies a minimum number of samples per time frame

$$N_{sample\_PI} = N/R_{PINOT} = N/R_pR_{nq} \geq (N_D + N_S/T)/N_C \tag{3.6}$$

for a solvable system. PINOT multiplicatively combines the maximum acceleration rates from parallel imaging and Noquist: $R_{PINOT} = R_pR_{nq}$. In order to maintain a solvable linear system of equations, the same data reduction limits apply as in the constituent methods.

All reduced-data methods have SNR loss to pay for the speed gain. One strategy to control the noise level in the reconstructed image is use regularization. To alleviate the noise amplification for the PINOT method, we implemented regularized PINOT (Eq. 3.7) using Tikhonov regularization [41]. The second term in Eq. 3.7 is the error from solution image and the prior estimate. A low resolution reference (25% of full resolution phase encoding lines) scan $f_{reference}$ is used as a prior estimate of the solution. The regularization parameter α was calculated using L-curve algorithm [24], which offers a trade-off mechanism between the error from prior knowledge (large α) or the error from unconditioned matrix inversion (small α).

$$\overline{f}_{regularization} = \arg\min_f \|M_{PINOT}f - F\|_2^2 + \alpha \|(f - f_{regularization})\|_2^2 . \tag{3.7}$$

3.3 PINOT Sampling Scheme

As discussed in [3] for Noquist, different sampling schemes can be designed for reduced sampling of k-t space. Not all patterns will yield a non-singular and well-conditioned

forward matrix M. Similarly, reduced sampling for parallel imaging may be performed in different ways [54, 37]. Optimization of sampling schemes is a complex and important problem, which depends on a multitude of parameters such as coil sensitivity maps, spatiotemporal image characteristics, and other factors. PINOT further compounds this complexity by combining methods. In this work we have adopted heuristic subset selection methods from Noquist and SENSE/SPACE-RIP, which have been shown to yield stable results for these individual techniques under a variety of conditions [3, 37, 49], and combined these to form a well-conditioned matrix M_{PINOT}. A stable subset selection method for Noquist with 50% dynamic FOV acquires even k-space lines in every frame and distributes acquisition of odd k-space lines across the phases of the cardiac cycle in a regular "stairwell" pattern (Fig. 15a). Similarly, a common subset for both SPACE-RIP and SENSE to sample with $R_p = 2$ is to simply acquire every other phase encoding view [54, 37] (Fig. 15b). For PINOT these sampling schemes are combined in a straightforward manner to form the pattern shown in Fig. 15c, which can readily be extended to larger grid sizes.

3.4 Experiments

We designed five experiments to demonstrate and evaluate PINOT's feasibility and performance. We start to test PINOT with computer-simulated data to simulate different scenario. Using computer-simulated data, PINOT is tested with noiseless and noisy situation, with different static and dynamic regions and to measure the SNR quantitatively. After that, we tested PINOT on two real MRI data sets. To validate PINOT sampling scheme, we compare the designed PINOT sampling scheme with other two commonly used sampling schemes from TSENSE and k-t SENSE. To evaluate PINOT's performance, we compared PINOT with TSENSE and k-t SENSE methods. The last one is to test PINOT with regularization technique.

Experiment 1: Computer-simulated data reconstruction

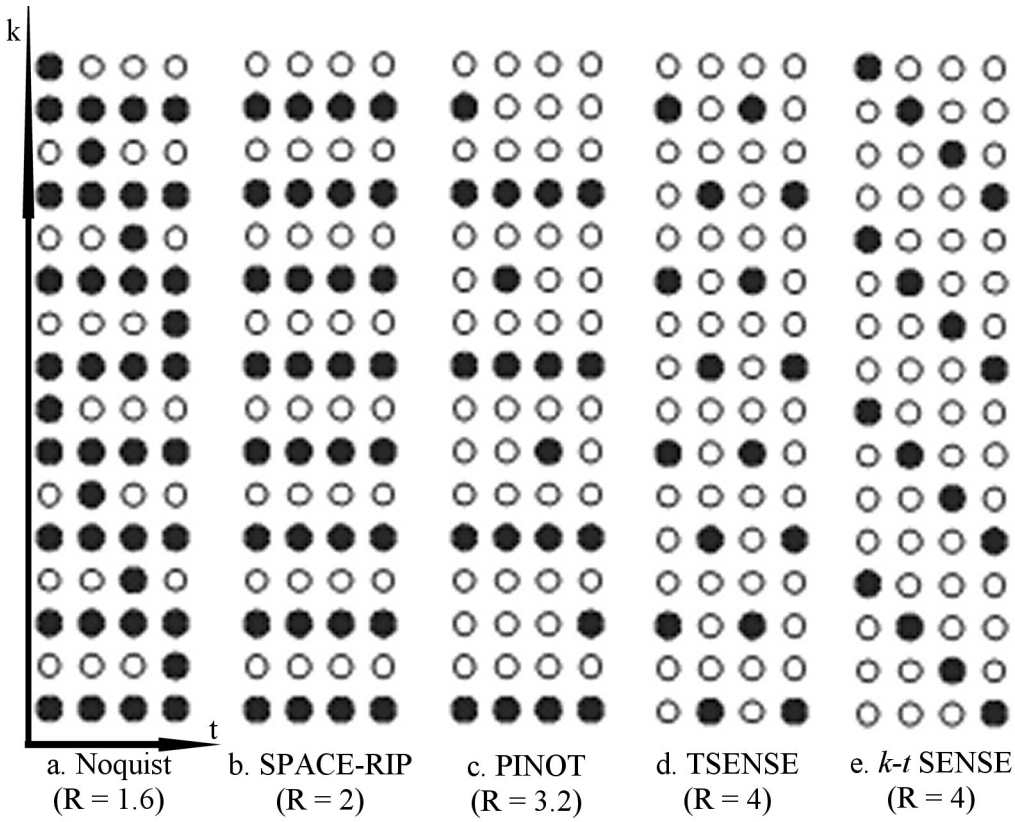

Figure 15: Reduced sampling schemes for an example with 16 phase-encodings and 4 frames for (a) Noquist with 50% static FOV, (b) SENSE or SPACE-RIP, (c) PINOT, (d) TSENSE (not accounting for auto-calibrated lines), and (e) k-t BLAST/k-t SENSE (not accounting for training data). The horizontal axis represents time and the vertical axis represents the phase encoding direction. The reduction factor R for each method is shown.

In the first experiment, PINOT was initially tested using noiseless computer simulated data. For reference, results for the same data with the individual SPACE-RIP and Noquist methods are also shown. To be more realistic, Gaussian noise was added to the computer simulated data and sensitivity maps with uniform noise levels across all receiver channels and phase encoding views, at levels corresponding to 1% of highest RSS image intensity, resulting in SNR in selected ROI (shown in Fig. 17a) of $19.1482dB$, $17.6382dB$ and $15.4962dB$ respectively for ROI 1,2 and 3 respectively. PINOT ($R = 3.75$) was compared with corresponding SPACE-RIP and Noquist quantitatively [61, 9] (see implementation details below in Quantitative Performance Evaluation). Mean signal intensity and noise distribution images are shown. Normalized noise distributions of three methods are compared and shown in histogram, displayed separately for the static and dynamic region. To test the PINOT reconstruction robustness against different choices of static/dynamic FOV regions, PINOT reconstructions were performed at different acceleration factors, with varying static and dynamic regions ($R = 2.61$, 3.75 and 6.67). Noise distributions of different reduction factors are shown in histogram as well. Condition numbers, as a measure of how well-conditioned the M_{PINOT} is, are calculated with different reduction factors ($R = 3.75$, 6.67 and 13.33), reconstruction errors are defined as the Euclidean norm of difference between the reconstructed image and full-grid image.

Experiment 2: Real MRI data reconstruction

In the second experiment, we tested PINOT on two real MRI data sets, in comparison with corresponding SPACE-RIP and Noquist for the first dataset in both spatial and temporal dimension. The second dataset showed PINOT reconstructions for different temporal frames.

Experiment 3: Sampling scheme comparison

The third experiment implemented TSENSE and *k-t* SENSE for comparison with

PINOT with both simulated and real MRI data. To evaluate temporal fidelity, temporal plots of signal intensity along two lines will be shown as well. TSENSE and *k-t* SENSE mean signal intensities are compared with PINOT along the spatial and temporal dimensions, and the noise distribution histogram of the three methods are shown as well. The computational cost of three different methods is also analyzed.

Experiment 4: Comparison of TSENSE and k-t SENSE [22]

In the fourth experiment, we compared noise level of the PINOT reconstructions using the default subset sampling schemes with the TSENSE, and *k-t* SENSE sampling schemes (Fig 3.1d,e). Additionally, two criteria, condition number and sum of squared errors (SSE), were shown to demonstrate the numerical stability of PINOT encoding matrix associate with different sampling schemes. Assuming added Gaussian distributed noise and the least squared reconstruction, SSE [31, 56] of the PINOT reconstructed image is measured using $E_{(M_{PINOT})} = trace(M_{PINOT}^{H}\Psi M_{PINOT})^{-1}$. Here Ψ is the receiver noise matrix and considered as identity matrix for simplicity.

Experiment 5: PINOT with regularization

In the last experiment, we compared PINOT with/without regularization under two different reduction factors 3.75 and 13.33 (75% static FOV for Noquist and $R_{np} = 4$). All experiments were computered in MATLAB $R2007a$ (The Mathworks, Natick, MA) on a QuadCore Xeon $2.66GHz$ workstation with 16GB of RAM running Linux.

Data:

Computer Simulated data: A time-resolved 2-D computer generated data set (see Fig. 16) was generated to simulate MRI acquisition of cardiac motion [3], with 120 frequency and phase encoding samples and 15 temporal frames. Four surface coils were simulated, located at each side of the FOV. The magnitude of the coil's sensitivity maps were calculated by the Biot-Savart law [6]. Geometric phase warp patterns (differently angled linear warps) were applied to each complex sensitivity map to avoid unrealistic phase symmetry and the associated impact on the condition of the

inversion problem, as previously described by Kyriakos [37].

MRI data: Breath-held, prospectively gated Steady-State Free Precession (SSFP) cardiac MRI scans (Fig. 19, 20) were used to evaluate PINOT by a protocol approved by the Institutional Review Board. The full Cartesian k-space data were used as "truth" images for comparison. Data sets are from a GE 1.5T TwinSpeed scanner (R12M4) using an 8-element cardiac coil. For a 2-chamber view cine MRI scan, a FIESTA/FastCARD cine SSFP sequence was used with slice thickness 8 mm, $TR = 4.4$ms, $TE = 1.5$ ms, flip angle 45°, 192 phase encodings, 224 read-out samples, and 12 temporal frames. Sensitivity maps were estimated from the same data to simulate perfectly co-registered maps. We note that this approach introduces a positive bias in the observed SNR, but eliminates complications from misregistration, which may otherwise be confused with residual artifacts due to the method itself. A short axis MRI scan was acquired using a FIESTA/FastCARD cine SSFP sequence. Scan parameters: $TE = 2.0$ ms, $TR = 4.1$ ms, flip angle = 45°, FOV = 350×350 mm, slice thickness = 12 mm, 8 views per segment, 202 phase encoding views (zero-padded to 224), 256 read-out samples, and 16 temporal frames. For this acquisition a separate reference scan was obtained with identical scan parameters to estimate sensitivity maps. Sensitivity maps were calculated from reference scan data. Both sensitivity maps were estimated as follows: first the (50%) highest frequency k-space views for each coil were removed. An inverse Fourier transform (FT) was applied to obtain the smoothed coil image after applying a smoothing filter. These images were subsequently divided by the root-sum-of squares (RSS) of all coil images to estimate the sensitivity maps.

Comparison of PINOT, k-t SENSE and TSENSE: In order to compare PINOT with TSENSE [35] and k-t SENSE [62], the reconstruction problems were dimensioned to achieve approximately the same acceleration factors for all three methods. To ensure a fair comparison the same sensitivity map was used for all three methods.

Modified TSENSE [35] was implemented combining UNFOLD ($R = 2$) with SENSE ($R = 2$). With the simulation data, 10 additional training data profiles were acquired for *k-t* SENSE with reduction factor 4. For PINOT, a SENSE reduction factor of 2 was used, and a 50% dynamic FOV for Noquist. These parameters yield reduction factors of 4 for TSENSE, *k-t* SENSE and 3.75 for PINOT with simulated data. In a short axis MRI scan, the same settings were applied with corresponding reduction factors 4 for TSENSE, *k-t* SENSE and 3.73 for PINOT. Extensions of the sampling patterns of Fig. 15 were used for all reconstructions.

Quantitative Performance Evaluation: As introduced in references [61, 9], we define SNR of each pixel in the reconstructed image as the ratio of the pixels mean value to its standard deviation across several acquisitions differing only in noise. In our experiments, Gaussian noise was added to the real and imaginary parts of the simulated data, with noise level comparable with that measured in real MR images. The reconstruction process was repeated 200 times for different realization of the random noise. The mean signal intensity is calculated by taking the average of the all reconstructed magnitude images for each pixel. The noise level is then calculated by taking the standard deviation in the resulting image magnitudes for each pixel, divided by the square root of reduction factor to normalize for different acceleration factors.

3.5 Results

3.5.1 Experiment 1: Computer simulated data Reconstruction

In the first experiment, PINOT was initially tested using noiseless computer simulated data. For reference, results for the same data with the individual SPACE-RIP and Noquist methods are also shown. To be more realistic, Gaussian noise was added to the computer simulated data and sensitivity maps with uniform noise levels across all receiver channels and phase encoding views, at levels corresponding to

1%of highest RSS image intensity, resulting in SNR in selected ROI (shown in Fig. 17a) of 19.1482dB, 17.6382dB and 15.4962dB respectively. PINOT ($R = 3.75$) was compared with corresponding SPACE-RIP and Noquist quantitatively [61, 9] (see implementation details in Quantitative Performance Evaluation). Mean signal intensity and noise distribution images are shown. Normalized noise distributions of three methods are compared and shown in histogram, displayed separately for the static and dynamic region. To test the PINOT reconstruction robustness against different choices of static/dynamic FOV regions, PINOT reconstructions were performed at different acceleration factors, with varying static and dynamic regions ($R = 2.61$, 3.75 and 6.67). Noise distributions of different reduction factors are shown in histogram as well.

Figure 16 shows experimental results comparing SPACE-RIP, Noquist and PINOT for noiseless computer simulated data. We used reduction factors of $R_p = 4$ for SPACE-RIP (Fig. 16c) and $R_{nq} = 1.88$ for Noquist (Fig. 16d) with 15 frames and 50% dynamic FOV. PINOT reconstruction (Fig. 16e) achieved a reduction factor of $R = 7.5$, or using only about 14 percent of phase encoding samples. Figure 15f shows the difference image (absolute intensity differences with the full-grid "true" image), scaled up by a factor of 1000 (The difference image is practically zero and that the reconstruction is practically perfect except for round-off errors). These experiments demonstrate PINOT reconstruction under ideal noiseless conditions.

With added Gaussian noise, the mean signal of magnitude and the noise distribution of SPACE-RIP ($R = 2$), Noquist ($R = 1.88$) and PINOT ($R = 3.75$) are presented in Fig 17. As in Noquist [3], PINOT noise distribution shows higher noise levels in the dynamic FOV. As in parallel imaging [54] we observe higher noise levels at locations with low coil sensitivity than at locations with high sensitivity. Both Noquist and PINOT showed a similar two peak shape with wider range noise distributions compared with SPACE-RIP. This occurs because the Noquist and PINOT

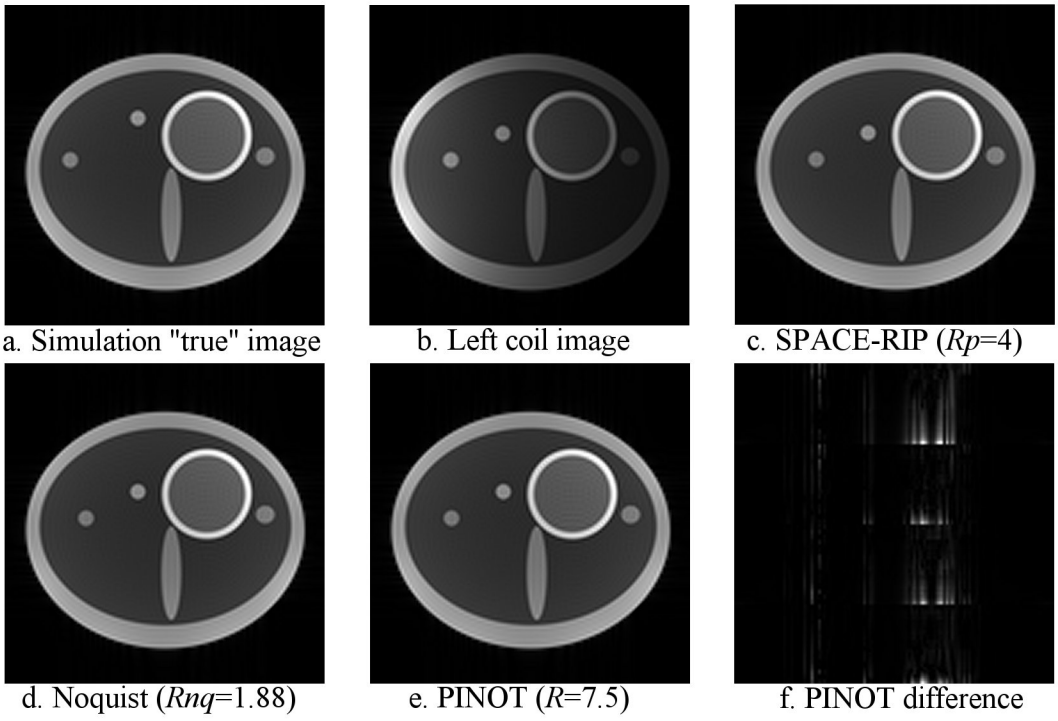

Figure 16: The figures show the 1st frame of 15 from a computer simulated sequence for: (a) full-grid reconstructed "true" image, (b) left surface coil computer simulated image, (c) SPACE-RIP reconstruction with reduction factor 4, (d) Noquist reconstruction with 50% centrally located dynamic FOV (reduction factor $R = 1.88$), (e) PINOT reconstruction (reduction factor $R = 7.5$), and (f) is the amplified absolute difference between PINOT and full-grid reconstruction, scaled up by a factor of 1000. Differences between truth and Noquist and SPACE-RIP reconstructions were smaller yet than for PINOT.

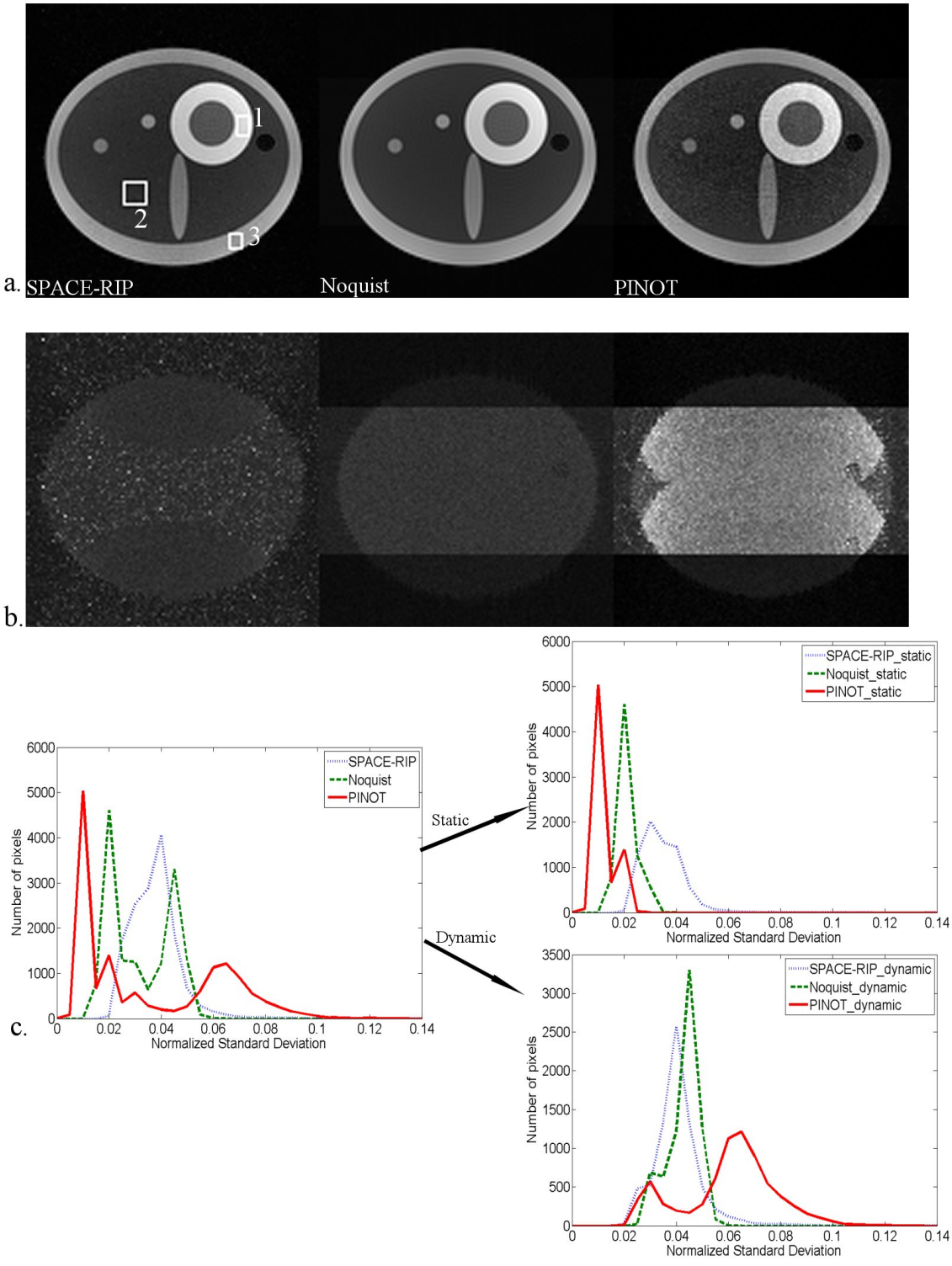

Figure 17: Reconstructed images (frame 7) of SPACE-RIP, Noquist, PINOT, showing (a) the mean signal intensities, (b) the normalized noise standard deviations and (c) corresponding histogram within full reconstructed images, compared with only the static and dynamic reconstructed regions images.

Table 1: Condition number range, mean and reconstruction error for PINOT with reduction factors ($R = 3.75$, 6.67, 13.33).

R_{PINOT}	$R_{SPACE-RIP}$	$R_{Noquist}$	Condition number range	Condition number mean	Reconstruction Error (frame 1)
3.75	2	1.875	[7.214 26.589]	12.472	11.216
6.67	2	3.33	[12.340 31.119]	21.819	14.3897
13.33	4	3.33	[132.17 1334.65]	590.382	93.4515

reconstruction results in different noise level in static and dynamic region. The explanation is confirmed by the histograms displaying the static region and dynamic region normalized noise distribution separately.

PINOT reconstructions were tested with 3 different reduction factors ($R = 2.61$, 3.75, 6.67), corresponding $R_p = 2$ and 25%, 50% and 75% static FOV for Noquist (Fig. 18). Even with noisy data and sensitivity maps, PINOT is still able to capture image changes at sharp edges and preserves spatiotemporal resolution well, but at a cost of reduced SNR, especially in the dynamic region. Fig. 18b showed the noise level histograms for PINOT with different acceleration factors. Table 1 shows the means, ranges of condition numbers observed in MPINOT and reconstructed errors associated with different acceleration factors ($R = 3.75$, 6.67, 13.33). Clearly, the higher the reduction factor is, the less well-conditioned M_{PINOT} is, the noisier PINOT reconstruction is.

3.5.2 Experiment 2: Real MRI data Reconstruction

In the second experiment, we tested PINOT on two real MRI data sets, in comparison with corresponding SPACE-RIP and Noquist for the first dataset in both spatial and temporal dimension. The second dataset showed PINOT reconstructions for different temporal frames.

A PINOT reconstruction of a cardiac MRI scan with a two-chamber view is shown

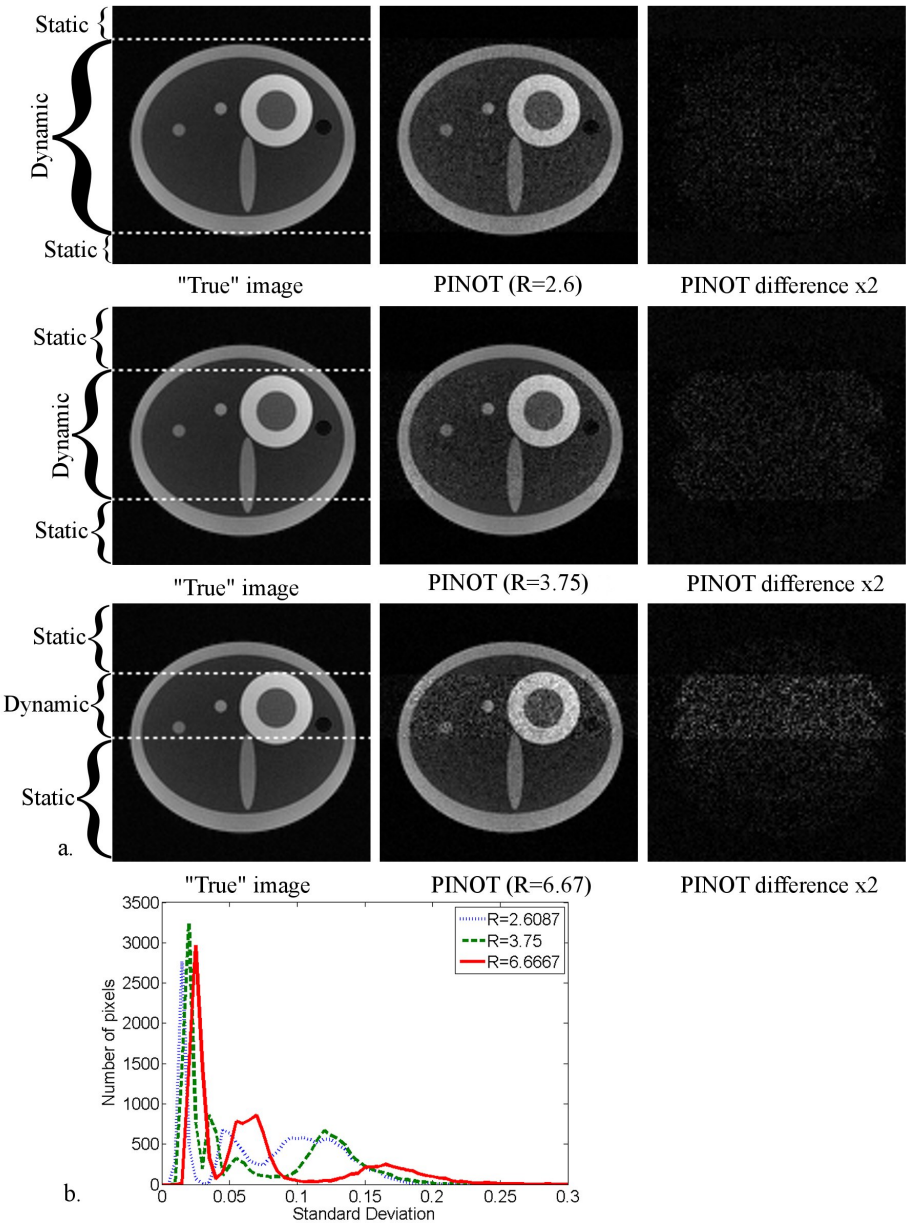

Figure 18: (a) shows PINOT reconstructions of 7th frame from the computer simulated images with noise. Each row includes: "true" image reconstructed using full samples, PINOT reconstruction with different reduction factor, and difference image. All reconstructions are shown at the same intensity scale. but intensities in the difference image are amplified by a factor of 2 to see the details. Static and dynamic regions for PINOT are marked in "true" images. (b) Histogram curves of the noise standard distribution for PINOT with PINOT reduction factors 2.6, 3.75, and 6.67.

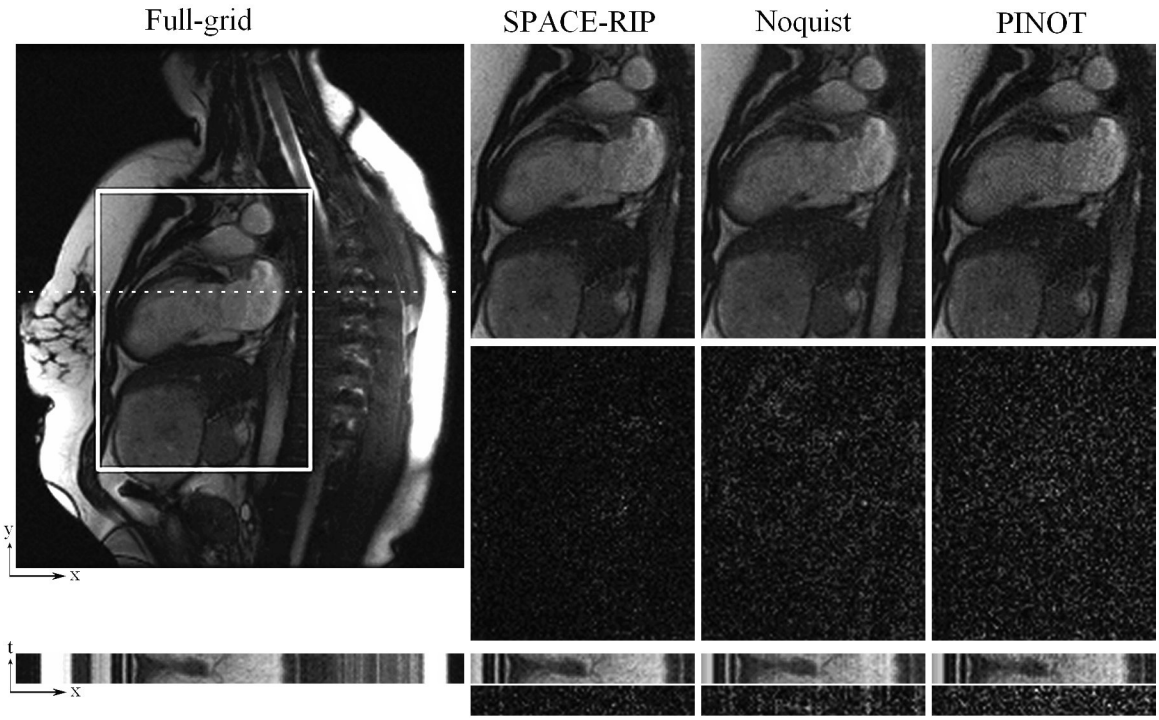

Figure 19: Comparison of experimental results of conventional full grid acquisition, SPACE-RIP reconstruction with a reduction factor of 2, Noquist reconstruction with 50% dynamic FOV (reduction factor is 1.85), and PINOT reconstruction with a reduction factor of 3.7 for real MRI data with a two-chamber long-axis view of the heart region (frame 1 of 12). Differences are shown at bottom with corresponding reconstructed ROI images. Temporal direction and difference are shown below full-grid image and each reconstructed image. The differences are scaled by a factor of 5 to reveal details.

in Fig. 19. The conventional (a), SPACE-RIP (b), Noquist (c), and PINOT (d) reconstructions used 192, 96, 104, and 52 phase encodings per frame respectively, corresponding with reduction factors of 1, 2, 1.85, and 3.7. Figure 20 shows PINOT reconstructions (frames 1, 9, and 15) of a 16-frame short axis scan. The PINOT reduction factor is 3.76, combining SPACE-RIP reduction factor 2 and Noquist reduction factor 1.88 (50% dynamic FOV). These PINOT reconstruction results both further confirm the edge detail preservation and reduced SNR, observed in the reconstructions from computer simulated data.

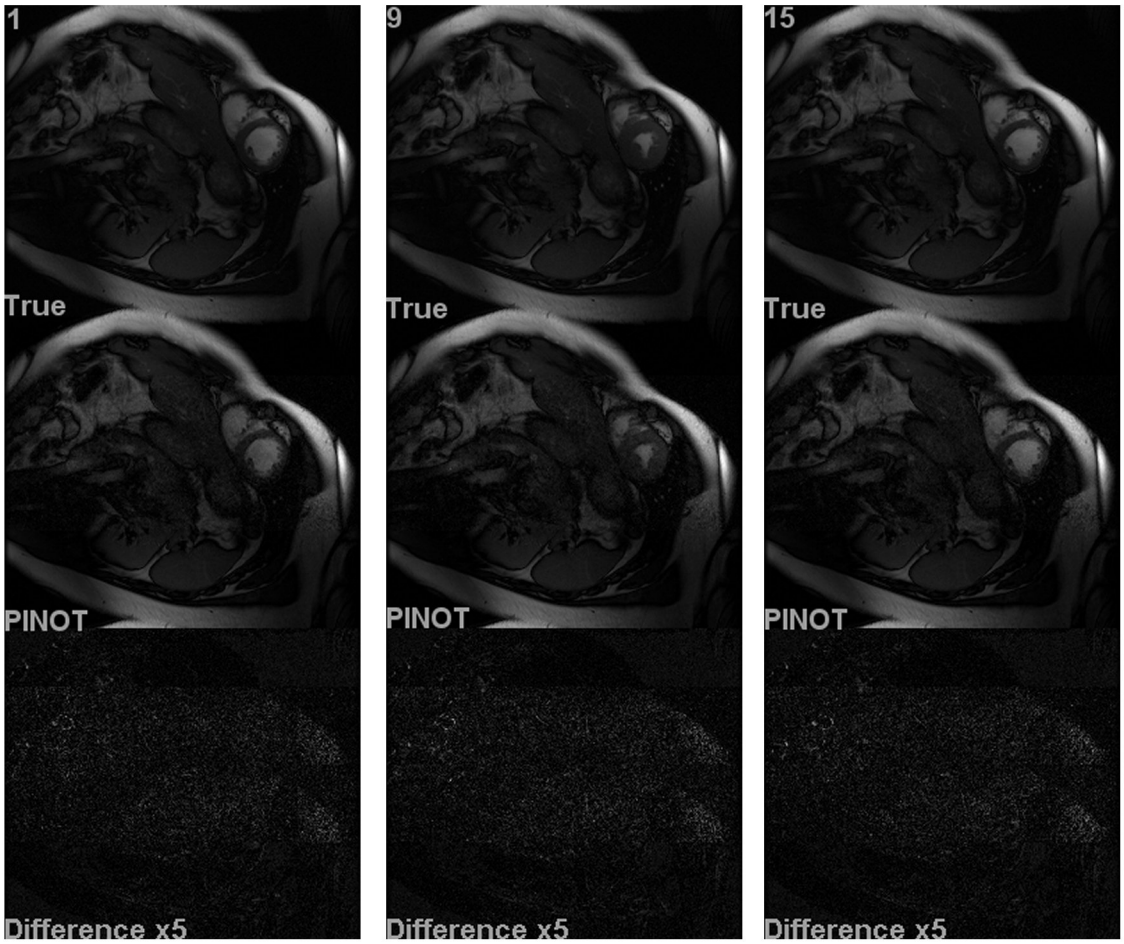

Figure 20: Conventional full-grid "true" images results (top row) for a retrospectively sub-sampled real MRI scan, compared with PINOT ($R = 3.76$) (middle row) for three different image frames (frames 1, 9, and 15 of a 16 frame series). The bottom row shows the corresponding difference images (with an intensity multiplication factor of 5).

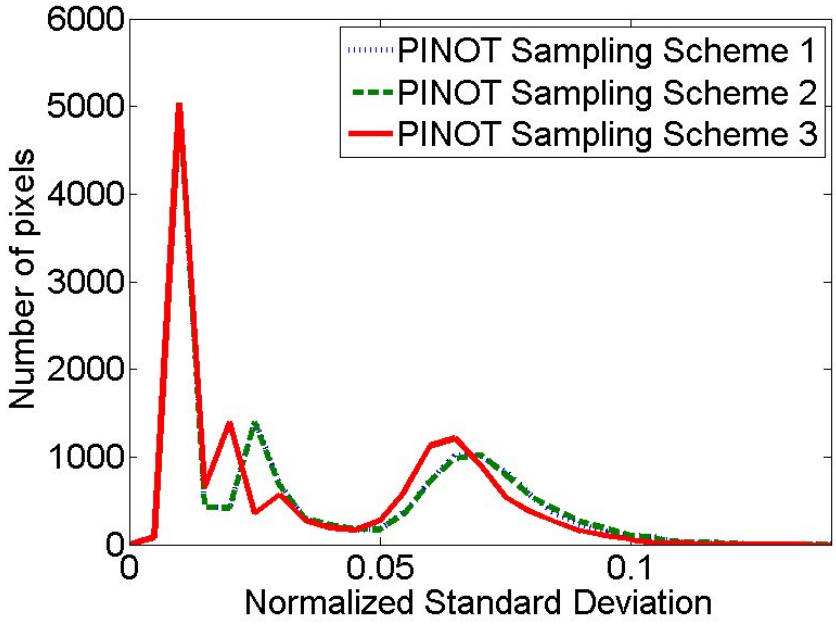

Figure 21: Normalized noise distribution for PINOT with three different sampling patterns. PINOT sampling scheme from 1 to 3 is TSENSE, *k-t* SENSE and PINOT sampling scheme respectively.

3.5.3 Experiment 3: Sampling Scheme comparison

We compared noise level of the PINOT reconstructions using the default subset sampling schemes with the TSENSE, *k-t* SENSE sampling schemes (Fig 15d e). Additionally, two criteria, condition number and sum of squared errors (SSE), were shown to demonstrate the numerical stability of PINOT encoding matrix associate with different sampling schemes. Assuming added Gaussian distributed noise and the least squared reconstruction, SSE [31, 56] of the PINOT reconstructed image is measured using $E_{(M_{PINOT})} = trace(M_{PINOT}^{H} \Psi M_{PINOT})^{-1}$. Here Ψ is the receiver noise matrix and considered as identity matrix for simplicity.

Fig. 21 shows the histogram of noise level, using all three different sampling schemes on PINOT around reduction factor 4. We found that the sampling pattern we proposed is slightly better than the other two. Table 2 shows the condition numbers from two columns shown in Fig. 22b and SSE of MPINOT with three different

		Column 49	Column 87
PINOT Sampling Scheme 1	SSE	33.9941	39.7927
	condition number	8.3487	14.8061
PINOT Sampling Scheme 2	SSE	35.6672	40.6622
	condition number	8.1122	11.7889
PINOT Sampling Scheme 3	SSE	35.6749	40.6202
	condition number	8.0523	11.3010

Table 2: Condition number and SSE (two columns) for PINOT reconstruction with three different sampling schemes.

sampling schemes. All three sampling schemes generate comparable well conditioned PINOT encoding matrix and PINOT sampling scheme has the smallest SSE.

3.5.4 Experiment 4: Comparison of PINOT with TSENSE and k-t SENSE

TSENSE combines UNFOLD ($R = 2$) with SENSE ($R = 2$) to achieve an acceleration factor of 4, relative to conventional full-grid acquisition. First, interleaved k-space sampling shifts two aliased components to the temporal band edge; the aliases are subsequently filtered using a low pass Fermi filter. Then the two remaining aliasing components in DC frequency can be separated by SENSE with two or more coils. k-t SENSE: The k-t SENSE implementation includes capturing the signal covariance of aliased components from a separate low-resolution training data set and then retrieving the true signal from aliased components.

TSENSE and k-t SENSE are implemented for comparison with PINOT with both simulated and real MRI data. To evaluate temporal fidelity, temporal plots of signal intensity along two lines were shown as well. TSENSE and k-t SENSE mean signal intensities are compared with PINOT along the spatial and temporal dimensions, noise distribution histogram of three methods are shown as well. Computational cost of different methods is also analyzed.

Figure 22a compares, in spatial domain, TSENSE, k-t SENSE, and PINOT at simulated diastole and systole for noisy computer simulated data. All three methods yielded visually acceptable image quality for acceleration factors at or close to 4.

TSENSE and k-t SENSE both displayed residual edge blurring at myocardial boundaries and image artifacts (marked by white arrows) during systolic contraction and diastolic relaxation. PINOT showed noticeably less edge artifact, however at some penalty of higher random noise level, especially in the dynamic FOV region. Mean signal intensity images and the normalized noise distribution histogram (Fig. 22c) further confirm this observation. A corresponding comparison in a short axis MRI scan is shown in Fig. 23, cropped to a region around the heart to highlight important myocardial edge details. The comparison of PINOT, TSENSE, and k-t SENSE consistently shows the same observation regarding edge resolution and SNR.

For the comparison of intensity changes over time, temporal profiles of two 1-D spatial cuts along the phase encoding axis are presented for the noisy computer simulated and short axis images, at two readout locations each, in Fig. 22b and 23d. Mean signal intensity images and the normalized noise distribution histogram are shown in Fig. 22c. The time profiles from the (cropped) short axis scan (Fig. 23d) were selected through the septal wall and the LV myocardium. In both cases these results again confirm that PINOT better captures the changes over time at sharp edges, as evidenced by the bright vertical lines (arrows) in the difference images for k-t SENSE and TSENSE at end systole, which indicate edge errors. PINOT shows a higher uniform noise level across the (x,t) difference map, whereas TSENSE and k-t SENSE results show remarkable gap of sharp signal transition along temporal frames (marked in white arrows). In Fig. 23, TSENSE shows a signal loss at the right ventricle wall, and TSENSE and k-t SENSE both have signal loss near abrupt systolic intensity changes near the endocardial edge. Comparing with TSENSE and k-t SENSE in temporal direction, PINOT has a slightly higher noise level in the dynamic FOV (Fig. 23c) but lower noise level in the static FOV.

The PINOT reconstruction computational time was measured for the phantom data set ($M_{PINOT} = 1920 \times 960$, $R = 3.75$). Direct matrix inversion for all 120

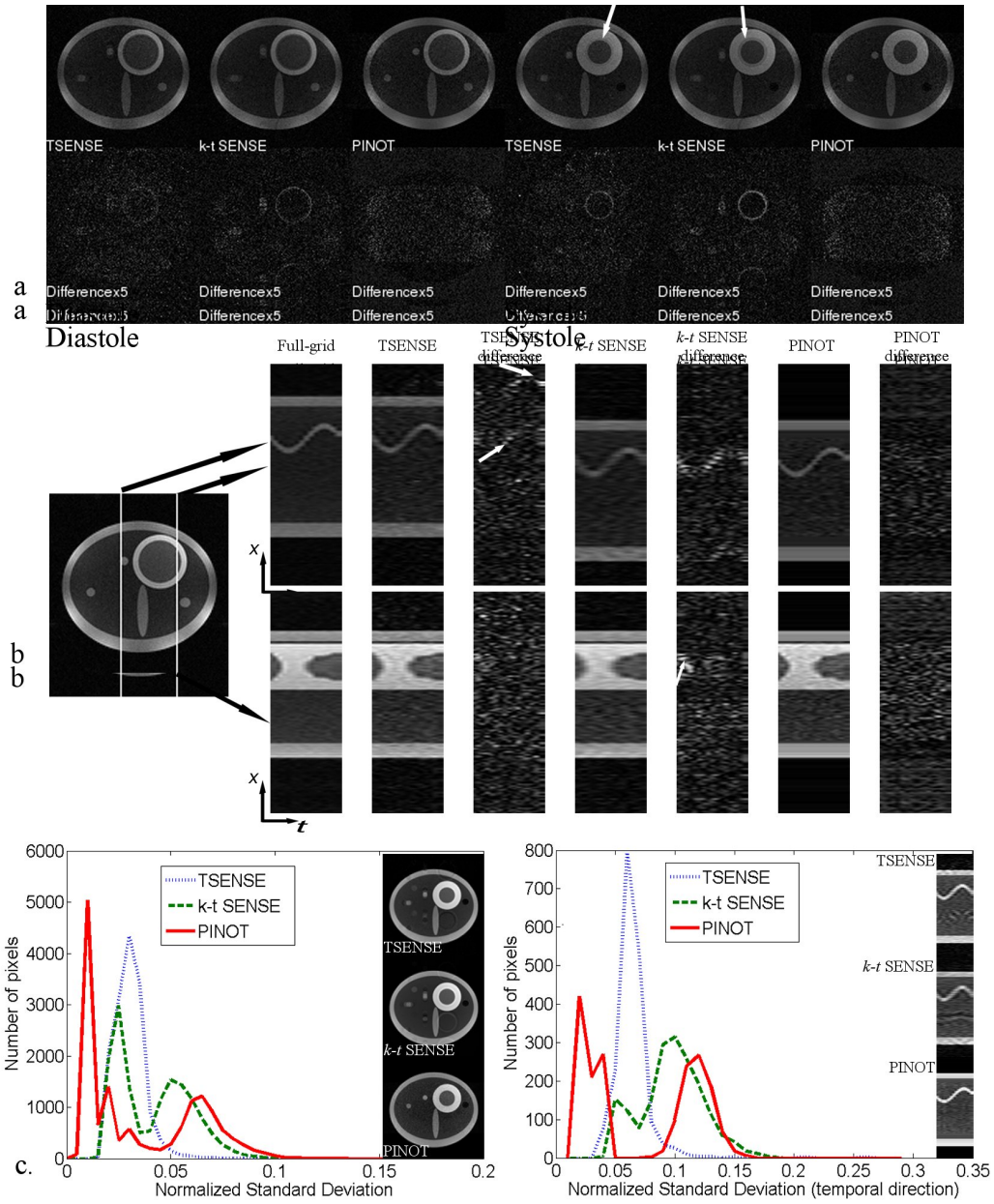

Figure 22: TSENSE, k-t SENSE, and PINOT reconstruction comparison of the diastole and systole frames from a 15 frame computer simulated data set with noise. Row a. shows TSENSE reconstruction (reduction factor = 4), k-t SENSE reconstruction (reduction factor = 4) and PINOT reconstruction with 50% dynamic FOV (reduction factor = 3.75). The absolute differences between TSENSE, k-t SENSE, and PINOT with the full-grid reconstruction are also displayed (difference images are enlarged 5 times to see the details, then all the images are shown under the same scale). b. shows the corresponding profiles in y-t space at different x. Gap of sharp signal transition and image artifacts along temporal frames are marked in white arrow. c. shows the histograms of the noise level with mean signal intensity images along spatial and temporal direction. (All images are under the same scale).

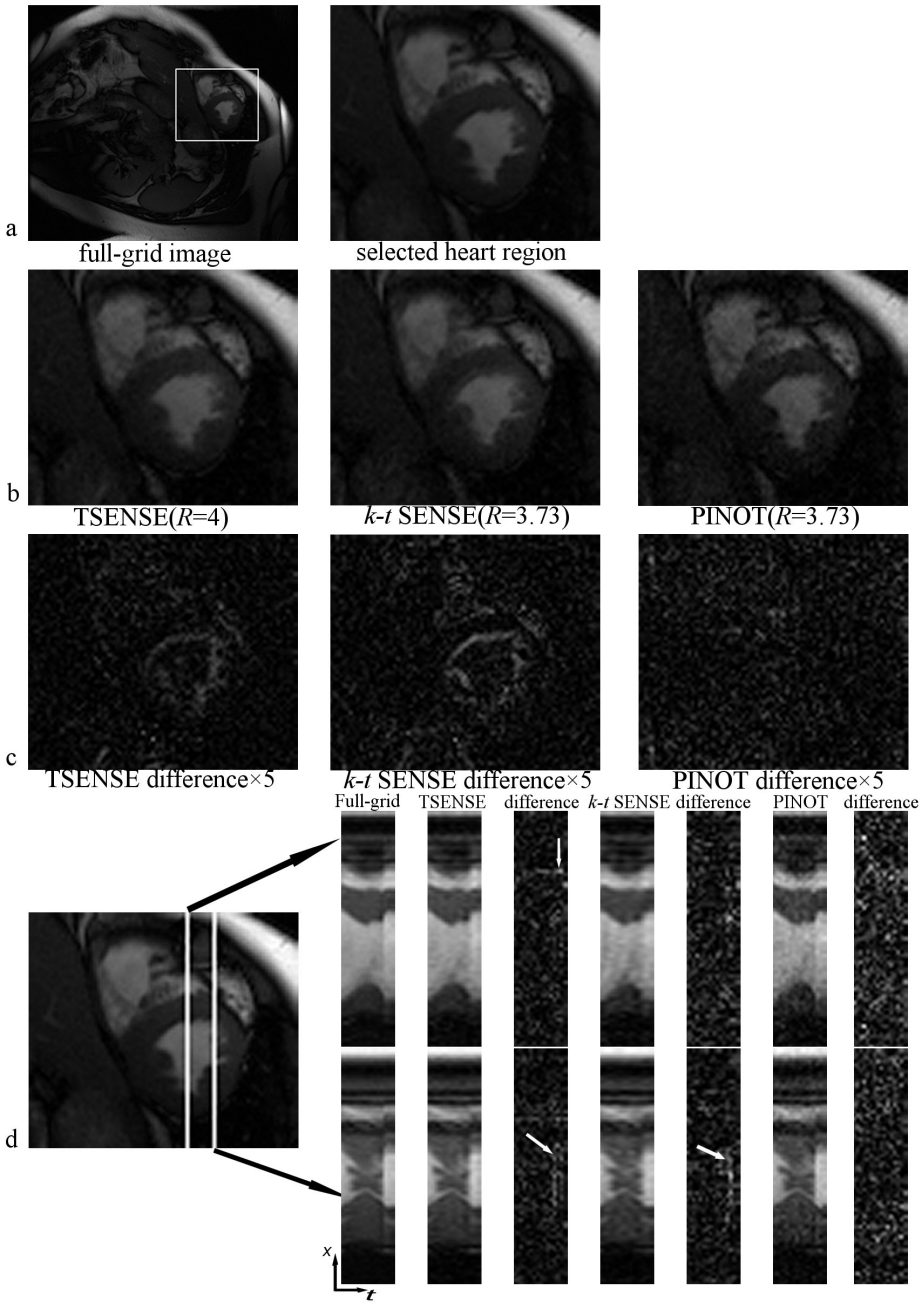

Figure 23: 13th of 16 frames in an axial data set results, comparing the selected heart region from the full-grid image and the reconstructed image from TSENSE, *k-t* SENSE, and PINOT. (a) shows full-FOV image and zoomed ROI images to reveal details in the heart. Zoomed TSENSE, *k-t* SENSE and PINOT results are shown in (b). (c) shows the corresponding difference images between selected heart region from the full-grid image and TSENSE, *k-t* SENSE, and PINOT, all amplified by the same factor (5) to compare differences. The achieved reduction factor is 4 for TSENSE, *k-t* SENSE and 3.73 for PINOT. Corresponding profiles in *y-t* space at different x were shown at the (d). Gap of sharp signal transition along temporal frames are marked in white arrow. (All images are under the same scale).

readout pixels by MATLAB on a Quad Core Xeon 2.66GHz computer with 16GB of RAM requires 58 minutes. However, this computational cost can be alleviated by using iterative CG method down to 6.38 minutes. For comparison: TSENSE reconstruction ($R = 4$) and k-t SENSE ($R = 4$) of the same data set required and 0.65 and 0.95 minute respectively.

3.5.5 Experiment 5: PINOT with regularization

In experiment five, regularized PINOT was implemented using Tikhonov regularization [41]. A low resolution reference (25% of full resolution phase encoding lines) scan is used as a prior estimate of the solution. The regularization parameter was calculated using the L-curve algorithm [24]. We compared PINOT with/without regularization under two different reduction factors 3.75 and 13.33 (75% static FOV for Noquist and $R_{np} = 4$).

As what we observe from Fig. 24a, there is no noticeable difference with/without regularization for PINOT reconstruction ($R = 3.75$). When the reduction factor is high ($R = 13.33$), noise amplification penalty of unregularized PINOT becomes a dominating factor in image quality, shown in Fig 24b, while regularized PINOT reconstruction shows a significant SNR improvement, but loses edge information. The observation is consistent with the assertion in [41] that the use of lower spatial resolution reference images as the regularization prior may results in oversmoothed reconstructed images. We conclude that PINOT with regularization may sacrifice edge detail in exchange of SNR improvement.

3.6 Discussion

Overall, PINOT has yielded stable results with a composite acceleration rate of around $3.5-4$ on both with simulated data and with a variety of MRI data sets. In all experiments where the constituent Noquist and SPACE-RIP methods yielded high-quality results, we also observed satisfactory image quality with the corresponding

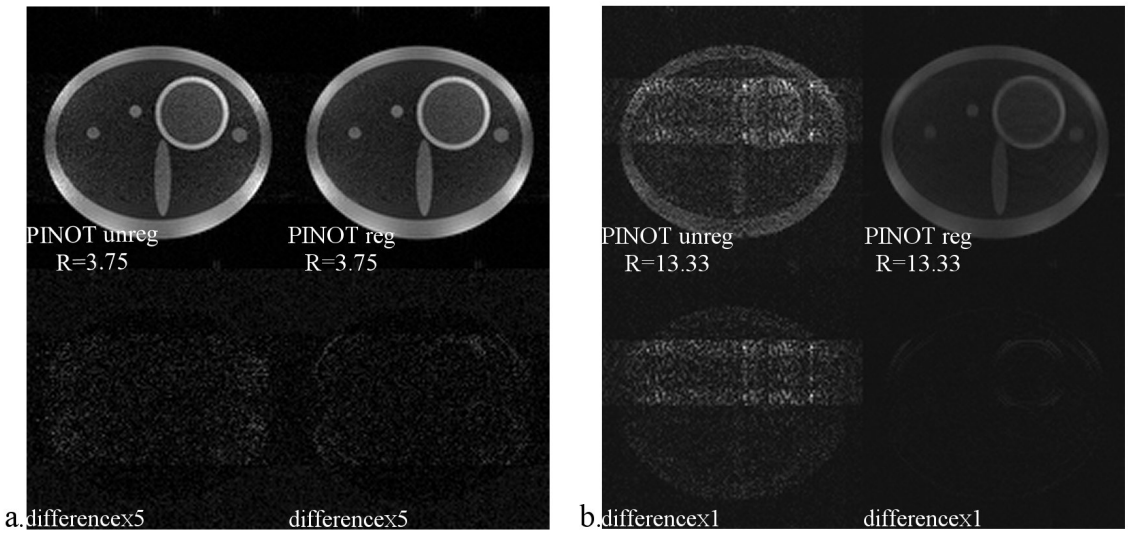

Figure 24: Unregularized and regularized computer simulated PINOT reconstruction of (a) reduction factor 3.75 and (b) reduction factor 13.33 using reference scan at 25% spatial resolution. Corresponding difference images are shown below, scaled by 5 in (a) to show details.

PINOT reconstruction. PINOT effectively achieves multiplication of the individual acceleration factors of the constituent methods, and intuitively it should come with a corresponding accumulated cost in SNR penalties in the dynamic region. A 50% static FOV for Noquist and a reduction factor of 2 for parallel imaging appear to be reasonable parameters for cine cardiac images with $4-8$ channel flexible surface coils at 1.5T, resulting in a composite acceleration rate of around 4. In such cases the PINOT encoding matrix is well conditioned and the PINOT reconstruction can be solved by iterative conjugate gradient method to alleviate the high computational cost of the direct matrix inversion. For the cases when images have implicitly low SNR, or high acceleration factor, the noise amplification penalty of PINOT may become a dominating factor in image quality. Regularization must be applied to improve the SNR, but may lose edge details and have increased computational burden. Like all other parallel imaging methods, PINOT reconstruction quality depends on the estimate accuracy of the sensitivity maps.

Compared with TSENSE and *k-t* SENSE at similar sampling rates, PINOT has

better edge preservation and higher temporal resolution, but with higher random noise level in dynamic regions. An explanation for these may be the fact that as a combination of Noquist and SPACE-RIP, PINOT does not apply any filter or implicit regularization. In clinical analysis of cardiac function, accurate detection of myocardial boundary locations is critically important. From this perspective PINOT has a spatial-temporal resolution advantage, but this must be weighed against the SNR penalty.

In most reconstructions in this study, we simply extended the Noquist sampling pattern with the straightforward even-spaced subsampling commonly used parallel imaging. The corresponding Matrix M_{PINOT} is well conditioned with reduction factors around 4. Our experiments also showed the possibilities of using TSENSE or k-t SENSE sampling patterns, but with slightly higher noise level results.

3.7 Summary

The "PINOT" method integrates SPACE-RIP parallel imaging with Noquist rFOV to accelerate cine imaging with an acceleration factor equal to the product of the individual factors feasible for each method. As illustrated by computer simulated and real MRI data experiments, PINOT can be successfully applied to the reconstruction of undersampled MR images while preserving full spatial-temporal resolution, retaining edge information better than comparable methods like TSENSE and k-t SENSE around reduction factor 4. However, the PINOT algorithm adds to the computational burden of the image reconstruction, and cost in accumulated SNR penalty in dynamic regions which can be alleviated by regularization but may sacrifice resolution. If an SNR trade-off can be afforded, PINOT may be the method of choice for accelerated acquisition with full preservation of sharp edge details. For imaging systems with limited SNR, TSENSE and k-t SENSE may be more suitable methods. Continued research must focus on improving PINOT reconstruction SNR performance with

higher reduction factor but not lose spatial or temporal resolution.

CHAPTER IV

PINOT IMPROVEMENTS/EXTENSIONS

4.1 Introduction

Chapter 3 introduced the PINOT theory and experiments showed that PINOT favorably preserves the spatio-temporal resolution of reconstructed images but at costs of a higher computational cost and higher noise level in the dynamic region of the reconstructed images. Instead of the pre-calculated sensitivity maps previously used for PINOT, we present an auto-calibrated variant of PINOT [21], offering PINOT an alternative way to calculate sensitivity maps.

Conjugate-gradient (CG) method [55] had been applied for alleviating the high computational cost for the PINOT reconstruction in Chapter 3. In this chapter, we propose an additional significant time savings, achieved by providing a favorable initial estimate based on PINOT matrix's structure, called CG-initialized PINOT (CGi-PINOT) [20].

This chapter is organized as following: section 4.2 introduces the importance of accurate coil sensitivities and particular challenge of sensitivity maps estimations for cardiac applications. It first gives an overview of the common sensitivity map estimation methods and their advantage and disadvantages, followed by an auto-calibrated variant of PINOT we present. Section 4.3 presents CGiPINOT for a speed up gain of PINOT reconstrution. Future directions are given in discussion.

4.2 Improving Sensitivity map Estimation

Parallel imaging, the use of multiple coils to accelerate MRI scan time, is a very hot research topic. Parallel imaging methods include SMASH, SENSE, SPACE-RIP,

GRAPPA, TSENSE, k-t SENSE and PINOT. All of these schemes at least partially use information from multiple coils to reconstruct the unaliased images from reduced sampled data. Unfortunately they face problems with image degradation (e.g. SNR loss or image artifacts) especially when the acceleration factor is high. As discussed in chapter 2, one major source of errors which deteriorates reconstruction quality is sensitivity map inaccuracy. The challenge of obtaining accurate sensitivity maps is very important for any reduced-data imaging method involving parallel imaging (PI) reconstruction, particularly those PI methods requiring explicit sensitivity maps. Another challenge in calculating sensitivity maps, especially in cardiac imaging applications, is the fact that there are large areas near the heart(for example, lung) which contribute little or no MR signals, resulting in high noise levels in the corresponding regions of sensitivity maps. In general, poor estimates of sensitivity maps will result in image artifacts while good estimates of sensitivity maps could allow for further increases in the reduction rate and still maintain good reconstructions.

4.2.1 Technical Overview of current sensitivity maps calculation

In parallel MRI, accurate coil sensitivity estimates are required to reconstruct aliasing free images. Raw sensitivity maps are typically calculated using each component coil images divided by the additional body coil image or the sum of square image. Sensitivity maps vary from the coil loading, the most commonly used approach uses low resolution images from each component coil acquired by reference scans before or after accelerated data acquisition. However this method prolongs the preparatory scan time and can introduce reconstruction artifacts due to spatial inconsistency between the reference scan and the accelerated scan. Another common way to calculate sensitivity maps is to use auto-calibrated methods [12] like GRAPPA [14] to estimate missing k-space lines for each coil and reconstruct a sum of squares images. These methods require additional auto calibrated signal lines in the image acquisition and

therefore avoid the misregisteration problem from reference scan.

These raw sensitivity maps are usually further refined using conventional methods involving smoothing or extrapolation algorithms. They are based on the assumption that coil sensitivities are smooth functions. A polynomial model [54] was used in the original SENSE paper and other basis function such as thin-plate splines or wavelets [40] are also used to improve coil sensitivity homogeneities. Feng Huang et al [29] exploit further improvement of sensitivity maps using inpainting technique, to estimate the sensitivities more accurately. It fills in damaged or missing regions of an image with the use of information from surrounding areas. Sheng et al. [70] and Uecker et al. [64] both used joint estimation of the image and the sensitivity maps, iteratively updating sensitivity maps, for brain images reconstructions. In the following, our proposed GRAPPA enhanced sensitivity maps is introduced for PINOT. Experiments in cardiac MR image are shown in section 4.4.

4.2.2 Auto-calibrated PINOT

We have previously [19, 18] used pre-scan calculated sensitivity maps for PINOT. Although commonly used and easy to implement, this method prolongs the preparatory scan time and can introduce reconstruction artifacts due to spatial inconsistency between the pre-scan and the acquisition data. Auto-calibrated methods like GRAPPA estimate missing k-space lines for each coil and reconstruct a sum of squares images. As demonstrated in GEYSER [26], acquiring autocalibration signals (ACS) simultaneously with the real scan and estimating missing data, GRAPPA can be used to calculate more accurate sensitivity maps for SENSE-like parallel imaging techniques. Based on this idea, we present an auto-calibrated variant of PINOT which uses GRAPPA to estimate coil sensitivity maps. These methods avoid the misregisteration problem but have additional computational cost for SENSE-like parallel imaging methods which requires explicit sensitivity map information.

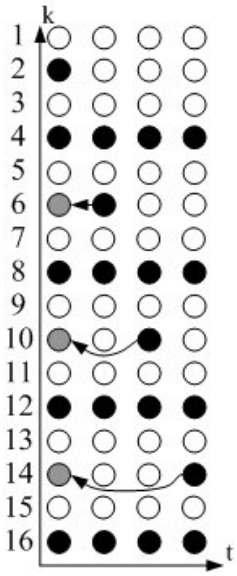

Figure 25: Sampling scheme (16 phase-encodings and 4 frames) for PINOT. Black dots represent sampled k-space lines. Horizontal axis: time, vertical axis: phase encoding direction. The reduction factor for this figure is 3.2. For the first time frame, all black sampling dots and the gray sampling dots are combined together to form k-space data for GRAPPA to estimate sensitivity maps. This procedure repeats for all frames.

The sampling scheme for PINOT with SENSE reduction factor 2 and 50% dynamic FOV is shown in Fig. 25. PINOT samples every fourth k-space line for each time frame with additional sheared-grid sampling spread across time frames. To estimate a sensitivity map for each time frame, all sheared-grid samples are replicated across all time frames. With additional low-frequency ACS lines, this forms a k-space encoded data set, used to create a GRAPPA reconstruction with reduction factor 2 to calculate the sensitivity maps. After that, the estimated coil sensitivities are used in PINOT reconstruction. The reconstruction schemes of auto-calibrated PINOT and pre-scan PINOT are compared in Fig. 26.

4.3 The PINOT Reconstruction Speed Improvement

As introduced in section 3.2, constrained by spatiotemporal and coil sensitivity priors, PINOT reconstructs the image f from reduced data F by direct-inversion of the

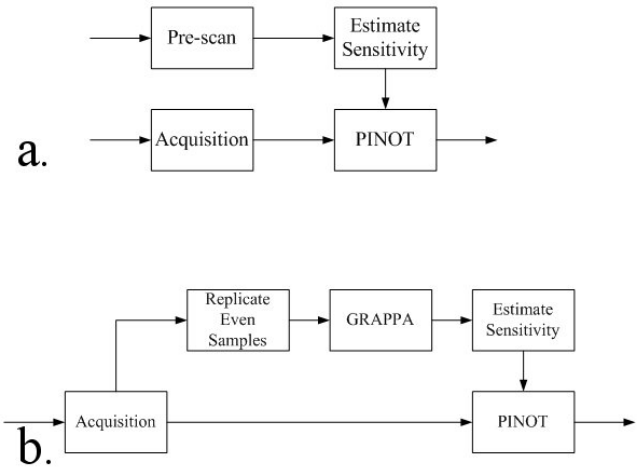

Figure 26: Coil sensitivity estimation scheme for: (a) pre-scan PINOT and (b) auto-calibrated PINOT.

forward model $F = M_{PINOT} f$. A solution for alleviating the high computational cost of this direct matrix inversion is the use of iterative algorithms, such as the conjugate gradient method [55]. Axelsson et al [51] explained the rate of conjugate gradient method's convergence and concluded that the CG method converges typically in three phases, an initial phase of rapid convergence but short duration, which depends essentially only on the initial error. The initial estimate for CG is often chosen as $f_0 = 0$. To improve the convergence speed, we take advantage of special structure of sparse matrix M_{PINOT} to calculate a fast initial estimate f_0 close to the solution f. The method is called CG-initialized PINOT (CGi-PINOT).

First, we simplify Eq. 3.4 to Eq. 4.1,

$$\boldsymbol{M}_{PINOT} = \begin{bmatrix} \boldsymbol{P}_1^{N_P \times N_S} & \boldsymbol{D}_1^{N_P \times N_D} & 0 & ... & 0 \\ \boldsymbol{P}_2^{N_P \times N_S} & 0 & \boldsymbol{D}_2^{N_P \times N_D} & ... & 0 \\ \vdots & \vdots & \vdots & \vdots & \vdots \\ \boldsymbol{P}_T^{N_P \times N_S} & 0 & 0 & ... & D_T^{N_P \times N_D} \end{bmatrix}, \tag{4.1}$$

where $N_P = N_c N_{sample\_PI}$. Submatrices of $\boldsymbol{M}_{PINOT}$ are $\boldsymbol{P}_t$ and $\boldsymbol{D}_t$ with sizes $N_P \times N_S$ and $N_P \times N_D$ respectively. Appendix A derives the approximate of the pseudo-inverse

of M_{PINOT} as Eq. 4.2

$$M_{PINOT}^{\dagger} = \begin{bmatrix} \boldsymbol{X}_1^{N_S \times N_P} & \boldsymbol{X}_2^{N_S \times N_P} & ... & \boldsymbol{X}_T^{N_S \times N_P} \\ \boldsymbol{Y}_1^{N_D \times N_P} & 0 & ... & 0 \\ 0 & \boldsymbol{Y}_2^{N_D \times N_P} & ... & 0 \\ \vdots & \vdots & \ddots & \vdots \\ 0 & 0 & ... & \boldsymbol{Y}_T^{N_D \times N_P} \end{bmatrix} \tag{4.2}$$

The principle behind it is to utilize the block structure of M_{PINOT} and this pseudo-inverse, we are able to separate the problem by frame index t and then deconstruct the problem into a series of pseudo-inversions for each frame as shown in Eq. 4.3.

$$\begin{bmatrix} T\boldsymbol{X}_t \\ \boldsymbol{Y}_t \end{bmatrix} \begin{bmatrix} \boldsymbol{P}_t & \boldsymbol{D}_t \end{bmatrix} = \begin{bmatrix} \boldsymbol{I} & 0 \\ 0 & \boldsymbol{I} \end{bmatrix} \tag{4.3}$$

Each of these inversions can be solved at very low computational cost. We have estimates of $\boldsymbol{X}_t$, $\boldsymbol{Y}_t$ for frame t. They are submatrices components to form M_{PINOT} in Eq. 4.2. A quick estimate (Eq. 4.4) is then applied to solve CG PINOT with faster convergence.

$$f_0 = M_{PINOT}^{\dagger} F \tag{4.4}$$

4.4 Experiments

Experiment 1: Auto-calibrated PINOT

In GRAPPA-enhanced autocalibrated PINOT reconstruction experiment, full-grid, pre-scan, GRAPPA enhanced PINOT reconstructions are compared. SENSE reduction factor 2 and Noquist 50% dynamic FOV was used, resulting in 60 phase encoding lines/frame acquired for PINOT reconstruction (reduction factor 3.73). Additional 32 k-space lines were used to estimate sensitivity maps for pre-scan, auto-calibrated and GRAPPA enhanced PINOT, resulted in the net reduction factors equal to 2.8.

Experiment 2: PINOT reconstruction with a fast initial estimate

Experiment two compared CGi-PINOT (initial estimate is calculated from Eq. 4.4, CG-PINOT (initial estimate set to be 0) and direct matrix inversion PINOT together in terms of the reconstruction time, convergence speed and number of iterations, on both simulated and in vivo studies. The number of iterations and tolerance were chosen to achieve comparable image quality to direct inversion PINOT.

4.5 Results

4.5.1 Experiment 1: PINOT sensitivity maps improvement

Fig. 27 b-c shows PINOT results with sensitivity maps calculated only using 32 k-space lines from prescan and acquisition stage respectively. This clearly results in Gibbs ringing. Using GRAPPA estimated the missing k-spaces with 32 ACS lines and has better sensitivity maps, so GRAPPA enhanced auto-calibrated PINOT achieves better SNR and fewer artifacts (Fig. 27d). A comparable quality PINOT reconstructed image for a pre-scan PINOT with the same reduction factor 3.8, shown in Fig. 27e, requires 112 k-space lines (half of full phase encoding lines) to estimate sensitivity maps, compared with 32 phase encoding lines for GRAPPA enhanced PINOT reconstruction.

The results show significant advantages of auto-calibrated PINOT with GRAPPA-enhanced sensitivity maps over PINOT with pre-scan or simple autocalibrated sensitivity maps. The GRAPPA-enhanced auto-calibration method resulted in higher SNR and less artifacts, allowing a substantial reduction of the total number of k-space lines needed by PINOT to generate the sensitivity maps required to reconstruct high-quality images.

4.5.2 Experiment 2: PINOT reconstruction with a fast initial estimate

The computer simulated complex data set has a reduction factor $R = 3.75$, combining SPACE-RIP reduction factor $R_p = 2$ and Noquist reduction factor $R_{nq} = 1.88$ (50% dynamic FOV). It takes about 10s to calculate f_0 for the phantom data, which

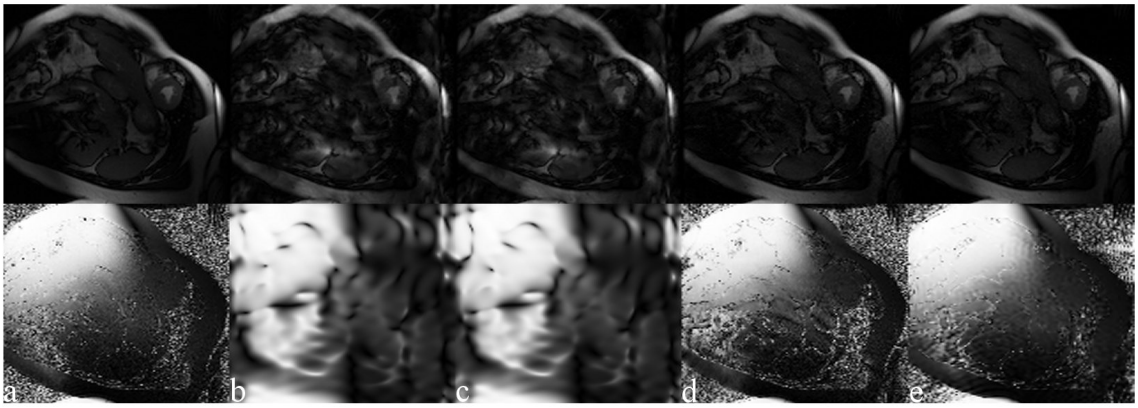

Figure 27: Systolic frame (7 of 16) of a short axis movie: (a) Full-grid reconstruction and coil sensitivity maps calculated with all k-space lines, (b) PINOT using pre-scan to compute sensitivity maps, (c)Auto-calibrated PINOT with self-referenced coil sensitivity maps, (d)GRAPPA enhanced PINOT scan calculated coil maps, and (e) PINOT using pre-scan to compute sensitivity maps. Additional 32 phase encoding lines are used in (b)-(d) and 112 phase encoding lines are used in (e) for calculating sensitivity maps. Corresponding sensitivity maps are shown below the reconstructions. All reconstructions and sensitivity maps are displayed under same scale.

is negligible compared to the full reconstruction time. Table 3 shows for the same image qualities, CG/CGi-PINOT are much faster than the direct inversion PINOT, while CGi-PINOT converges faster than uninitialized CG-PINOT. Fig. 28 shows a comparison of CG-PINOT and CGi-PINOT after 10 iterations for phantom data. CGi-PINOT almost converges while CG-PINOT still has artifacts. The initial estimate f_0 (Fig. 28b) reconstructs quickly but has significant noise. Since this is not the least-squares solution, we lose some noise resistance relative to solving the full matrix. This result is too noisy to use as the final reconstruction, but provides a good initial estimate f_0, and allows the CG-PINOT to be solved with fewer iterations.

The short axis cine MRI data has R equals to 3.76 with $R_p = 2$ and $R_{nq} = 1.88$. Cine MRI reconstruction (Fig. 29) shows similar characteristics but CGi-PINOT converges at 30 iterations, while CG-PINOT converges at 40 iterations. We also tested CG-PINOT and CGi-PINOT running until the CG method has fully converged, typically 200 iterations, which take about 152.34 minutes, still 10 times faster than

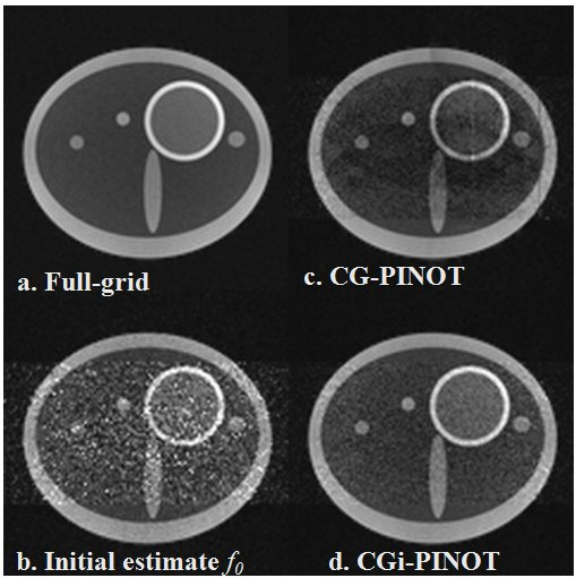

Figure 28: displays the 1st frame of the phantom images, showing the full-grid reconstruction (a), initial estimate f0 (b), CG-PINOT (c) and CGi-PINOT (d) at 10 iterations.

direct inversion PINOT. The results (Fig 29g) were equal for CG-PINOT and CGi-PINOT and have slightly lower RMS errors than the images shown in Fig. 29.

Both simulated and in vivo studies show that CGi-PINOT with initial estimate f_0 converges faster and provides excellent reconstructed image quality with less time. This is due to the initial convergence phase of CG method. Furthermore, as temporal frames and/or the image size increase, the size of M_{PINOT} will increase proportionally, causing the calculation time advantage of CGi-PINOT to increase dramatically. However as the number of iterations increases beyond the initial convergence phase, the convergence rate no longer depends heavily on initial error, and the speed advantage of CGi-PINOT disappears. The results then have higher accuracy than direct inversion because the CG method is more resistant to numerical precision problems. Even at complete convergence, CGi-PINOT requires a full order of magnitude less computation time than direct inversion.

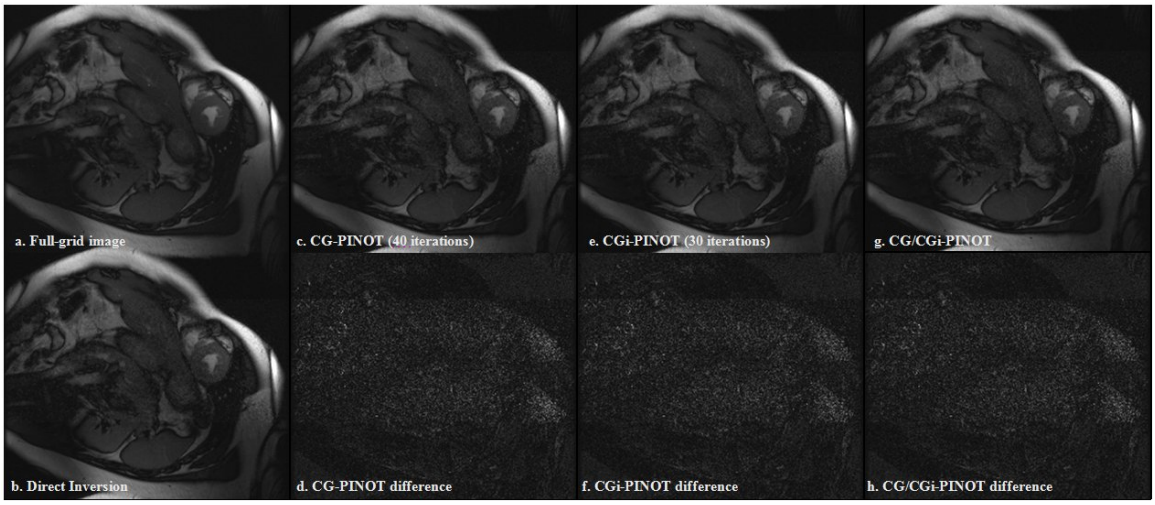

Figure 29: 8^{th} frame of full-grid images (a) for a cine MRI, with direct inversion PINOT (b), CG-PINOT (c) and CGi-PINOT (e) at 40 and 30 iterations respectively. The fully converged CG/CGi-PINOT are shown in (g). The bottom row (d), (f) and (h) shows the corresponding difference images (intensity enlarged 5 times to show details) from the corresponding top. All images are under the same scale.

	Phantom		Cine MRI	
	Time	Iteration	Time	Iteration
Direct Inversion	58.01	N/A	1595.5	N/A
CG-PINOT	6.38	20	70.35	40
CGi-PINOT	4.57	15	67.23	30

Table 3: Time (min) and iteration numbers needed for direct inversion PINOT, CG-PINOT and CGi-PINOT.

4.6 Discussion

The nonlinear joint estimation method showed successful sensitivity map estimation in brain MRI. Image inpainting has been used in restoration of old paintings by museum artists, and removing scratches from photographs. It fills in damaged or missing regions of an image with the use of information from surrounding areas. In its essence, it is very similar to image interpolation and is reported by Feng Huang et. al that it may be promising for improving sensitivity maps. Future work could focus on to exploiting improvement of sensitivity maps using inpainting techniques to initially estimate the sensitivity maps and then apply a joint estimation technique to further improve the maps' quality.

CGiPINOT, using special sparse-matrix data structures to increase the reconstruction speed, is presented. Further savings in computation time may be realized by more extensive use of parallel computing, for example using recently popularized GPU processing methods [60, 17].

4.7 Summary

Two improvements for the PINOT method are presented in this chapter. Using autocalibrated signals to calculated sensitivity maps for PINOT application is proposed, offering PINOT, other than pre-scan, an alternative way to calculate sensitivity maps. Alleviating the high computational cost of PINOT reconstruction, Conjugate Gradient PINOT with a fast initial estimate is presented and speeds up the reconstruction speed for PINOT.

CHAPTER V

PAPOULIS-GERCHBERG CONSTRAINED RECONSTRUCTION

5.1 Introduction

Papoulis-Gerchberg (PG) [11, 53] method has been applied to image restoration applications such as super-resolution (SR) and inpainting. By transforming between the image and its transform domains, the algorithm reduces error energy (i.e., the sum of squared differences from truth in either domain) in each step iteratively. We apply this idea into the rFOV reduced-data imaging method and reconstructed MR images iteratively. In the first half of this chapter, we introduce a Gerchberg Reduced Iterative System (GRIS), implemented with the Gerchberg-Papoulis (GP) algorithm, which allows flexible incorporation of multiple constraints. Under the GRIS, utilizing a temporal band-limitation constraint in the image reconstruction, a variant of Noquist (rFOV method) called iterative Noquist (iNoquist) [36], is proposed. The second half of the chapter investigates extensions of iNoquist applications. Utilizing different source of prior information, a first combination of iNoquist and Partial Fourier technique (phase-constrained iNoquist) and further combining with parallel imaging (PINOT-GRIS) are presented to achieve additional acceleration gains.

5.2 Gerchberg Reduced Iterative System (GRIS)

Papoulis-Gerchberg (PG) algorithm, one special form of Projection Onto Convex Sets (POCS) method, has been extensively applied to spectral estimation and image restoration. It solves the missing data problem in band-limited signals. The

Papoulis-Gerchberg algorithm is relative simple and can work by successive reduction of error energy. It is generally performed via the transformation between the time and frequency domains iteratively while imposing the requirements that the signal is band-limited and to match the known portion of the signal.

If we define a signal $d \in L(R)^2$, and the Fourier transform D of the given a signal $d(t)$ is:

$$D(\omega) = \int_{-\infty}^{\infty} d(t) e^{-jwt} dt. \tag{5.1}$$

Where dt is said to be band-limited if

$$D(\omega) = 0, \quad for\, |\omega| > \sigma. \tag{5.2}$$

The algorithm starts with a finite segment of the signal $d_0(t) = P_T d(t)$, where

$$P_T(t) = \begin{cases} 1, & t \in [-T,\ T] \\ 0, & t \notin [-T,\ T] \end{cases} \tag{5.3}$$

Use the Fourier Transform (F) of the filtered signal and set to zero outside interval of the passband P_σ, where

$$P_\sigma(\omega) = \begin{cases} 1, & \omega \in [-\sigma,\ \sigma] \\ 0, & \omega \notin [-\sigma,\ \sigma] \end{cases} \tag{5.4}$$

Perform the Inverse Fourier Transform (F^{-1}) of the clipped signal. Impose the known portion of the observed signal, $d(t)$, to the processed signal:

$$d_{k+1}(t) = P_T(t) + (1 - P_T) F^{-1} P_\sigma F d_k(t) \quad k = 0, 1, 2 \cdots \tag{5.5}$$

Repeat the above equation until desired convergence. The convergence $\|d_k - d\|_{L^2} \to 0$ has been proven by Papoulis, which means the band-limited signal $d(t)$ can be recovered from its segment $d_0(t)$.

5.3 Iterative Noquist (iNoquist) Algorithm

Noquist [3], proposed by Brummer et al., exploits data redundancy associated with the presence of static FOV regions in a dynamic MR image sequence to accelerate

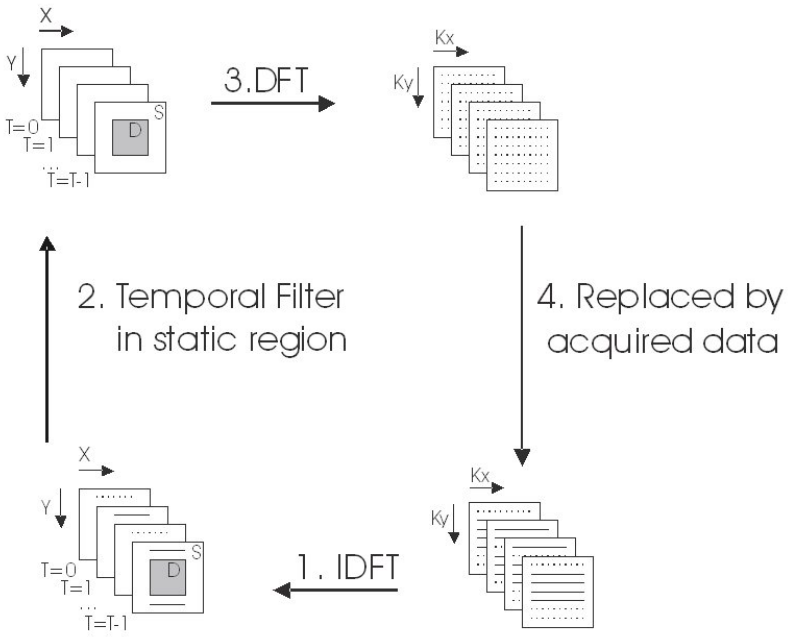

Figure 30: Reconstruction steps for iNoquist image reconstruction.

imaging speed. Noquist reconstructs the static region of an image series only once through direct matrix inversion (see details in chapter 3). Here we propose an iterative version of Noquist under Gerchberg reduced error energy system. Unlike original Noquist, iNoquist iteratively applies static (or temporally band-limited in Fourier domain) FOV region constraints in the spatial-temporal domain by regionally selective temporal filtering, and forces the resulting k-space data to be consistent with all acquired views by replacing corresponding lines with acquired data. Figure 30 shows the reconstruction steps for the iNoquist method.

Not only can iNoquist be used as an accelerated imaging method by itself but also can be applied as a post processing method to parallel imaging methods [23]. Combining parallel imaging and iNoquist sequentially may further improve suppression of aliasing artifacts. The implemental details is as follows: reduced-sampled k-space data by SPACE-RIP are reconstructed initially, iNoquist begins the first iteration reconstruction using SPACE-RIP estimated results, iteratively applies temporal band-limitation constraints for (nearly) static regions in the image sequence to

improve the estimation of the k-space data omitted during acquisition.

5.4 Recent Developments of Partial Fourier Methods

A brief review of Partial Fourier technique and an example of PF technique implemented with POCS were introduced in chapter 2. Recent works have combined both parallel imaging and Partial Fourier techniques. Bydder et al [4] and Willig-Onwuachi et al [68] presented combining PF with parallel imaging by constraining parallel imaging reconstruction to get a real image. In addition, POCSENSE [58], which uses the POCS formalism to reconstruct images using the parallel imaging technique SENSE followed by PF reconstruction. Other works integrated parallel imaging methods with rFOV methods, examples are k-t SENSE [62], TSENSE [35], and PINOT [19]. Combined methods have further acceleration gain. Theoretically, partial Fourier, parallel imaging and rFOV method utilize three different sources of data redundancy and are possible to be exploited jointly for compounded gains in imaging speed or better image quality. However, PF techniques have not been combined with either rFOV methods or both parallel imaging and rFOV methods. In the next section, we introduce two algorithms, each combining iNoquist with partial Fourier method or partial Fourier and parallel imaging methods.

5.5 Algorithms

5.5.1 Phase-constrained iNoquist

Like iNoquist iteratively applying band-limited constraints to static FOV under GRIS, Similarly partial Fourier techniques, implemented with POCS algorithm, force images to comply with phase constraints in the image domain, and k-space data to comply with acquisition in the k-space domain. Therefore the combination of both methods can be naturally formed under the POCS formalism. Here, we propose a phase-constrained iNoquist method combining iNoquist and POCS Partial Fourier to further accelerate imaging. Following the definition in section 5.2, we define k-space MR

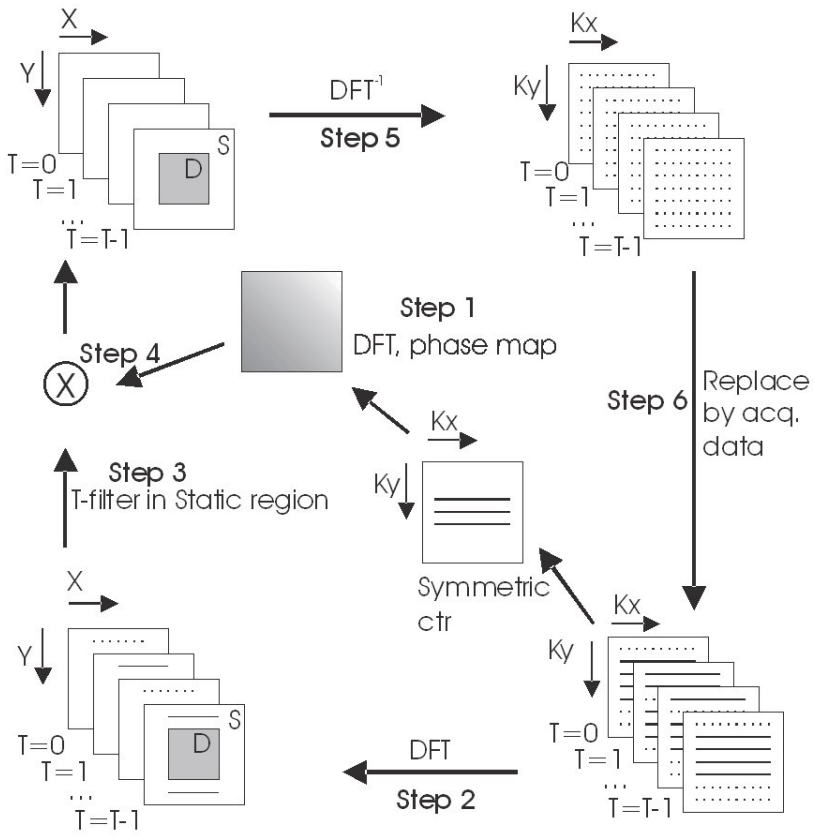

Figure 31: Reconstruction steps for phase constrained iNoquist image reconstruction.

signal $D(k,t)$, image space signal $d(x,t)$ and sampled k-space data $D_{sampled}(k,t)$. The reconstruction procedure, shown in Fig 31, is as follows:

1. Symmetric low frequency k-space views are used to calculate phase constraints $\varphi(x,t)$.

2. Zero-fill missing k-space data and apply inverse Fourier Transform to get initial estimated images $d(x,t)$.

3. In each iteration, apply a temporal low-pass filter in static regions along temporal direction to enforce temporal band-limitation constraints in the image domain.

4. Constrain the phase of resulting image to $\varphi(x,t)$ by multiplying the absolute value of the current estimate with $\varphi(x,t)$.

5. Apply a FT to get estimated fully-sampled k-space for each image and replace each acquired view by the original sampled data.

6. Apply inverse Fourier Transform and go back to step 3 until convergence or maximum number of iteration reaches.

5.5.2 PINOT with Paritial Fourier Reconstruction (PINOT-GRIS)

In this section, we propose an approach named PINOT-GRIS (PINOT by Gerchberg-Reduced Iterative System) to incorporate multiple constraints from three separate methods, PINOT (SPACE-RIP parallel imaging and Noquist rFOV) and a partial Fourier method, together to accelerate imaging speed under Gerchberg's reduce energy system. Fig. 32 is a flow chart displaying how PINOT is iteratively combined with the partial Fourier method. The k-space sampling pattern is a straightforward combination of typical sampling patterns for PF and PINOT. Fig. 33d shows PINOT-GRIS sampling pattern with 24 phase encodings and 4 time points. Acquired data are shown in black dots, and omitted k-space views in white and gray. The upper half-plane of k-space is sampled following the PINOT scheme for each time point, augmented by a symmetric fully-sampled central k-space region, used commonly in

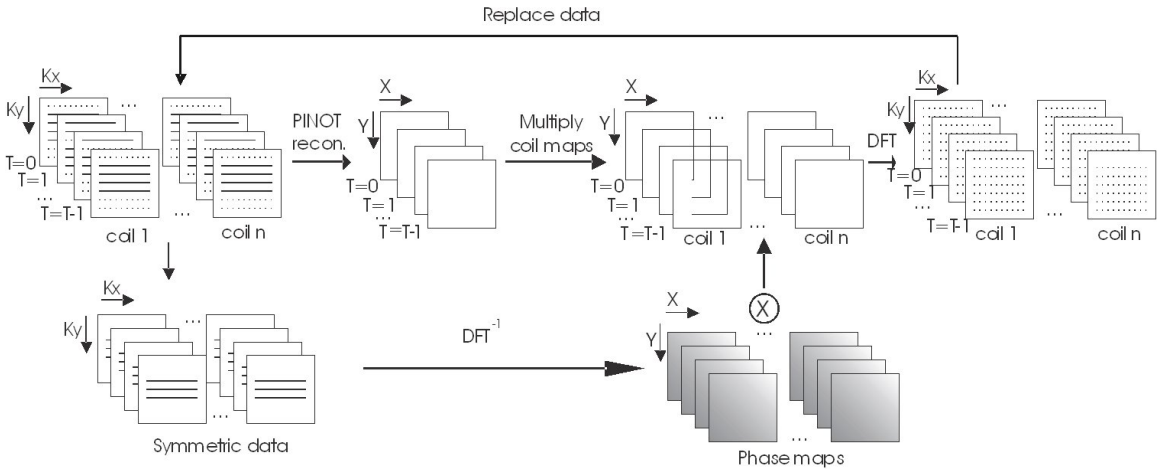

Figure 32: PINOT-GRIS reconstruction flow chart.

PF imaging to estimate image phase maps.

The proposed method starts with PINOT reconstruction of only the (incomplete) acquired k-t space data (black dots in Fig. 33d). The resulting images, which contain artifacts due to the less well-determined pseudo-inversion, are then multiplied by the coil sensitivity maps, and each time point is phase-constrained by multiplying their absolute value with the phase maps estimated from the central k-t space samples. Fourier Transform yields a current estimate of the complete k-t space data, where unsampled k-t spaces (gray dots in Fig. 33d) are selected, together with original undersampled k-t space data (black dots in Fig. 33d), to form a complete PINOT sampling scheme for the next iteration. This process repeats until convergence. Each update to the data grid reduces the "error energy" (i.e., the sum of squared differences from truth in either domain) and improves the reconstruction accuracy.

5.6 Sampling Scheme Design

The sampling schemes of three proposed methods are illustrated (for an example with 24 phase-encodings and 4 temporal frames) in Fig. 33. Black dots represented sampled k-space data; white dots and gray dots are skipped k-space data. Noquist employs a "stairwell" sampling pattern [3, 49] acquiring even k-space lines in every

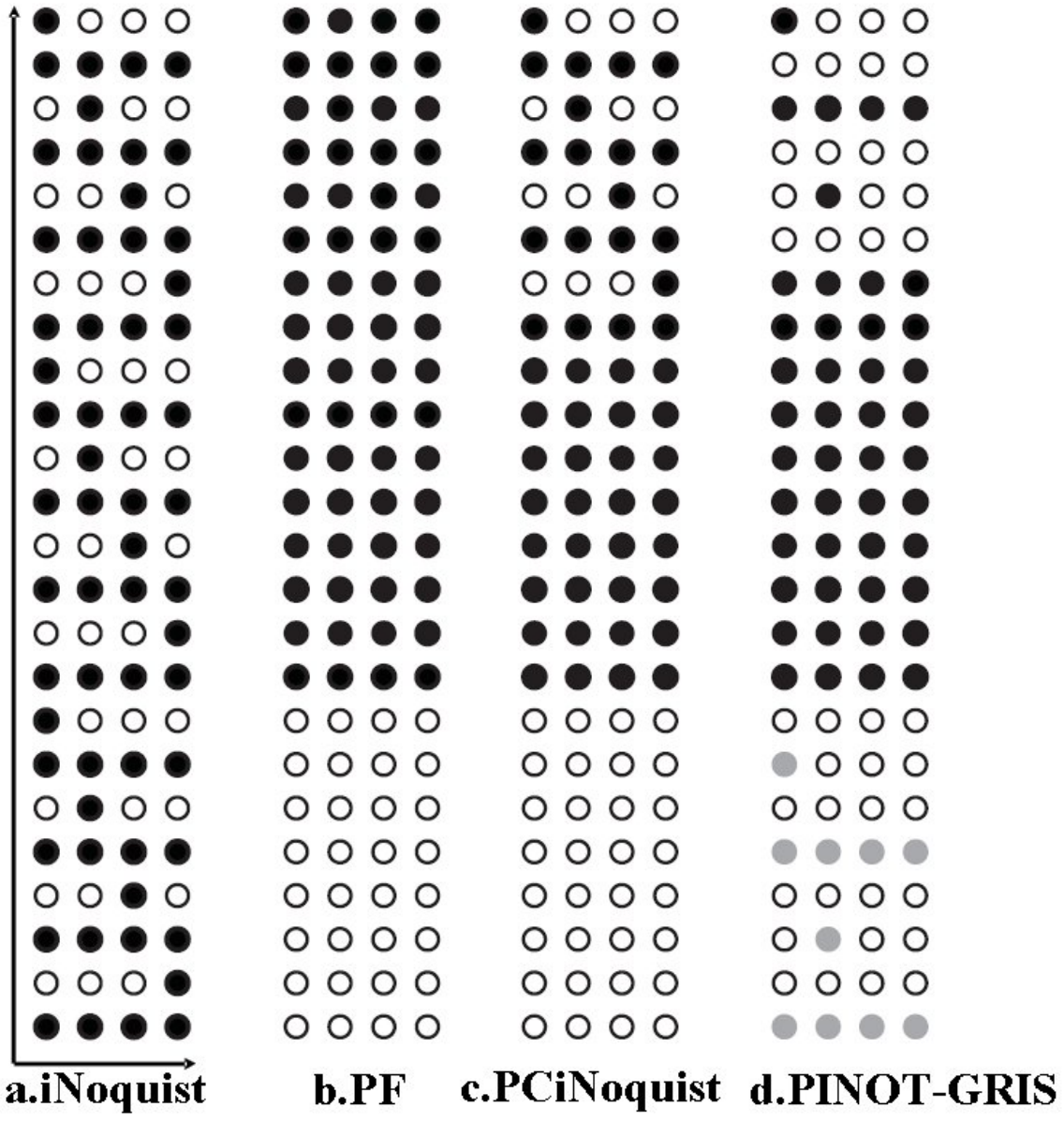

Figure 33: Sampling patterns, an example with 24 phase-encodings and 4 temporal frames, for (a) iNoquist with 50% static FOV, (b) Partial Fourier, (c) Phase Constrained iNoquist and (d) PINOT-GRIS. The horizontal axis represents time and the vertical axis represents the phase encoding direction. Acquired data are shown in black dots, and omitted k-space views in white and gray.

frame and distributing odd k-space lines across the cardiac phases, shown in Fig 33a. PF acquires half-plane k-space data and a symmetric k-space center for phase estimation, shown in Fig. 33b. Phase-constrained iNoquist (Fig. 33c) combines stairwell-reduced half-plane sampling with the same k-space center. Fig 33d shows the sampling pattern for PINOT-GRIS. The upper half-plane of k-space is sampled following the PINOT scheme for each time point, augmented by a symmetric fully-sampled central k-space region, used commonly in PF imaging to estimate a spatially band-limited image phase map.

5.7 Experiments

The proposed iNoquist was evaluated with one computer simulated dataset and three real MRI datasets. Other than the computer simulated dataset and two GE real MRI datasets (details in chapter 3) introduced earlier, an additional data set from a Philips Intera 1.5T imager (R10.3) was used here with a 5-element cardiac synergy coil. For a 2-chamber view cine MRI scan (Philips) a balanced FFE SSFP sequence was used with slice thickness 8 mm, TR = 4.4ms, TE = 2.2ms, flip angle deg 45, 232 phase encodings, 512 read-out samples, and 20 temporal frames. All reconstruction methods were implemented in MATLAB 2010b (The Mathworks, Natick, MA) on a on a Quad Core Xeon 2.66GHz CPU with 16GB RAM. All reconstructed images in the same figure are shown on the same scale for visual evaluation of image quality.

For testing iNoquist and its combined methods, we designed four experiments to demonstrate and evaluate its feasibility and performance. In the first experiment, iNoquist ($R = 1.875$) was initially tested using computer simulated data with Gaussian noise, comparing with corresponding Noquist and UNFOLD, followed by an iNoquist reconstruction on a real two chamber MRI data experiment. In the second experiment, we applied iNoquist as a post processing method to parallel imaging method on a real MRI data set, in comparison with corresponding SPACE-RIP, with reduction

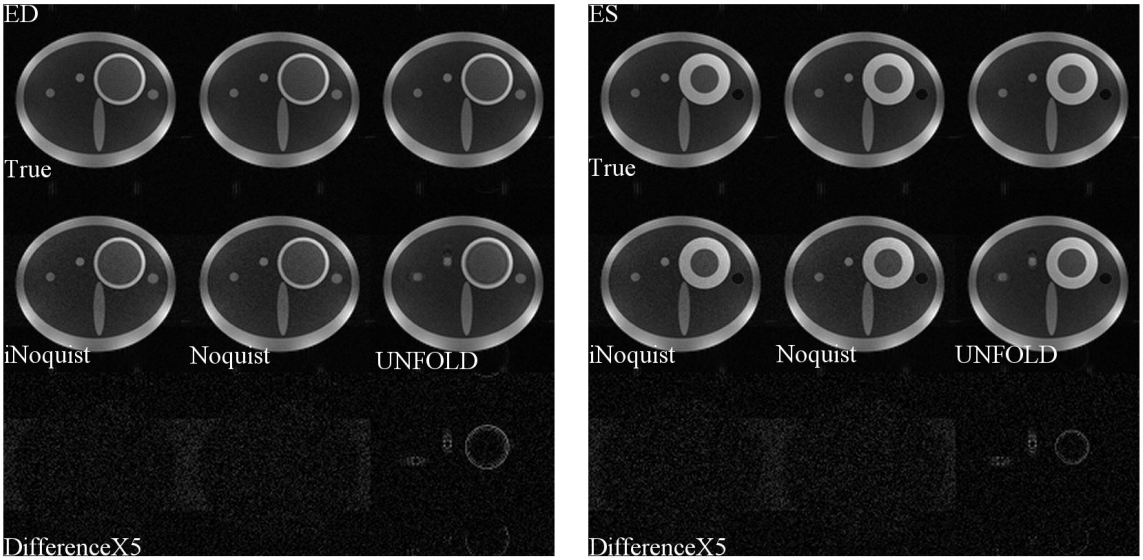

Figure 34: iNoquist, Noquist, and UNFOLD reconstruction comparison of the diastole and systole frames from a 15-frame computer simulated data set with noise with reduction factor 1.875, 1.875 and 2. The absolute differences between iNoquist, Noquist, and UNFOLD with the full-grid reconstruction are also displayed (difference images are enlarged 5 times to see the details, then all the images are shown under the same scale).

factor $R = 4$. A common subset sampling scheme for SENSE/SPACE-RIP is used, simply acquiring every fourth phase encoding line. The third experiment compared phase-constrained iNoquist with the corresponding iNoquist and PF. Reduction factors are 2.2, 1.87 and 1.6 respectively with 50% dynamic FOV for iNoquist. The sampling schemes of three methods are illustrated in Fig. 4.4. In the fourth experiment, PINOT-GRIS was compared with corresponding PINOT and PF reconstructions, using a 50% dynamic FOV for Noquist. All three methods (partial Fourier, PINOT and PINOT-GRIS) have reduction factors of 1.75, 3.5 and 3.8, respectively.

5.8 Results

Experiment 1 iNoquist results:

Figure 34 shows the comparison in spatial domain of iNoquist, Noquist, and UNFOLD at simulated diastole and systole for noisy computer simulated data. All three methods yielded visually good image quality for acceleration factor 1.875, 1.875 and

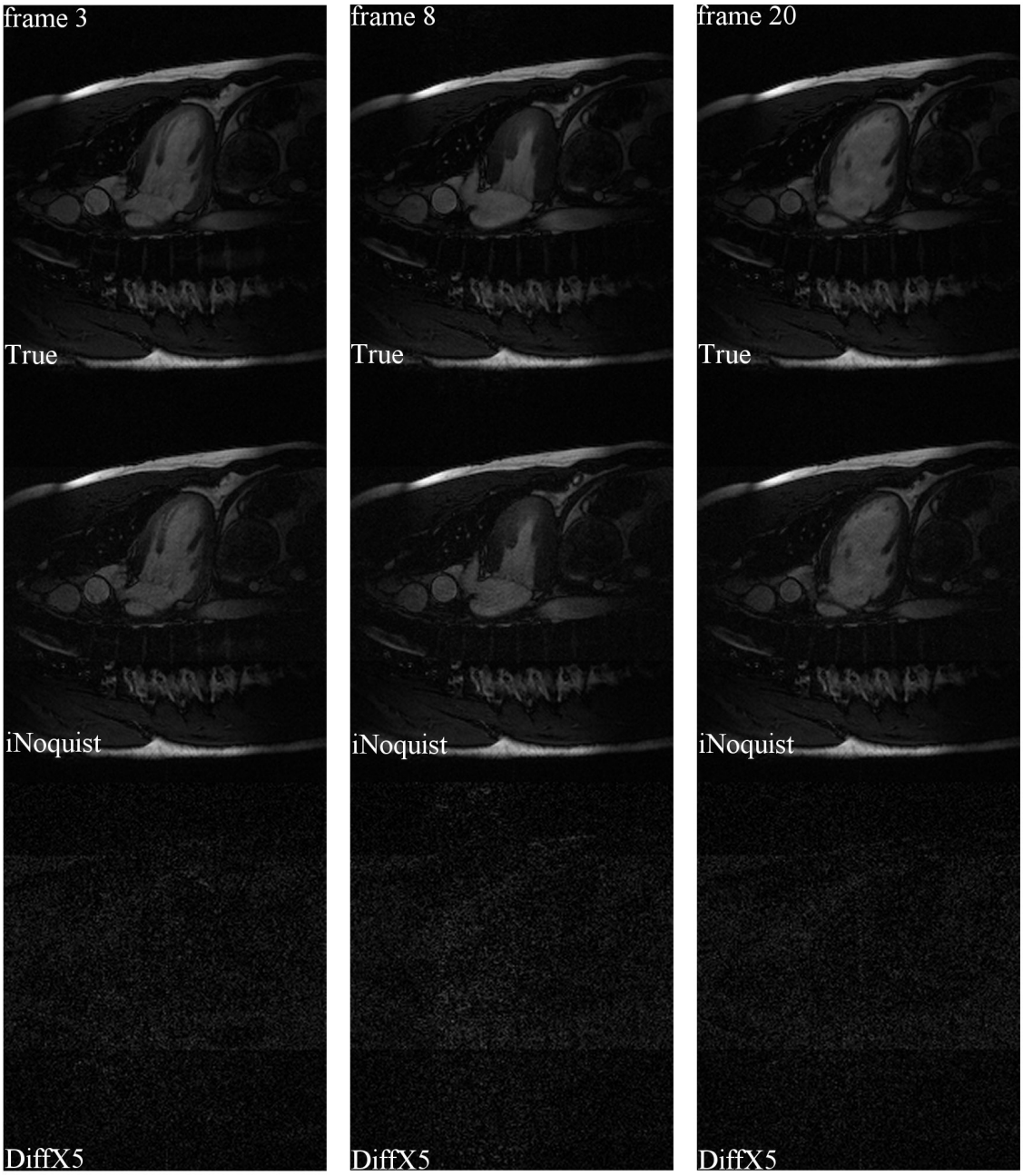

Figure 35: Conventional full-grid "true" images results (top row) for a retrospectively sub-sampled real MRI scan, compared with iNoquist ($R = 1.875$) (middle row) for three different image frames (frames 3, 8, and 20 of a 20 frame series). The bottom row shows the corresponding difference images (with an intensity multiplication factor of 5).

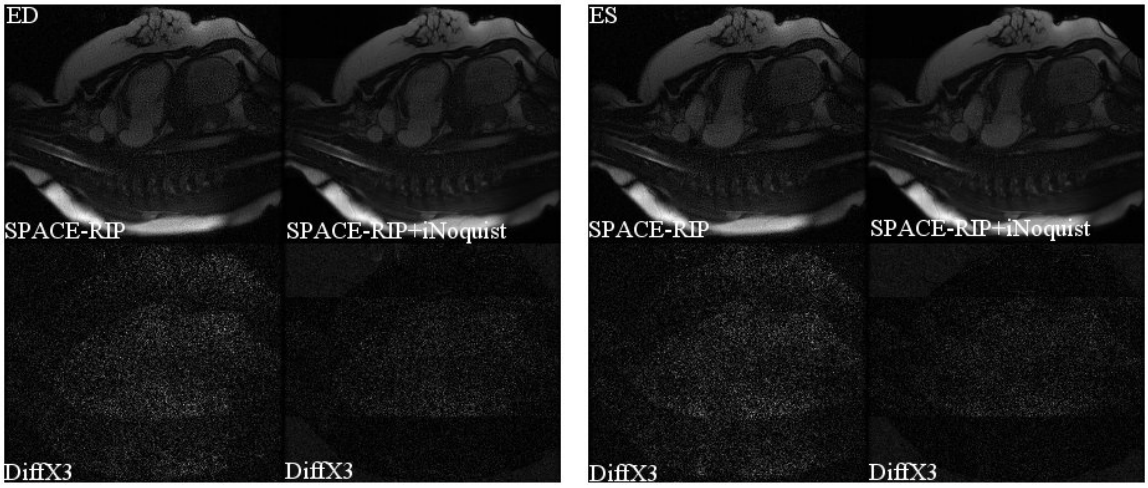

Figure 36: shows SPACE-RIP (R=4) and SPACE-RIP with iNoquist($R = 4$) reconstructions of end diastole (frame 1) and systole (frame 6). The bottom row shows differences from truth (i.e., a full-grid reconstruction), amplified by a factor of 3 to see the details.

2. UNFOLD displayed residual edge blurring at simulated myocardial boundaries and blood vessels during systolic contraction and diastolic relaxation, as well as ghost artifacts. iNoquist and Noquist do not show any edge artifact but higher random noise level in dynamic region. Furthermore, it appears that iNoquist and Noquist show no difference. Figure 35 shows iNoquist reconstructions (frames 3, 8, and 20) of a 20-frame two chamber MRI scan. The iNoquist reduction factor was 1.875 (50% dynamic FOV). These real MRI reconstruction results further confirm the edge detail preservation property of iNoquist, observed also from computer simulated data.

Experiment 2 SENSE with iNoquist results:

Fig. 36 shows a comparison of SPACE-RIP, SPACE-RIP with iNoquist with reduction factors $R = 4$. End-diastole (ED) and End-systole (ES) reconstructions demonstrate that SPACE-RIP with iNoquist provides a greater suppression of noise levels compared with SENSE for the same reduction factor 4. Successive application of iNoquist after SENSE reconstruction leads to further noise suppression, while retaining image resolution. Respective reconstruction times for SPACE-RIP and SPACE-RIP with iNoquist are 2 minutes 18 seconds and 3 minutes 21 seconds respectively.

Experiment 3 Phase-constrained iNoquist results:

The iNoquist ($R = 1.875$), PF ($R = 1.6$) and phase-constrained iNoquist ($R = 2.2$) results from retrospectively subsampled data are presented in Fig 37. Corresponding difference images between reconstructed and full-grid images were amplified 3 times to reveal details. iNoquist displays higher noise levels in dynamic regions, and the PF method shows some phase errors while phase-constrained iNoquist achieves higher reduction factor and better phase correction compared with PF.

Experiment 4 PINOT-GRIS results:

The PF ($R = 1.7$), PINOT ($R = 3.5$) and PINOT-GRIS ($R = 3.8$) results are shown in Fig 38 for end-diastolic and end-systolic frames, where the bottom row shows differences from full-grid reconstructions amplified 3 times for visibility. PINOT shows good edge preservation and shows the expected noise level penalty. PF results show artifacts in areas with rapid phase changes, demonstrating that the method is very sensitive to the accuracy of phase estimates. In comparison, with the same phase estimates, the combined method PINOT-GRIS mitigates phase artifact dramatically, and inherits both PINOT and PF methods' properties, resulting in some residual phase artifacts and noise level increase. PINOT-GRIS converges quickly, typically around 5 iterations.

5.9 Discussion

The proposed iterative method iNoquist, similar to Noquist, yields anticipated no edge information loss but has noise amplification in dynamic regions relative to full-grid images, which is similar to Noquist. Higher sampling rate/reduction factor for parallel imaging is desired but usually limited due to ill-posed inverse problem resulted in higher noise level and even hot spots in the reconstructed images. Compared with parallel imaging alone with the same reduction factor, Combination of SPACE-RIP

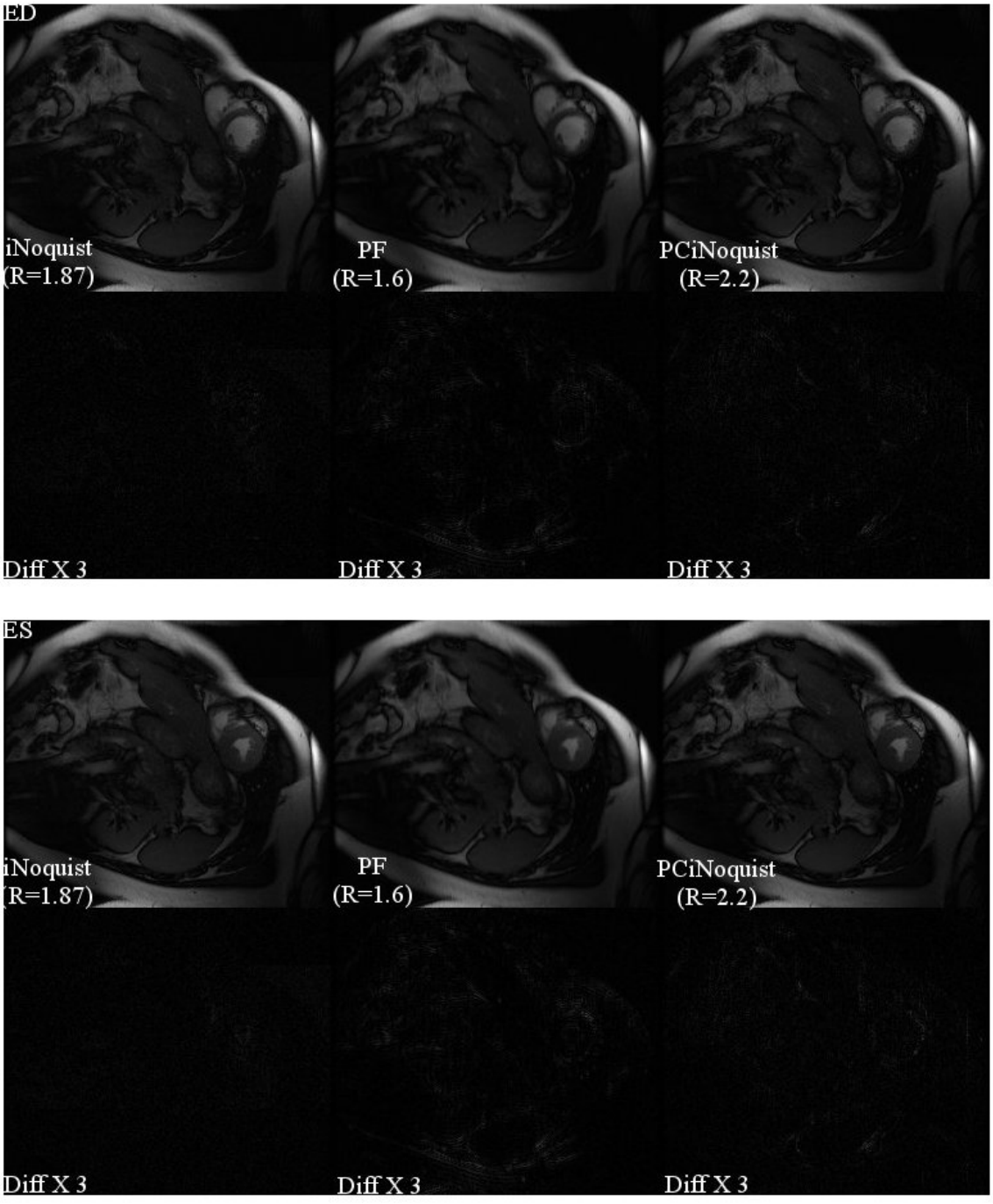

Figure 37: iNoquist, PF and phase constrained iNoquist reconstruction comparison (top row) of the end-diastole (frame 1) and end-systole (frame 8) frames. The bottom row shows the corresponding difference images with a scale factor 3 for visibility.

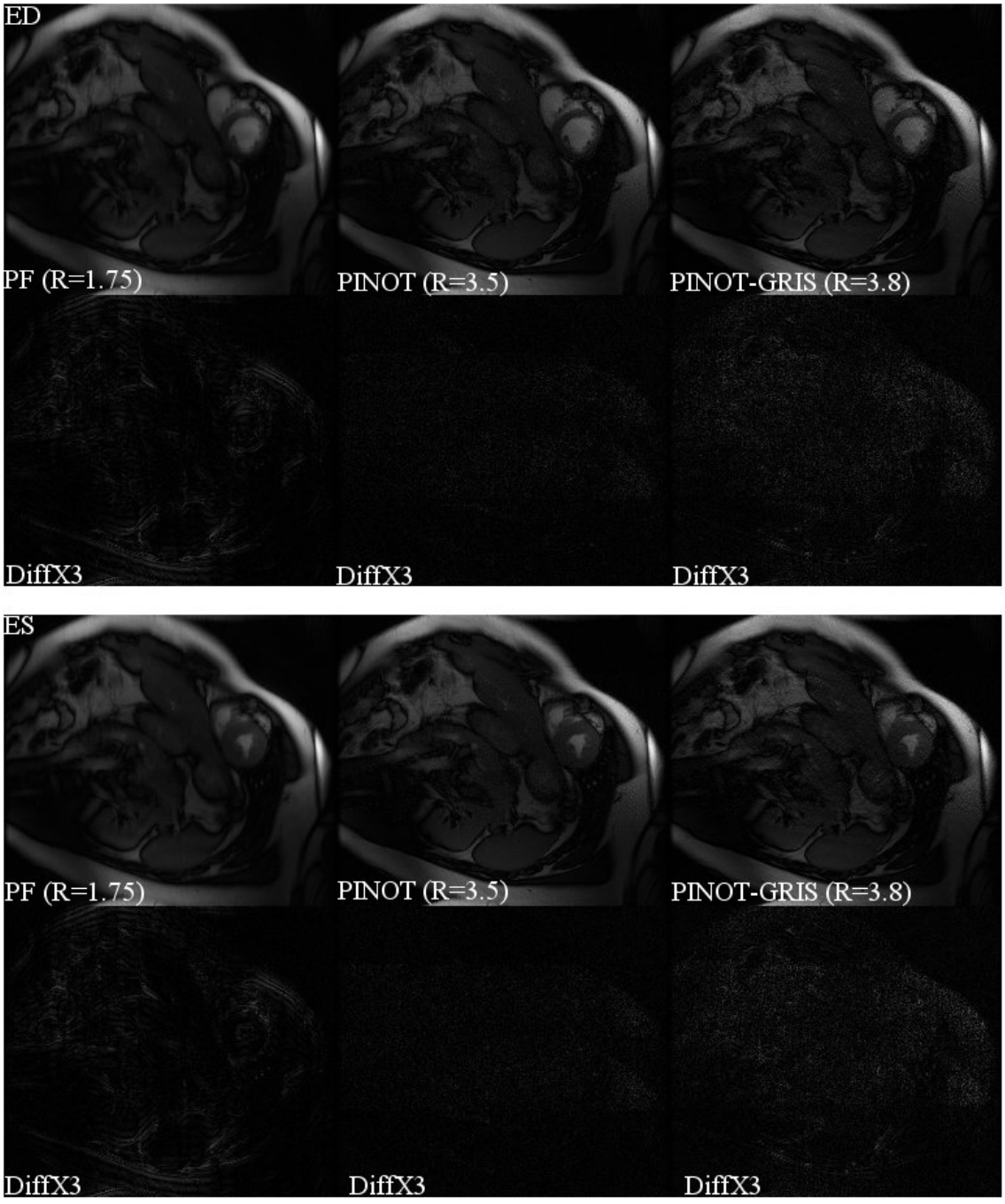

Figure 38: iNoquist, PF and phase constrained iNoquist reconstruction comparison (top row) of the end-diastole (frame 1) and end-systole (frame 8) frames. The bottom row shows the corresponding difference images with a scale factor 3 for visibility.

with iNoquist suppresses the noise level and residual artifacts. Compared with integrated PINOT, it has the advantage of alleviating computational burden, even though it does not achieve the same overall image quality. Furthermore, although illustrated here only for SPACE-RIP, we note that iNoquist can be used as a post processing method following any parallel imaging method to suppress residual noise and artifacts. Phase-constrained iNoquist proposes a successful first combination of a PF method with a rFOV (iNoquist) approach for reduction factor higher than 2. Compared with individual methods which each have reduction factor below 2 in most cases, phase-constrained iNoquist provides a higher acceleration gain and improvements of phase accuracy compared with Partial Fourier imaging. PINOT-GRIS combines three sources of data redundancy from parallel imaging, rFOV method and partial Fourier method to speed up imaging. This method suppresses phase errors when partial Fourier method alone does not work well but pays the price of higher noise level. PINOT reconstruction involves big matrices inversion and is time-consuming, here the proposed PINOT-GRIS is even more computational challenge. Furthermore, adding more and more sources of prior information (i.e., fully sampled low frequency k-space data are needed for phase estimates in addition to the PINOT sampling k-space data) causes diminishing returns in overall combined reduction factor and may be difficult to find an SNR-optimal sampling pattern.

5.10 Summary

In this chapter, we proposed three accelerated imaging methods based on Papoulis-Gerchberg algorithm. The proposed iterative method, iNoquist, yields spatial resolution preservation but noise amplification in dynamic regions relative to full-grid images. Successive combination of SPACE-RIP with iNoquist demonstrates further suppression of the noise level and residual artifacts. Phase-constrained iNoquist provides a higher acceleration gain and improves phase correction compared with Partial

Fourier imaging. PINOT-GRIS, for the first time, combines three sources of data redundancy from parallel imaging, rFOV method and partial Fourier method to speed up imaging. The experiment on PINOT-GRIS demonstrates the successful reconstruction for the proposed method with phase errors suppression but pays the price of higher noise level and computational time.

CHAPTER VI

CONCLUSION AND FUTURE WORK

6.1 Conclusion

The central goal of this thesis are to develop novel reduced-data imaging methods for cardiac MRI to improve reconstructed image performance. In summary, this thesis explores several new techniques of reduced-data imaging in MRI and the findings are as follows.

- As illustrated by a variety of computer simulated and real cardiac MRI data experiments, the proposed reduced-data imaging method, PINOT, can be successfully applied to the reconstruction of undersampled MR images. It preserves image spatial-temporal resolution of corresponding fully sampled scans, retaining edge information better than comparable methods like TSENSE and k-t SENSE around reduction factor 4, but with higher random noise level in dynamic regions. An explanation for these is the fact that as a combination of Noquist and SPACE-RIP, PINOT does not apply any filter or implicit regularization. In clinical analysis of cardiac function, accurate detection of myocardial boundary locations is critically important. From this perspective PINOT has a spatial-temporal resolution advantage, but this must be weighed against the SNR penalty and higher computational cost.

- For the cases when images have implicitly low SNR, or high acceleration factor, the noise amplification penalty of PINOT becomes a dominating factor in image quality. Regularization must be applied to improve the SNR, but lose edge details and have increased computational burden.

- An additional significant time savings is achieved by providing a favorable initial estimate which is close to the solution, calculated based on PINOT matrix's block structure, for CG PINOT reconstruction.

- Like all other parallel imaging methods, PINOT reconstruction quality depends on the estimate accuracy of the sensitivity maps. Estimation of sensitivity maps remain a challenge in cardiac MRI. Other than the pre-calculated sensitivity maps estimated from pre-scan, PINOT offers the option of using auto-calibrated signals, acquired simultaneously during actual scan, to calculate coil sensitivity maps.

- The Gerchberg Reduced Iterative System, implemented with the Gerchberg-Papoulis (GP) algorithm, allows flexible incorporation of multiple constraints and offers convenient implementation for combining different reduced-data imaging methods.

- The proposed iterative iNoquist method, under Gerchberg Reduced Iterative System, yields spatial resolution preservation but noise amplification in dynamic regions relative to full-grid images. It has the same performance as the Noquist method but is more flexible and can be easily combined with other reduced-data imaging methods.

- Successive combination of SPACE-RIP with iNoquist suppressed the noise level and residual artifacts, demonstrating that iNoquist can be valuable as a post-processing technique for parallel imaging methods for improving image quality.

- A novel phase-constrained iNoquist method was developed, for the first time combining Partial Fourier with a reduced FOV method. Compared with individual methods which have limited reduction factor smaller than 2 in most cases, the phase-constrained iNoquist method provides a higher acceleration

gain and achieves improved phase correction compared with the partial Fourier method.

- PINOT-GRIS was developed, combining for the first time three different sources of data redundancy from parallel imaging, rFOV method and partial Fourier to speed up imaging. The proof of concepts showed stable results that PINOT-GRIS suppresses phase errors when partial Fourier does not work well but pays the price of higher noise level and is computationally challenging.

6.2 Future Work

The remain unexplored areas for the future continued research are as follows:

- A major drawback of advanced techniques for image reconstruction is the increased computation time. While such methods are right now not practical in clinical settings, the situation may change in the near future. With more extensive use of parallel computing, for example using recently popularized GPU processing methods [17, 60], further savings in computation time may be realized.

- Because noise amplification is the limiting factor in reduced-data imaging for higher acceleration situation, Tikhonov regularization has been applied to improve the SNR, but tends to oversmooth reconstructed images and lose edge details. A better regularization scheme, such as total variation regularization, which may preserve image resolution, may be used.

- Another remaining issue that needs to be addressed is the challenge in calculating sensitivity maps. A particular challenge in cardiac imaging, is that there are large areas (for example, lung) which contribute little or no signals, which needs interpolation techniques to fill in the holes. However, an open area in research

would be to use advanced image processing techniques (image interpolation) to improve sensitivity maps accuracy.

APPENDIX A

DERIVATION OF BLOCKMATRIX

PINOT is a direct-inversion method for parallel MRI. In order to obtain the image $\boldsymbol{f}$ from the received signal $\boldsymbol{F}$, we need to solve the following equation.

$$\boldsymbol{F} = \boldsymbol{M}_{PINOT}\boldsymbol{f} \tag{A.1}$$

There are numerous methods for solving this equation from calculating the pseudo-inverse of $\boldsymbol{M}_{PINOT}$ to gaussian elimination and conjugate gradient. The problem is that the size of the matrix $\boldsymbol{M}_{PINOT}$ is quite large for a typical image, having dimensions $TN_cN_{sample\_PI} \times TN_D + N_S$, where T is the number of frames, c is the number of coils, N_{sample_PI} is the number of samples per column, and N_S and N_D are the number of pixels in the static and dynamic regions respectively.

Consider the transform matrix for PINOT from 3.4. We can combine the submatrices for all the coils in a single frame as:

$$\boldsymbol{M}_{PINOT} = \begin{bmatrix} \boldsymbol{P}_1^{N_P \times N_S} & \boldsymbol{D}_1^{N_P \times N_D} & \mathbf{0} & \cdots & \mathbf{0} \\ \boldsymbol{P}_2^{N_P \times N_S} & \mathbf{0} & \boldsymbol{D}_2^{N_P \times N_D} & \cdots & \mathbf{0} \\ \vdots & \vdots & \vdots & \ddots & \vdots \\ \boldsymbol{P}_T^{N_P \times N_S} & \mathbf{0} & \mathbf{0} & \cdots & \boldsymbol{D}_T^{N_P \times N_D} \end{bmatrix},$$

where $N_P = N_cN_{sample\_PI}$.

The problem in (A.1) can be solved if we can determine an "inverse" of $\boldsymbol{M}_{PINOT}$ that will satisfy the equation

$$\boldsymbol{M}_{PINOT}^{\dagger}\boldsymbol{M}_{PINOT} = \boldsymbol{I}, \tag{A.2}$$

where $\boldsymbol{I}$ is the $TN_D + N_S \times TN_D + N_S$ identity matrix. Note that this is less stringent than the pseudo-matrix since we do not require $\boldsymbol{M}_{PINOT}\boldsymbol{M}_{PINOT}^{\dagger}$ to be Hermitian.

By dropping this requirement, we will be losing some noise resistance relative to solving the full matrix.

We will demonstrate that there exists "inverse" of $\boldsymbol{M}_{PINOT}$ that solves (A.2) of the form:

$$\boldsymbol{M}_{PINOT}^{\dagger} = \begin{bmatrix} \boldsymbol{X}_1^{N_S \times N_P} & \boldsymbol{X}_2^{N_S \times N_P} & \cdots & \boldsymbol{X}_T^{N_S \times N_P} \\ \boldsymbol{Y}_1^{N_D \times N_P} & \boldsymbol{0} & \cdots & \boldsymbol{0} \\ \boldsymbol{0} & \boldsymbol{Y}_2^{N_D \times N_P} & \cdots & \boldsymbol{0} \\ \vdots & \vdots & \ddots & \vdots \\ \boldsymbol{0} & \boldsymbol{0} & \cdots & \boldsymbol{Y}_T^{N_D \times N_P} \end{bmatrix}$$

We find the product of the two matrices is of the form:

$$\boldsymbol{M}_{PINOT}^{\dagger}\boldsymbol{M}_{PINOT} = \begin{bmatrix} \sum_{t=1}^{T} \boldsymbol{X}_t\boldsymbol{P}_t & \boldsymbol{X}_1\boldsymbol{D}_1 & \boldsymbol{X}_2\boldsymbol{D}_2 & \cdots & \boldsymbol{X}_T\boldsymbol{D}_T \\ \boldsymbol{Y}_1\boldsymbol{P}_1 & \boldsymbol{Y}_1\boldsymbol{D}_1 & \boldsymbol{0} & \cdots & \boldsymbol{0} \\ \boldsymbol{Y}_2\boldsymbol{P}_2 & \boldsymbol{0} & \boldsymbol{Y}_2\boldsymbol{D}_2 & \cdots & \boldsymbol{0} \\ \vdots & \vdots & \vdots & \ddots & \vdots \\ \boldsymbol{Y}_T\boldsymbol{P}_T & \boldsymbol{0} & \cdots & \cdots & \boldsymbol{Y}_T\boldsymbol{D}_T \end{bmatrix}$$

In order for this to evaluate to the identity matrix, the following conditions must be met:

1. $\sum_{t=1}^{T} \boldsymbol{X}_t\boldsymbol{P}_t = \boldsymbol{I}$
2. $\boldsymbol{X}_t\boldsymbol{D}_t = \boldsymbol{0}$, $\forall_t$
3. $\boldsymbol{Y}_t\boldsymbol{P}_t = \boldsymbol{0}$, $\forall_t$
4. $\boldsymbol{Y}_t\boldsymbol{D}_t = \boldsymbol{I}$, $\forall_t$

We further restrict condition 1 by requiring $T\boldsymbol{X}_t\boldsymbol{P}_t = \boldsymbol{I}$, $\forall_t$. By adding this restriction we are able to completely separate the problems in terms of the frame index t. We can then deconstruct the problem into a series of pseudo-inversions for each frame:

$$\begin{bmatrix} T\boldsymbol{X}_t \\ \boldsymbol{Y}_t \end{bmatrix} \begin{bmatrix} \boldsymbol{P}_t & \boldsymbol{D}_t \end{bmatrix} = \begin{bmatrix} \boldsymbol{I} & \boldsymbol{0} \\ \boldsymbol{0} & \boldsymbol{I} \end{bmatrix}$$

Each of these inversions can be solved relatively quickly, allowing the entire problem to be approximately solved with less computation.

REFERENCES

[1] Barrett, H. and Myers, K., *Foundations of Image Science*. Hoboken, New Jersey: Wiley, 2003.

[2] Breuer, F., Kellman, P., Griswold, M., and Jakob, P., "Dynamic autocalibrated parallel imaging using temporal grappa (TGRAPPA)," *Magnetic Resonance in Medicine*, vol. 53, pp. 981–985, 2005.

[3] Brummer, M., Moratal-Prez, D., Hong, C., Pettigrew, R., Millet-Roig, J., and Dixon, W., "Noquist: Reduced field-of-view imaging by direct fourier inversion," *Magnetic Resonance in Medicine*, vol. 51, pp. 331–342, Feb 2004.

[4] Bydder M, R. M., "Partial fourier partially parallel imaging," *Magnetic Resonance in Medicine*, vol. 53, pp. 1393–1401, 2005.

[5] Candes, E., Romberg, J., and Tao, T., "Robust uncertainty principles: Exact signal reconstruction from highly incomplete frequency information," *IEEE Transactions on Information Theory*, vol. 52, pp. 489–509, 2006.

[6] Cheng, D., *Field and wave electromagnetics*. Reading, Massachusetts: Addison-Wesley, 1989.

[7] Cuppen, J. and Van, E., "Reducing mr imaging time by one-sided reconstruction," *Magnetic Resonance Imaging*, vol. 5, pp. 526–527, 1987.

[8] D.A., F., J.D., H., J.C., W., L., K., and A., M., "Halving mr imaging time by conjugation: demonstration at 3.5 kg," *Radiology*, vol. 161, pp. 527–531, 1986.

[9] Dietrich, O., Raya, J., Reeder, S., Reiser, M., and Schoenberg, S., "Measurement of signal-to-noise ratios in mr images: influence of multichannel coils, parallel imaging, and reconstruction filters," *Journal of Magnetic Resonance Imaging*, vol. 26, pp. 375–385, Aug. 2007.

[10] Donoho, D., "Compressed sensing," *IEEE Transactions on Information Theory*, vol. 52, pp. 1289–1306, 2006.

[11] Gerchberg, R., "Super-resolution through error energy reduction," *Journal of Modern Optics*, vol. 21, pp. 709–720, 1974.

[12] Griswold, M., Breuer, F., Blaimer, M., Kannengiesser, S., Heidemann, R., Mueller, M., Nittka, M., Jellus, V., Kiefer, B., and Jakob, P., "Autocalibrated coil sensitivity estimation for parallel imaging," *NMR in Biomedicine*, vol. 19, pp. 316–324, May 2006.

[13] Griswold, M. A., Jakob, P. M., Nittka, M., Goldfarb, J. W., and Haase, A., "Partially parallel imaging with localized sensitivities (PILS)," *Magnetic Resonance in Medicine*, vol. 44, pp. 602–609, Oct. 2000.

[14] Griswold, M. A., Jakob, P. M., R.M., H., Nittka, M., Jellus, V., Wang, J., Kiefer, B., and Haase, A., "Generalized autocalibrating partially parallel acquisitions (GRAPPA)," *Magnetic Resonance in Medicine*, vol. 47, pp. 1202–1210, Jun 2002.

[15] Haacke, E., Lindskog, E., and Lin, W., "A fast, iterative, partial-fourier technique capable of local phase recovery," *Journal of Magnetic Resonance Imaging*, vol. 92, pp. 126–145, 1991.

[16] Haccke, E., Brown, R., Thompson, M., and Venkatesan, R., *Magnetic Resonance Imaging: Physical Principles and Sequence Design*. Wiley-Liss, 1999.

[17] Haldar, J., Stone, S., Yi, H., Tsao, S., Sutton, B., Hwu, W.-M., and Liang, Z., "Fast mr image reconstruction using graphics processing units," in *The 14th International Society for Magnetic Resonance in Medicine Scientific Meeting & Exhibition (ISMRM 2008)*, (Toronto, Canada), p. 1493, ISMRM, May 2008.

[18] Hamilton, L., Fabregat, J., Moratal, D., Ramamurthy, S., and Brummer, M., "Time-resolved parallel imaging with a reduced dynamic field of view," in *IEEE International Symposium on Biomedical Imaging:From Nano to Macro(ISBI 2008)*, (Paris, France), pp. 1023–1026, IEEE, April 2008.

[19] Hamilton, L., Fabregat, J., Moratal, D., Ramamurthy, S., Lerakis, S., Parks, W., Sallee, D. I., and Brummer, M., ""PINOT": Time-resolved parallel magnetic resonance imaging with a reduced dynamic field of view," *Magnetic Resonance in Medicine*, vol. 65, pp. 1062–1075, Apr. 2011.

[20] Hamilton, L., Hamilton, B., Ramamurthy, S., and Brummer, M., "Conjugate gradient PINOT reconstruction with a fast initial estimate.," in *The 18th International Society for Magnetic Resonance in Medicine Scientific Meeting & Exhibition (ISMRM 2010)*, (Stockholm, Sweden), p. 2890, ISMRM, May 2010.

[21] Hamilton, L., Javier, F., Moratal, D., Ramamurthy, S., and Brummer, M., "GRAPPA-enhanced autocalibration for PINOT reconstruction.," in *ISMRM Third International Workshop on Parallel MRI*, (Santa Cruz, CA), ISMRM, Oct 2009.

[22] Hamilton, L., Javier, F., Moratal, D., Ramamurthy, S., K., S., and Brummer, M., "Comparison of TSENSE, k-t SENSE and PINOT fast imaging methods on cine MRI.," in *The 17th International Society for Magnetic Resonance in Medicine Scientific Meeting & Exhibition (ISMRM 2009)*, (Honolulu, HI), p. 4558, ISMRM, May 2009.

[23] Hamilton, L., Krishnan, S., Ramamurthy, S., Moratal, D., and Brummer, M., "Suppression of residual noise and artifact in parallel imaging by iterative noquist.," in *The 19th International Society for Magnetic Resonance in Medicine Scientific Meeting & Exhibition (ISMRM 2011)*, (Montreal, Canada), p. 4403, ISMRM, May 2011.

[24] Hansen, P., "Regularization tools: A matlab package for analysis and solution of discrete ill-posed problems," *Numerical Algorithms*, vol. 6, pp. 1 – 35, 1994.

[25] Heidemann, R., Griswold, M., Haase, A., and Jakob, P., "VD-AUTO-SMASH imaging," *Magnetic Resonance Materials in Physics Biology and Medicine*, vol. 45, pp. 1066–1074, 2001.

[26] Hoge, W. and Brooks, D., "Using GRAPPA to improve autocalibrated coil sensitivity estimation for the SENSE family of parallel imaging reconstruction algorithms," *Magnetic Resonance in Medicine*, vol. 60, pp. 462–467, Aug. 2008.

[27] Hoge, W., Brooks, D., Madore, B., and Kyriakos, W., "On the regularization of Sense and Space-RIP in parallel MR imaging," in *IEEE International Symposium on Biomedical Imaging:From Nano to Macro(ISBI 2004)*, (Arlington, VA, USA), pp. 241–244, IEEE, April 2004.

[28] Huang, F., Akao, J., Vijayakumar, S., Duensing, G., and Limkeman, M., "k-t GRAPPA: a k-space implementation for dynamic mri with high reduction factor," *Magnetic Resonance in Medicine*, vol. 54, pp. 1172–1184, Nov. 2005.

[29] Huang, F., Chen, Y., Duensing, G., Akao, J., Rubin, A., and Saylor, C., "Application of partial differential equation-based inpainting on sensitivity maps," *Magnetic Resonance in Medicine*, vol. 53, pp. 388–397, Feb. 2005.

[30] Huang, F., Lin, W., and Li, Y., "Partial fourier reconstruction through data fitting and convolution in k-space," *Magnetic Resonance in Medicine*, vol. 62, pp. 1261–1269, 2009.

[31] Jacob, M., Xu, D., and Liang, Z., "Optimal selection of phase encodings in parallel MR imaging," in *Second International Workshop on Parallel MRI)*, (Zurich, Switzerland), p. 55, ISMRM, Oct 2004.

[32] Jakob, P., Griswold, M., Edelman, R., and Sodickson, D., "AUTO-SMASH: a self-calibrating technique for smash imaging. simultaneous acquisition of spatial harmonics," *Magnetic Resonance Materials in Physics Biology and Medicine*, vol. 7, pp. 42–54, 1998.

[33] Jung, H., Sung, K., Nayak, K., Kim, E., and Ye, J., "k-t FOCUSS: a general compressed sensing framework for high resolution dynamic mri.," *Magnetic Resonance in Medicine*, vol. 61, pp. 103–116, Jan 2009.

[34] Kellman, P., Epstein, F., and McVeigh, E., "Adaptive sensitivity encoding incorporating temporal filtering (TSENSE)," *Magnetic Resonance in Medicine*, vol. 45, pp. 846–852, May 2001.

[35] Kellman, P., Epstein, F., and McVeigh, E., *The development of TSENSE*. Parallel Imaging in Clinical MR Applications, Heidelberg: Springer, 2007.

[36] Krishnan, S., Moratal, D., Hamilton, L., Ramamurthy, S., and Brummer, M., "Reconstruction of sparsely-sampled dynamic mri data using iterative "error energy" reduction.," in *The 18th International Society for Magnetic Resonance in Medicine Scientific Meeting & Exhibition (ISMRM 2010)*, (Stockholm, Sweden), p. 2867, ISMRM, May 2010.

[37] Kyriakos, W., Panych, L., Kacher, D., Westin, C., Bao, S., Mulkern, R., and Jolesz, F., "Sensitivity profiles from an array of coils for encoding and reconstruction in parallel (SPACE RIP)," *Magnetic Resonance in Medicine*, vol. 44, pp. 301–308, Aug 2000.

[38] Liang, D., Liu, B., Wang, J., and Ying, L., "Accelerating SENSE using compressed sensing," *Magnetic Resonance in Medicine*, vol. 62, pp. 1574–1584, Dec. 2009.

[39] Liang, Z. and Lauterbur, P., *Principles of Magnetic Resonance Imaging: A Signal Processing Perspective*. New York, New Jersey: Wesley-IEEE Press, 2000.

[40] Lin, F., Chen, Y., Belliveau, J., and Wald, L., "A wavelet-based approximation of surface coil sensitivity profiles for correction of image intensity inhomogeneity and parallel imaging reconstruction," *Human Brain Mapping*, vol. 19, pp. 96–111, 2003.

[41] Lin, F., Kwong, K., Belliveau, J., and Wald, L., "Parallel imaging reconstruction using automatic regularization," *Magnetic Resonance in Medicine*, vol. 51, pp. 559–567, Mar. 2004.

[42] Lustig, M., Alley, M., Vasanawala, S., Donoho, D., and Pauly, J., "L1 spirit: Autocalibrating parallel imaging compressed sensing," in *The 17th International Society for Magnetic Resonance in Medicine Scientific Meeting & Exhibition (ISMRM 2009)*, (Honolulu, HI), p. 379, ISMRM, May 2009.

[43] Lustig, M., Donoho, D., and Pauly, J., "Sparse mri: The application of compressed sensing for rapid MR imaging," *Magnetic Resonance in Medicine*, vol. 58, pp. 1182–1195, 2007.

[44] Lustig, M. and Pauly, J., "Iterative self-consistent parallel imaging reconstruction from arbitrary k-space," *Magnetic Resonance in Medicine*, vol. 64, pp. 457–471, Aug. 2009.

[45] Madore, B., "UNFOLD-SENSE: A parallel mri method with self-calibration and artifact suppression," *Magnetic Resonance in Medicine*, vol. 52, pp. 310–320, Aug 2004.

[46] Madore, B., Glover, G., and Pelc, N., "Unaliasing by fourier-encoding the overlaps using the temporal dimension (UNFOLD) applied to cardiac imaging and fmri," *Magnetic Resonance in Medicine*, vol. 42, pp. 813–828, Jun 1999.

[47] Margosian, P., Schmitt, F., and Purdy, D., "Faster mr imaging: imaging with half the data," *Health Care Instrum*, vol. 1, pp. 195–197, 1986.

[48] Minino, A., Arias, E., Kochanek, K., Murphy, S., and Smith, B., "Deaths: Final data for 2000," tech. rep., Department of Health and Human Services, National Center for Health Statistics, Sept. 2002.

[49] Moratal-Prez, D., Brummer, M., and Dixon, W., "Optimal data selection for "noQuist" reduced field of view (rFOV) imaging," in *The 14th International Society for Magnetic Resonance in Medicine Scientific Meeting & Exhibition (ISMRM 2006)*, (Seattle, WA), p. 3190, ISMRM, May 2006.

[50] Noll, D., Nishimura, D., and Macovski, A., "Homodyne detection in magnetic resonance imaging.," *IEEE Transanction on Medical Imaging*, vol. 10, pp. 154–163, Jun 1991.

[51] O., A., "Iteration number for the conjugate gradient method," *Mathematics and Computers in Simulation*, vol. 61, pp. 421 – 435, Jan. 2003.

[52] Ohliger, M., Grant, A., and Sodickson, D., "Ultimate intrinsic signal-to-noise ratio for parallel mri: electromagnetic field considerations," *Magnetic Resonance in Medicine*, vol. 50, pp. 1018–1030, 2003.

[53] Papoulis, A., "A new algorithm in spectral analysis and bandlimited extrapolation," *IEEE Transanctions on Circuits and Systems*, vol. 22, pp. 735–742, Sept. 1975.

[54] Pruessmann, K. P., Weiger, M., Scheidegger, M. B., and Boesiger, P., "SENSE: Sensitivity encoding for fast MRI," *Magnetic Resonance in Medicine*, vol. 42, pp. 952–962, Nov. 1999.

[55] Pruessmann, K., Weiger, M., Bornert, P., and Boesiger, P., "Advances in sensitivity encoding with arbitrary k-space trajectories," *Magnetic Resonance in Medicine*, vol. 46, pp. 638–651, Oct. 2001.

[56] Reeves, S. and Z., Z., "Sequential algorithms for observation selection," *IEEE Transactions on Signal Processing*, vol. 47, pp. 123–132, Jan. 1999.

[57] Roemer, P., Edelstein, W., Hayes, C., Souza, S., and Mueller, O., "The NMR phased array," *Magnetic Resonance in Medicine*, vol. 16, pp. 192–225, Nov. 1990.

[58] Samsonov, A., Kholmovski, E., Parker, D., and Johnson, C., "Pocsense: Pocs-based reconstruction for sensitivity encoded magnetic resonance imaging," *Magnetic Resonance in Medicine*, vol. 52, pp. 1397–1406, 2004.

[59] Sodickson, D. K. and Manning, W. J., "Simultaneous acquisition of spatial harmonics (SMASH): Fast imaging with radiofrequency coil arrays," *Magnetic Resonance in Medicine*, vol. 38, pp. 591–603, Oct 1997.

[60] Sorensen, T., Atkinson, D., Boubertakh, R., Schaeffter, T., and Hansen, M., "Rapid non-cartesian parallel imaging reconstruction on commodity graphics hardware," in *The 14th International Society for Magnetic Resonance in Medicine Scientific Meeting & Exhibition (ISMRM 2008)*, (Toronto, Canada), p. 1490, ISMRM, May 2008.

[61] Thunberg, P. and Zetterberg, P., "Noise distribution in SENSE- and GRAPPA-reconstructed images: a computer simulation study," *Magnetic Resonance in Medicine*, vol. 25, pp. 1089–1094, Sept. 2007.

[62] Tsao, J., Boesiger, P., and Pruessmann, K., "k-t blast and k-t sense: dynamic mri with high frame rate exploiting spatiotemporal correlations," *Magnetic Resonance in Medicine*, vol. 50, pp. 1031–1042, 2003.

[63] Tsao, J., Boesiger, P., and Pruessmann, K., "k-t GRAPPA: a k-space implementation for dynamic mri with high reduction factor," *Magnetic Resonance in Medicine*, vol. 54, pp. 1172–1184, Nov 2005.

[64] Uecker, M., Hohage, T., Block, K., and Frahm, J., "Image reconstruction by regularized nonlinear inversionjoint estimation of coil sensitivities and image content," *Magnetic Resonance in Medicine*, vol. 60, pp. 674–682, Sept. 2008.

[65] Wang, Z., Wang, J., and Detre, J., "Improved data reconstruction method for GRAPPA," *Magnetic Resonance in Medicine*, vol. 54, pp. 738–742, Sept. 2005.

[66] Webb, A., *Introduction to Biomedical Imaging*. Hoboken, New Jersey: Wesley-IEEE Press, 2003.

[67] Wiesinger, F., Boesiger, P., and Pruessmann, K., "Electrodynamics and ultimate SNR in parallel MR imaging," *Magnetic Resonance in Medicine*, vol. 52, pp. 376–390, 2004.

[68] Willig-Onwuachi, J., Yeh, E., Grant, A., Ohliger, M., McKenzie, C., and Sodickson, D., "Phase-constrained parallel mr image reconstruction," *Journal of Magnetic Resonance*, vol. 176, pp. 187–198, 2005.

[69] Xu, D., King, K., and Liang, Z., "Improving k-t sense by adaptive regularization," *Magnetic Resonance in Medicine*, vol. 57, pp. 918–930, May 2007.

[70] Ying, L. and Sheng, J., "Joint image reconstruction and sensitivity estimation in SENSE (JSENSE)," *Magnetic Resonance in Medicine*, vol. 57, pp. 1196–1202, June 2007.

VITA

Lei H. Hamilton was born in Hefei, Anhui province, China and received the Bachelor of Engineering (with high distinction) degree in Electrical Engineering from Anhui University, Anhui, China in 2002. She received her Masters of Engineering in Electrical Engineering at University of Science and Technology of China in 2002. She came to the United States in 2005 and spent one year and half in Auburn University, being a PhD candidate in Electrical and Computer Engineering, under the guidance of Dr. Thomas Denney. In 2007, she transfered to Gerogia Institute of Technology and worked under the direction of Dr. Marijn Brummer of Emory University for her doctoral research in bioenginnering major in Electrical and Computer Engineering Department. She has published a journal paper, five first author conference papers and abstracts.